2020

Defect Modeling and Vibration-Based Bending Fatigue of Additively Manufactured Inconel 718

Wesley Earl Eldt
Wright State University

Defect Modeling and Vibration-Based Bending Fatigue of Additively Manufactured Inconel 718

A thesis submitted in partial fulfillment of the requirements for the degree of
Master of Science in Mechanical Engineering

By

WESLEY EARL EIDT
B.S.M.E., Wright State University, 2019

2020
Wright State University

WRIGHT STATE UNIVERSITY
GRADUATE SCHOOL

April 29, 2020

I HEREBY RECOMMEND THAT THE THESIS PREPARED UNDER MY SUPERVISION BY Wesley Earl Eidt ENTITLED Defect Modeling and Vibration-Based Bending Fatigue of Additively Manufactured Inconel 718 BE ACCEPTED IN PARTIAL FULLFILLMENT OF THE REQUIRMENT FOR DEGREE OF Master of Science of Mechanical Engineering.

_____

Joy Gockel, Ph.D.
Thesis Director

_____

Raghavan Srinivasan, Ph.D., P.E.
Interim Chair, Department of Mechanical and Materials Engineering

Committee on final examination:

_____

Joy Gockel, Ph.D.

_____

Onome Scott-Emuakpor, Ph.D.

_____

Nathan Klingbeil, Ph.D.

_____

Barry Milligan, Ph.D.
Interim Dean of the Graduate School

ABSTRACT

Eidt, Wesley Earl. M.S.M.E. Department of Mechanical and Materials Engineering. Wright State University, 2020. Defect Modeling and Vibration-Based Bending Fatigue of Additively Manufactured Inconel 718.

Additive manufacturing (AM) is convenient for building components with complex features. However, the long-term integrity of these components is uncertain, since AM parts have defects such as pores and rough surfaces. In this work, an analytical model was developed to determine the impact of defects, and a novel bending fatigue test was used to determine the fatigue life of channeled specimens. The analytical model, based off the theory of critical distances, investigates coupled pores and predicts their potential for fatigue failure. This resulted in a maximum allowable pore size and spacing recommendation for coupled defects. Additionally, specimens with through channels built using laser powder bed fusion were tested in high-cycle vibration-based bending fatigue. The resultant S-N curve and fractography studies revealed similar performance between the channeled specimens and the solid specimens. This research serves to increase understanding of additive defects and their influence on the fatigue life of AM components.

TABLE OF CONTENTS

LIST OF FIGURES

LIST OF TABLES

Chapter 1: Overview

1.1 Introduction

Additive manufacturing (AM) provides numerous advantages over traditional machining processes. Fine resolution, intricate internal geometries, and rapid production of small quantities of parts are all benefits that AM technology allows, but the process is not without drawbacks. Defects, both inside and on the external surfaces of produced components, are inherent to the additive process. While these flaws can sometimes be removed during post-processing, this adds cost and is not always feasible. Therefore, the fatigue behavior of as-built additive parts is of interest to any industry looking to take advantage of the benefits of AM processes.

Defects most common in additive parts can be generalized into two categories: porosity and surface roughness. Pores are spaces within a component void of material, and surface roughness is imperfect finish on the outside of an AM build. Both of these can act as stress concentrators and initiation sites for crack propagation. This work includes two experiments, one focused on each primary defect type. The effects of porosity are explored through the development of a defect modeling method. This model is based off the theory of critical distances, an established but underutilized method for analyzing defects in parts. Initially developed for machined components with macroscale features, the capabilities of the theory are extended in this work to include microscale defects in the form of coupled

additive pores. Meanwhile, the effects of surface roughness are studied by conducting a series of vibration-based bending fatigue tests. Specimens with unpolished through-channels are fatigued and compared to otherwise identical solid specimens. In this manner, the effects of the rough channel surfaces are observed. These experiments provide meaningful findings that can both impact immediate manufacturing decision-making and guide future research in the field of additive manufacturing.

1.2 Motivation

The advantages of the additive manufacturing process make AM technology enticing to many industries, particularly the defense industry. This is evidenced by the release of the Department of Defense's *Additive Manufacturing Roadmap*, which outlines the organization's goals for advancing AM technology [1]. In particular, additive manufacturing offers the ability to rapidly prototype and produce unique components without the need for specialized and expensive assembly line equipment. This can save time and money both when developing new technology and when trying to replace or repair parts that are no longer in production. When employing additive technology, the integrity of the components should be thoroughly understood, particularly in applications of critical importance. Unfortunately, AM parts are notoriously unpredictable, especially in fatigue, due in large part to the quantity of defects that they often contain. While much work has been done to minimize the presence of defects in additive components [2] [3] [4] [5], the effects of the inevitable remaining defects are not yet fully understood. Therefore, the results of this work should be of interest to any industry in which the reliability of their components is of paramount importance.

1.3 Contributions

The contributions of this work can be summarized in the following four items:

1. The translation of the theory of critical distances into a form applicable to additive manufacturing porosity defects.
2. The development of guidelines for maximum pore size and minimum proximity to avoid fatigue failure.
3. The fatigue testing of novel geometry additively manufactured specimens with as-built through channels.
4. A direct comparison of solid and channeled specimens in vibration-based bending fatigue.

These contributions expand the current understanding of the effects of both internal and external defects inherent to additively manufactured parts, allowing for increased confidence in the fatigue performance of AM components.

Chapter 2: Background and Literature Review

2.1 Additive Manufacturing

2.1.1 What is Additive Manufacturing?

Additive manufacturing (AM) is a blanket term for manufacturing processes where the compositional material is gradually deposited until the desired geometry is complete. Frequently, this is done in a layer-by-layer fashion from the ground up. Additive processes stand in contrast to subtractive processes, where a block of material is cut until that which remains is the desired component, and formative manufacturing, in which liquid material is set in a mold until hardened. AM allows for increased part complexity, particularly when it comes to internal features; since builds happen a layer at a time, internal structures are built at the same time as external structures [6]. There is significant global interest in additively manufactured goods. The Wohlers estimate from 2014 gave the industry's annual revenue to be over four billion dollars [7], and this number is only expected to rise [8].

The additive manufacturing process begins with creating a computer-aided design, commonly referred to as a CAD model. In order to print layer-by-layer, the model must next be discretized. A stereolithography (STL) file is a common way to do this. STL files divide the component's geometry into a web of triangles, defined by three sets of vertex coordinates and a normal direction [9]. Since vertices must be shared between adjacent

triangles, the resulting organization has distinct layers that can be identified by an additive printer. Once the file is in the appropriate format, the build parameters can be selected. In laser powder bed fusion (LPBF), a common subset of AM, a typical parameter set might include laser power and speed, layer thickness, hatch spacing, scan pattern, and use of skywriting. Scan stripe width and overlap can also be specified [10]. Available parameters vary by specific additive process and machine used. Once all layers have been constructed, the specimen can be cut from the platform on which it was built, and the build process is complete.

2.1.2 Types of Additive Manufacturing

In 2012, the ASTM (American Society for Testing and Materials) identified seven distinct families of additive manufacturing technologies [11] [12]. These processes all share the common steps of AM outlined previously, but they vary in their specific means of achieving the final assembled component.

2.1.2.1 Vat Photopolymerization

Vat photopolymerization involves spreading a layer of liquid resin onto the build platform and then selectively hardening the resin using light, typically ultraviolet irradiation. The resin is distributed via a recoater, and the build platform moves downward after each layer that is built [13]. Advantages of this method include the potential for large build platforms, as well as smooth surface finish, with upward facing surfaces potentially having Ra roughness values of less than one micrometer [14].

2.1.2.2 Binder Jetting

The binder jetting build process begins by spreading a layer of loose powder across a build plate. The nozzle then prints a layer of the binding serum in the desired layer shape. The present layer is set by heat, and then a new layer of powder is spread and the process is repeated [15]. Once the final layer has been cured, loose powder is removed from the completed part. Applying an infiltrant to the completed build can help improve component strength [14].

2.1.2.3 Material Jetting

Material jetting is similar to the vat photopolymerization process. The key difference is that instead of spreading a layer of material using a recoater, the photopolymer build material is applied using an overhead nozzle before it is solidified by the UV light source [16]. Advantages of the material jetting process include cheaper printers [14] and the ability to use more than one material in the same build [12].

2.1.2.4 Sheet Lamination

Sheet lamination is a process that involves adhering solid layers of material together into the final desired geometry. Layers can either be pre-cut to the specified shape [14], or excess material can be removed once the adhesion process is completed [12]. The sheet lamination process can be done relatively quickly compared to other additive manufacturing methods and allows for simple changes in material from one layer to the next [12].

2.1.2.5 Material Extrusion

Material extrusion is one of the most publicly well-recognized forms of additive manufacturing, and it involves squeezing heated, softened material through a nozzle. The material is laid in thin paths until a single cross-section is complete [17]. Material solidification typically occurs naturally, in time with the extrusion process. This form of AM is popular because entry-level machines are affordable for individuals [14], and because homes and offices make suitable build environments [12].

2.1.2.6 Directed Energy Deposition

In directed energy deposition additive manufacturing, a melt pool is created on the previous layer using a laser energy source. A thin wire of material is fed into this melt pool, solidifying cohesively on top of the preceding layer [18]. This method is particularly useful for repairing existing parts, as its functionality is similar to that of welding [12]. Directed energy deposition also allows for less porosity and more control over microstructure; however, this comes at the cost of surface quality, feature resolution, and build time [14].

2.1.2.7 Powder Bed Fusion

Laser powder bed fusion is the additive process used to create the specimens tested in this experiment. In laser powder bed fusion (LPBF), material is swept from a powder bank onto the build plate using a recoater. Then, a high-energy laser melts the loose powder in the profile of a layer of the part being built. Once a single layer has been traced, the build plate shifts downward by a distance equal to the layer thickness, a new layer of powder is spread, and the next layer is melted onto the slowly growing component. Once the final layer is complete, the part is removed from the surrounding loose powder.

The LPBF process takes place in an inert gas environment. Often, this gas is either nitrogen or argon, the latter of which was used for the Inconel 718 build in this study. Maintaining a proper inert environment helps prevent reactions within the chamber during the build. Gas flow within the chamber has also been demonstrated to affect finished part qualities like overall part density [19].

Powder bed fusion carries a number of advantages over traditional manufacturing processes. Intricate internal geometries are more accessible with LPBF than even with other AM methods [14]. Additionally, a significant amount of different materials can be processed in this fashion, ranging from metals and plastics to ceramics and sand [12]. The laser powder bed fusion process is certainly not without its faults, however. Surface quality and feature accuracy are heavily parameter-dependent and can be difficult to optimize [14]. Furthermore, different machine parameters are applied when building over loose powder versus when building over solid part. This is further complicated by the fact that LPBF builds often require some amount of support structure, including a raft or other excess material on the bottom surface to help protect against warping [14].

2.1.3 Inconel 718

Inconel 718 (alloy 718) is classified as a high-strength thermal-resistant superalloy [20]. Because of this strength, heat resistance, and corrosion resistance [21], Inconel is frequently utilized in aerospace applications. The chemical composition of Inconel 718 is approximately 50% nickel and 20% chromium by weight, with small portions of iron, niobium, molybdenum, cobalt, and titanium, and trace portions of aluminum, carbon, manganese, silicon, phosphorus, sulfur, boron, and copper [22].

For the solid version of alloy 718, a room-temperature elastic modulus of approximately 28,000 ksi (193 GPa) and a Poisson's ratio of 0.280 have been established by the literature [22]. Material tests have also shown plates of Inconel 718 to have a yield strength of 105 ksi (724 MPa) and an ultimate tensile strength of 150 ksi (1.03 GPa) [23]. Work has been done to show that hot isostatic pressing the AM Inconel can sacrifice yield strength for an increased level of ductility. The same study found that static material properties of additive alloy 718 produced via laser powder bed fusion are comparable to those of its traditionally forged counterpart; however, porosity and microstructure still differ vastly and can create significant issues for the material's viability, particularly in fatigue [24]. Fatigue studies have had difficulty determining a fatigue limit for machined Inconel at high [25] or low [26] temperatures at 10 million cycles, and additive 718 is less likely still to display infinite life properties due to the additional defects present.

2.2 Common AM Defects

2.2.1 Surface Roughness

Perhaps the most apparent kind of defect resulting from an additive build is surface roughness. The quality of an additive surface depends heavily on the machine build parameters. Specifically, the contour parameters control the laser while tracing the outside edge of each layer of the build [27]. The relationship between these contour parameters and the surface finish has been thoroughly reviewed, with consensus being that the two are strongly tied [28] [29] [30]. Further, a parameter known as the downskin parameter can be defined. This parameter is applied when the AM machine recognizes loose powder within a set number of layers below the scan path. The purpose of this separate parameter set is to

lessen the effect of build angle on the resulting downward-facing surfaces' roughness metrics. As-built downward-facing surfaces tend to have a rougher finish than either horizontal or vertical surfaces [4] [31] [32].

The dogbone specimens used in this experiment were manufactured such that one half of the internal through channel can be categorized as a downward-facing surface. As stated above, these regions are expected to have increased surface roughness. This is particularly relevant since surface quality has previously been linked to fatigue life [33] and fatigue strength [34] in additively manufactured materials. This is due to the high number of stress concentrators, in the form of surface valleys, both increasing local stresses and acting as potential crack initiation points. In order to better discuss and quantify the effects of surface quality on component life, a number of standard surface roughness metrics have been established.

2.2.1.1 Surface Roughness Metrics

The International Organization for Standardization (ISO) has defined seven metrics for characterizing the severity of surface roughness [35] [36]:

Sa – The average roughness is calculated as the mean vertical distance away from the plane of average height.

Sv – The maximum valley is the distance from the plane of average height to the lowest point on the surface.

Sp – The maximum peak is the distance from the plane of average height to the highest point on the surface.

Sz – The maximum height range is the distance between the maximum valley depth and the maximum peak height.

Sq – The root mean square roughness is the square root of the sum of squares of all points' distances to the plane of average height.

Ssk – The skewness is the left/right asymmetry of the probability density curve of all points' distances to the plane of average height.

Sku – The kurtosis is a measure of the steepness of the probability density curve of all points' distances to the plane of average height.

Each of these metrics is calculated using the height data from an area of surface. However, each also has an equivalent R metric that can be found using only a line of height values [37]. Calculating surface metrics based off only a line of values may yield results less representative of the entire surface, but it provides two advantages. Firstly, computational time is decreased drastically. Secondly, some regions that would be essentially unmeasurable using surface methods may become accessible when only a linear measurement is necessary.

To measure the roughness of a channel, the specimen would need to be cut so as to avoid any distinctive end effects. Next, a light microscope could be used to measure the location data of all the points making up the surface of the hole. Some light microscopes have the ability to shape correct, which would be helpful in accounting for the circular (or in the case of particularly high roughness, elliptical [31]) profile of average height. Discretion must be used when determining whether to correct based off the circular or

elliptical estimation of an aberrant channel profile. While measuring from the nominal circular path might be a better gauge for determining "quality" of the build, taking the roughness from the actual resultant elliptical profile may provide a more accurate analysis for the potential detriment to fatigue life. In the vibration-based bending experiment presented in this work, specimen geometry and the destructive nature of the test did not allow for thorough measurements of the as-built roughness inside the channels.

2.2.2 Porosity

Together with surface roughness, porosity is one of the most prevalent and most studied types of defects observed in additively manufactured components. A pore is a small, (usually) unintended void in the solid material composition of a completed part. (Note: Sometimes, particularly in biomedical applications, small amounts of porosity are beneficial for reasons unrelated to strength or fatigue performance [38] [39]. However, in industrial applications, porosity is almost invariably viewed negatively.) "Density" is used as a term to describe the total solid material within the component, or one minus the total porosity.

Studies have been performed with the intention of increasing the total density of additive components. These previous tests vary from optimizing parameter sets including scan strategy, laser speed [2], hatch spacing [40], and others, to post-processing techniques like chemical etching, hot isostatic pressing, and stress relieving [41]. Interest in decreasing porosity is high because, like surface defects, internal pores create stress concentration points that detract from the integrity of the part. Also similar to roughness, post-build remedies are not always viable for correcting porosity issues due to a component's frailty,

precision, or reactivity. Therefore, strong demand exists for minimizing porosity during the build process and understanding the effects of pores that remain even after treatment [42].

2.2.2.1 Types of Porosity

Pores are typically classified into three categories depending on their size, shape, and means of formation. Lack of fusion pores are created when a particular spot does not receive enough energy from the laser pass, creating too small of a melt pool [3]. This can occur due to a laser speed that is too high, a laser power that is too low, hatch spacing that is too wide, or other similar factors. Lack of fusion pores are frequently irregular, narrow shapes.

In contrast, keyholing can occur when a location receives too much energy. At a not yet fully realized threshold, some of the melted metal powder transforms into the vapor phase. This vapor works to amplify the laser absorption into the solid metal below, creating a deep gaseous cavity that can collapse into a porous void [43]. Keyhole pores are named for the shape of the deep vertical hollow that is formed.

Gas porosities are small, spherical pores that are created from entrapped gas originating from the build environment. Gas porosities are often smaller than other kinds of voids and sometimes occur in clusters. Individual gas porosities have near-negligible effects on part performance, and in those instances when some porosity is desirable, gas porosities are the target features [38].

2.2.3 Microstructure Considerations

The final microstructural composition of an additively manufactured component is complex and heavily dependent on the thermal history of the material during the build [44]. This thermal history is the aggregation of numerous build parameters and other factors, a list which can include laser power and speed [45], part geometry [46], chamber air flow rate and direction, build plate location [47], layer height [48], hatch spacing, and scan strategy [49]. All of these contributors have direct influence over two secondary metrics for describing the thermal history: melt pool size [50] and cooling rate [51].

The bottom-to-top nature of an additive build dictates that a part will likely be anisotropic on the microstructural level. Grains can become elongated in the vertical direction, potentially decreasing material strength along this axis [52]. In order to counteract these effects, the specimens in this experiment were built in the direction parallel to the bending deflection rather than the axis of bending stress application. This may also reduce the risk of possible layer separation, which can become a concern under non-optimal loading orientations [53].

2.3 Fatigue in Additive Manufacturing

Fatigue is the process in which repeated loadings of magnitudes smaller than a material's yield strength can result in eventual failure. The fatigue process can be divided into three parts. Stage 1 is the gradual initiation of a crack, Stage 2 the propagation of that crack across the cross-section of the part, and Stage 3 the sudden failure once the weakened part can no longer withstand the applied loading [54]. These loadings can be random or

cyclic. The load ratio is the ratio of a cyclic loading pattern's minimum applied stress to its maximum applied stress.

Fatigue is often divided into low-cycle and high-cycle categories. Generally, low-cycle fatigue encompasses failures that occur at less than about 10^3-10^4 cycles, while high-cycle fatigue includes any number of loadings greater than that. Some metals, given enough loadings, will fail at virtually any applied stress level. Others will last into the infinite life regime (> ~10^7 cycles) unless the applied loading is greater than a certain magnitude, known as the endurance or fatigue limit.

AM components are particularly vulnerable to fatigue due to the high number of defects present within 3D-printed material. Geometric inhomogeneities such as surface notches and internal pores increase local stresses and make convenient locations for crack initiation, potentially greatly reducing the total fatigue life of the part.

2.4 Fatigue Testing Methods

The repeated stresses applied during a fatigue test can be produced by various means. Likely the most utilized method is the axial tension fatigue test. In this method, each end of a test coupon is gripped and pulled repeatedly with a specified force or displacement [31]. Axial tests are convenient because axial load frames are relatively common. Specimens of any cross section can be tested, and the stresses obtained will be equal across the entire cross section of the part. Drawbacks to this process include relatively slow load frequency (on the order of 20 Hz [31]) and the over-simplified loading that is not representative of what most components will realistically face in application [55].

A more complex loading can be achieved in the form of a rotating-bending fatigue test. In this arrangement, a radially symmetric test coupon is clamped in place while a calibrated weight driven by a motor spins around the specimen, inducing bending stress. This test is relatively low frequency (on the order of 30 Hz [56]) due to the wide range of motion of the parts. This method has also been criticized due to its "less severe" loading capabilities compared to axial fatigue tests [57].

Vibration bending fatigue is a novel testing method that consists of a specimen mounted in a carrier plate fastened to a shake table. As the shaker vibrates, bending stresses are achieved in the specimen as a resonance frequency is activated [55]. This vibration fatigue method shares advantages with both axial and rotating-bending tests. Like rotating-bending fatigue tests, a higher order mode shape is obtained via the application of bending stresses. Additionally, with a sufficiently capable shaker, stresses can be obtained on par with those used in axial fatigue tests [58]. However, unlike both axial and rotation-bending fatigue tests, vibration bending can achieve load frequencies upwards of 2,000 Hz, allowing for much faster fatigue testing [55].

2.5 Defect Modeling for Additive Manufacturing Fatigue

The presence of defects within a material can cause decreased performance in both static and fatigue loading. Defect modeling is useful for predicting how a particular defect will affect a given part under specific loading conditions. However, creating models means making assumptions that will affect the accuracy of the prediction. Different fatigue analysis procedures exist with their individual advantages and disadvantages, and each of them becomes increasingly complex to use when applied to additively manufactured

components. This is due to the large quantity of defects present and the inconsistency in these defects' geometries and arrangements.

2.5.1 Linear Elastic Fracture Mechanics

One common method for explaining fatigue behavior is using the linear elastic fracture mechanics (LEFM) approach. This method starts by assuming a crack is immediately present in the part and examines the continuously changing stresses surrounding the crack's tip as it propagates throughout the component. LEFM relies on the value of the stress intensity factor, which is a function of the length of the crack of interest. As the crack grows, so does the stress intensity factor, increasing the effective stress on the part. As one might expect, the predicted stress reaches its maximum value immediately at the crack tip; in fact, the stress asymptotically approaches infinity in this region [54]. These stress intensity factors are treated as multipliers of the applied load, indicating how much more stress the region around a crack tip faces compared to the solid body of the part, allowing for the life prediction to be adjusted accordingly.

2.5.2 Strain Energy Methods

Strain energy methods are another possibility for analyzing the fatigue life of a metal component. Energy is stored in the physical bonds and the geometry of the microstructure of a material. When deformation occurs, often in the form of a crack lengthening or widening due to applied loading, some of this stored energy is released, and this energy can be quantified [54]. Since the load-bearing capability of a material is related to the amount of energy stored in its microstructure, the experienced energy loss can be used as a metric for how much more strain the component will be able to withstand before

ultimate failure. When the total strain energy density, which can be visualized as the area under the stress-strain curve, reaches its maximum value for the material, failure is predicted to occur [59]. This method again relies on continuously updated measurements of the state of the part along the cracking region, as the total released strain energy will increase minutely with every applied cycle of loading.

2.5.3 Methods Unique to Additive Manufacturing

Several past research efforts have worked to correlate defect measurements to fatigue life in additively manufactured components. These have included relating pore density and size to fatigue performance [60] [61], relating average roughness and maximum surface notch depth to fatigue performance [27] [33], and calculating maximum allowable stress intensity factors [62]. These studies have helped increase the community's understanding of the relationship between defects and fatigue performance, but the results can usually be summarized in this way: Having more defects is worse than having fewer defects, and large defects are worse than small defects. Thus far, the question of how big a defect must be before it becomes a concern has remained unexplored because traditional fatigue prediction models do not allow for this kind of prediction. However, another burgeoning method of fatigue analysis does have this capability.

2.5.4 The Theory of Critical Distances

Originally conceptualized by Tanaka [63] and later expanded and publicized by Taylor [64], the theory of critical distances (TCD) is a family of methods for analyzing a component for viability under a given loading. Instead of investigating a defect for the maximum stress concentration that it will cause, the TCD postulates that a defect can be

adequately examined by determining the stress at a location some distance away from the tip of the flaw. The space of interest is either a single point or the integrated sum of a line, area, or volume, depending on the specific method being applied. The distance away from the defect is the calculated "critical distance" and is the unique facet of the TCD [64]. Some possible areas of analysis are depicted below in Figure 1.

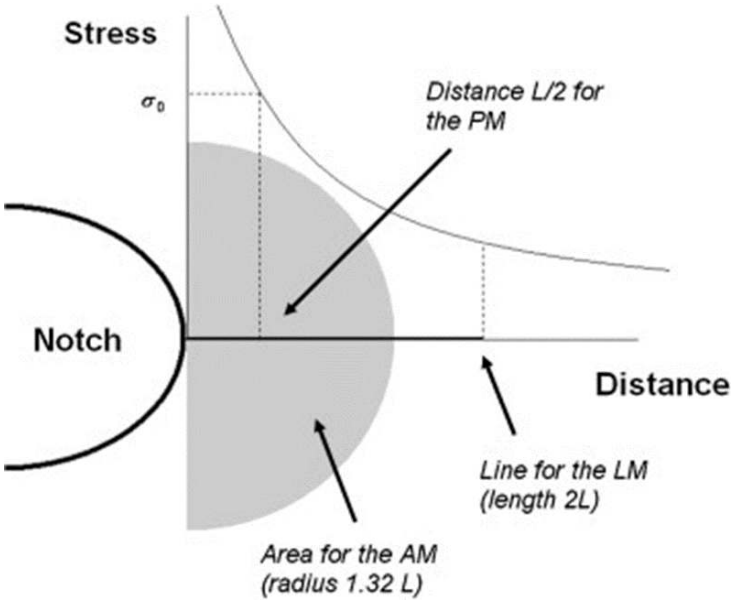

Figure 1: Locations of interest for the area method (AM), line method (LM), and point method (PM) of the TCD as a ratio of the critical distance L *[65]*

If the stress experienced in the designated region surpasses a calculated stress threshold, then the component is predicted to experience fatigue failure. Determining the necessary stresses are left up to the user, so while closed-form solutions may be helpful for the point and line methods, the more complex methods would likely require use of finite element analysis. However, herein lies one of the major advantages of using the theory of critical distances: It is not necessary to know the stress directly at the tip of the defect. This eliminates the need for converging a stress solution at the tip of a sharp notch, which is

theoretically infinite in linear elastic fracture mechanics. Another benefit is that a defect can be analyzed once, before loading, and a prediction can be made for the fatigue performance of the part. This stands in contrast to previous methods which required constant knowledge of the crack's progression in order to recalculate stress intensity factors and remaining strain energy.

The theory of critical distances was developed for and has been most frequently applied to intentional, notch-like features on the surfaces of components. These include fatigue validation of the theory [66], as well as extension of its use to fatigue [67] and fracture [68] of porous polymethylmethacrylate (PMMA). The TCD has also been applied to surface roughness of machined components [69]. A recent publication has attempted to apply the theory of critical distances to individual three-dimensional spheroidal pores [70], but additive pores often reside in close proximity to one another. One study has been performed to analyze coupled pores [38], but this was not concerning an additive material and did not attempt to discern threshold defect sizes or proximities. The TCD has great potential in its ability to superimpose stress solutions, and the field of additive manufacturing can benefit from this.

Chapter 3: Development of the Analytical Model

3.1 Introduction

The theory of critical distances has been thoroughly explored for large-scale designed features that act as stress concentrators; however, the microscale and geometries relevant to additive defects are much less established under the theory. This chapter walks through the equations used to develop stress profile maps and how these equations were applied to coupled spherical pores.

3.2 Applying the Theory of Critical Distances

The first step when applying the theory of critical distances was to select one of the four methods. Due to the novelty of the analysis that was to be performed, the point method was chosen as it is the most straightforward method. The point method uses the stress at a location half the critical distance away from the defect as its critical point. The failure criterion can be expressed in equation form:

$$\Delta\sigma\left(\frac{L}{2}\right) = \Delta\sigma_0$$

In this equation, L is the critical distance, $\Delta\sigma$ is the stress range at a given location, and $\Delta\sigma_0$ is the threshold stress range above which premature fatigue failure of the part due to the defect would be expected. This maximum stress range was calculated using the

literature fatigue limit for the preferred material (σ_0) as well as the desired stress ratio (R) of the cyclic loading, and can be calculated using the following equation:

$$\Delta\sigma_0 = \sigma_0 * (1 - R)$$

Once the threshold was determined, the next step was to determine the critical distance length for a given defect. This distance (L) was defined by the following equation:

$$L = \frac{1}{\pi} * (\frac{\Delta K_{th}}{\Delta\sigma_0})^2$$

ΔK_{th} is the fatigue stress intensity factor applied at the fatigue limit and is calculated by:

$$\Delta K_{th} = 1 + q * (K_t - 1)$$

In this equation, q is the notch sensitivity and K_t is the stress concentration factor caused by the defect under analysis. For a notch, the stress concentration factor is provided as:

$$K_t = 0.855 + 2.21 * \sqrt{a/\rho}$$

Here, a is the notch depth and ρ is the notch tip radius. With the exception of the author-generated threshold stress range calculation, these equations were obtained from the primary book on the TCD, Taylor's *The Theory of Critical Distances: A New Perspective in Fracture Mechanics* [64].

The biggest hurdle to overcome was translating the equations that were created for designed notch features into a form applicable to spherical additive pores. In this analysis, pores were modeled as notches with length and radius equal to the radius of the pore. This was done to compare the pore to a hemispherical notch. Consequently, the $\sqrt{a/\rho}$ term was

a constant value of 1 for all modeled pores. For the purpose of the model, notch sensitivity q, which can possibly vary from 0 to 1, was assigned a constant value of 0.5. The result of this was a constant ΔK_{th} value of approximately 2.03. With this, combined with the constant $\Delta\sigma_0$ as a result of the consistent material and load ratio, the critical distance L became constant 6.49 μm for all spherical pores regardless of radius. The failure criterion then simply became a function of only a single variable: the stress at a distance L away from the surface of a given pore.

3.3 Calculating Local Stress

The final step necessary to complete the analysis, then, was to determine the stress at the critical distance location. The loading was assumed to be uniform uniaxial tension on a part that was large compared to the defect inside. The stress at a point was determined using the following equation, obtained from the work of Vardar, et al [71], and developed based off the work of Goodier [72]:

$$\sigma_\theta = \frac{S}{2} * (1 + \cos(2\theta)) + \frac{S}{4(7-5\nu)} * \left(\frac{\rho}{d}\right)^3 * \{ (13 - 20\nu) - 3\left(\frac{\rho}{d}\right)^2 - \left[5(1-2\nu) - 21\left(\frac{\rho}{d}\right)^2\right] * \cos(2\theta)\}$$

In this equation, d is the distance away from the center of the pore, ρ is the pore radius, ν is the Poisson's ratio for the material (0.294), S is the applied stress, and θ is the angle from the horizontal axis in the direction of the vertical loading (0). To determine the stress at the critical distance point, a distance $d = \rho + L$ was applied, since d was measured from the center of the pore and L was from the pore's surface.

Stress profiles were obtained in this manner, plugging in all location values from the surface of the pore until to a point where σ_θ sufficiently approached S. To obtain the total stress profile for a pair of pores, the distance between them was first defined. Then, all distances from the surface of one pore to the surface of the other were plugged in and σ_θ values were obtained. The individual profiles were summed together, and a single S value was subtracted from the total so that the applied stress was not counted twice. The profiles were then plotted against the threshold stress, and the resulting graphs are presented in the following chapter.

Chapter 4: Defect Modeling Results

4.1 Introduction

Coupled pores of equal radius were modeled under a uniformly applied tensile load using the theory of critical distances as a standard for determining failure. The theory's point method postulates that the stress at a location a particular distance away from a defect can be used to predict whether or not the defect will have a negative effect on the fatigue life of the part in which it resides. This chapter presents the results of modeling coupled pores of various sizes and at a range of separation and attempts to unify the findings into standard guidelines for maximum allowable pore size and proximity.

4.2 Interpreting Results

The results of the coupled defect analysis model are presented first in the form of stress profile maps. These plots show the effective stress calculated at all points between the two defects of interest. An example curve is shown in Figure 2 below.

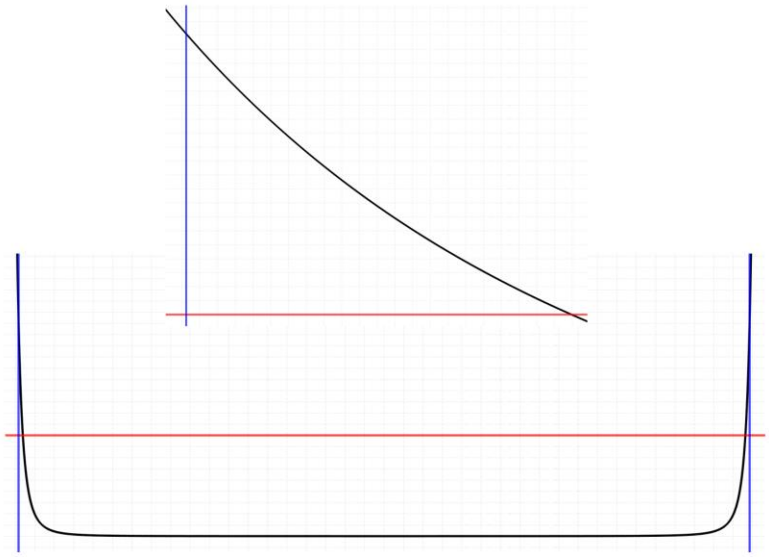

Figure 2: Sample stress profile

The sample plot features a zoomed in view of the left location of interest. On these plots, the black curve represents the effective stress experienced by the part, composed of the applied stress and the stress concentration contributions from both defects. The blue lines represent the locations of the critical distance from each defect, according to the point method. The red horizontal line is the threshold stress, which is compared to the stress profile at that the critical distance location to make a fatigue effect prediction for the given defect orientation. If the stress profile exceeds the threshold value at the critical distance location, then the defects are predicted to impact fatigue life according to the theory of critical distances fatigue criteria. If the stress profile is below the threshold stress at the location of the critical distance value, then the effect of the present defects on the fatigue life of the component is considered negligible. In the following stress profiles, the stress profiles and critical distances are symmetric due to individual defect couples being composed of pores of the same radius. Precise stress values at critical distance locations are marked with red stars for ease of interpretation.

Stress profiles were created by varying two parameters: the pores' radial length (r) and the pore separation – pore radius ratio (t/r). Figure 3 demonstrates these values with respect to the defect arrangement.

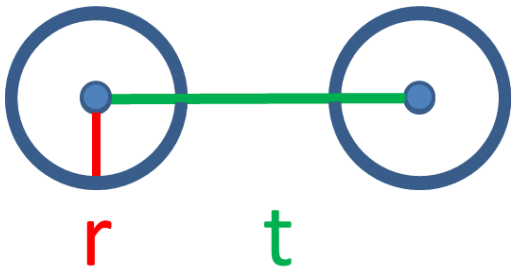

Figure 3: Varied parameters in the coupled defects analysis

Parameters held constant throughout all trials are displayed in Table 1.

Parameter	**Constant Value**
Applied Load	400 MPa
Load Ratio	0.1
Material Endurance Strength	500 MPa
Poisson's Ratio	0.294
Notch Sensitivity	0.5
Allowable Stress Threshold	450 MPa

Table 1: Experimental constants

4.3 Stress Profile Maps

For the purpose of trend analysis, many stress profile maps were developed, with situations representing a range of r values from 5-20 µm and t/r values ranging from 3-100. In this section, three plots are presented to demonstrate the overarching trends, and the rest are represented in the next section as data.

The first stress profile presented for discussion is the r = 20 µm, t/r = 10 plot. This is seen in Figure 4 below.

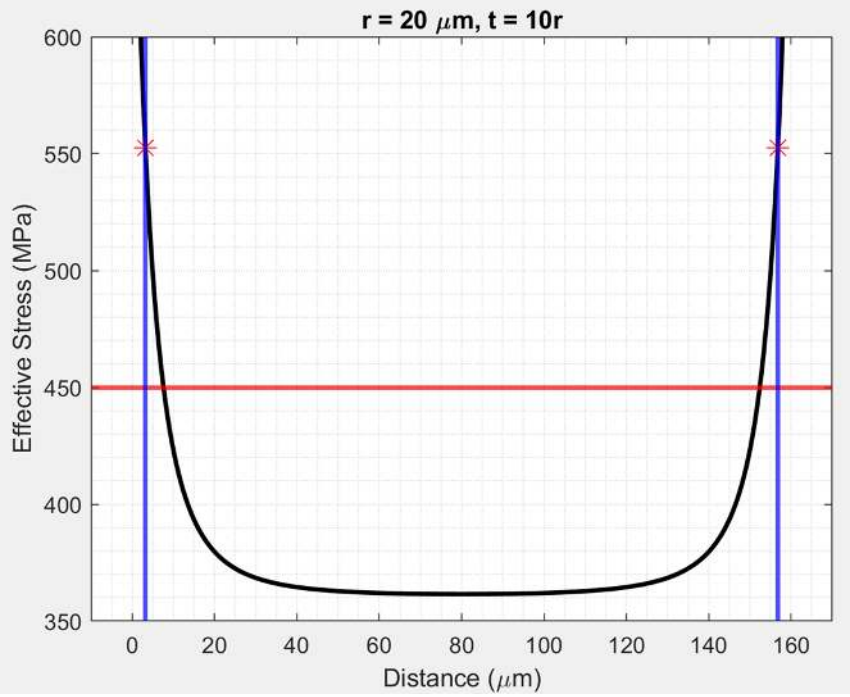

Figure 4: Stress profile, r = 20 µm, t/r = 10

In this graph, it is clear that the effective stress experienced at the critical distance locations is well above the allowable threshold. This implies that two pores of radius 20 µm and at a center-to-center distance of 200 µm will cause sufficient stress concentration effects to decrease the fatigue life of their component. The current model does not attempt to quantify this negative effect, but it can be inferred that greater oversteps of the tolerable stress will be more detrimental to fatigue performance.

The next figure maintains the same t/r value of 10 but decreases the pore radius value to 5 µm.

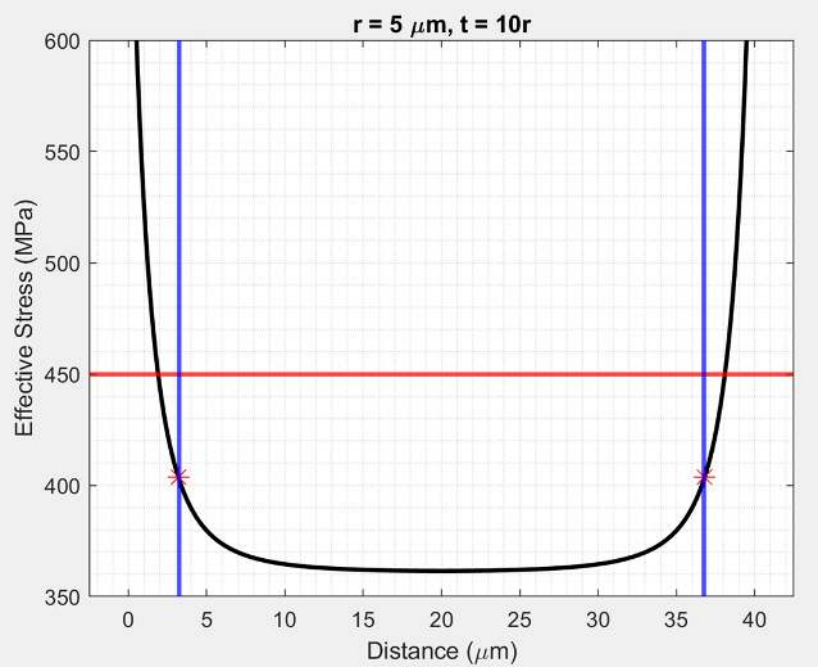

Figure 5: Stress profile, r = 5 μm, t/r = 10

Direct comparison between Figure 4 and Figure 5 reveals that the shape of the stress curve remains constant, since the t/r quantity remains unchanged. The stress at the critical distance, however, decreases with decreasing pore radius. This is because the critical distance is now a greater portion of the total t/r distance. The difference in this case is enough for the 5 μm radius pores to stay under the allowable stress threshold.

The final stress profile plot presented, Figure 6, maintains the 5 μm pore radius, but this time the t/r ratio is increased to 40.

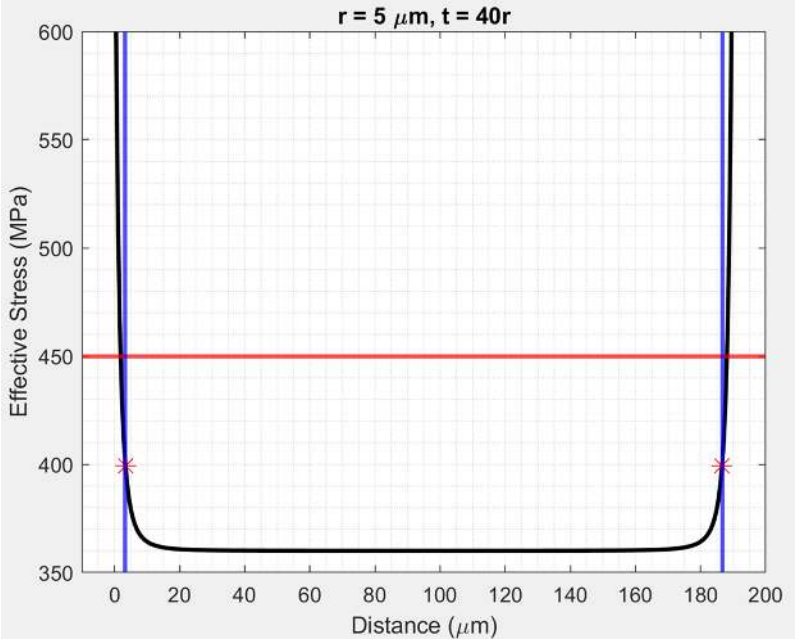

Figure 6: Stress profile, r = 5 μm, t/r = 40

In this stress map, much of the space between the pores is clearly defined by a constant stress value. This effective stress value of 360 MPa represents the range of stress experienced by the part under the cyclic loading with no additional stress contribution from the defects. This is due to the much larger distance between the pores relative to the size of the defects (increased t/r ratio). It can be noted that the stresses experienced at the critical distance locations in Figure 5 and Figure 6 are essentially equivalent at approximately 400 MPa, despite the large difference in t/r between the two. The cause of this phenomenon is discussed in the next section.

4.4 Determination of Critical Pore Characteristics

The radius and t/r parameters were varied in the Matlab script to determine critical pore characteristics. These values were obtained by selecting a pore radius and gradually adjusting the t/r ratio until the distance where the effective stress was equal to the threshold

stress at the critical distance location was determined. A brief summary of these results can be seen in Table 2.

r	t/r	t
5.0 µm	3.25	16.2 µm
6.0 µm	3.26	19.5 µm
7.0 µm	3.48	24.3 µm
8.0 µm	4.0	32.0 µm
8.50 µm	6.7	56.9 µm
8.55 µm	89	760 µm

Table 2: Critical t/r values for increasing pore sizes

It is observed that there is a rapid jump in necessary t/r distance for pores of diameter greater than 17 µm. This is further visualized in Figure 7, shown below.

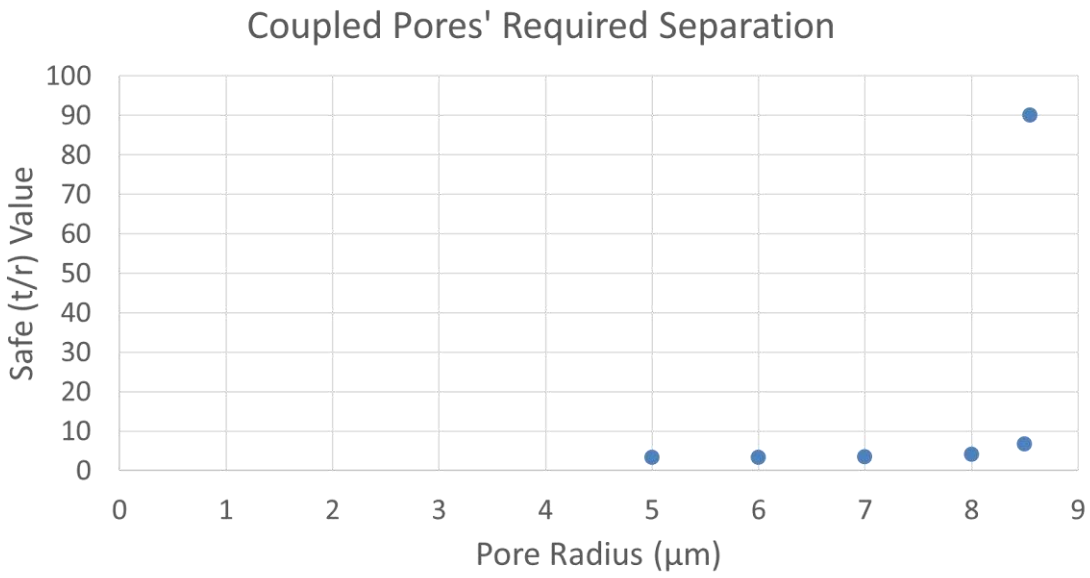

Figure 7: Required t/r separation of coupled pores of various sizes

This behavior demonstrates an asymptote in the data at approximately 8.55 µm pore radius. This represents the defect size that becomes a detriment to fatigue life with only a single pore present. At this defect size, the "required separation" distance approaches infinity and eventually no longer exists as the stress caused by a single pore surpasses the allowable stress threshold. This pore size of diameter 17 µm could serve as a theoretical maximum tolerable defect size for build parameter optimization goals, provided that all pores of this size maintain a center-to-center separation of at least 56.9 µm.

4.5 Conclusions

In this chapter, the theory of critical distances was used as a foundation for the development of stress profiles of coupled additive pores. It was found that the established model predicts premature fatigue failure when individual pores are larger than radius 8.5 µm, or when smaller coupled pores are closer than 56.9 µm center-to-center. The strictness of these guidelines indicates that efforts toward decreasing porosity in AM components are worthwhile, since typical additive parts will have numerous pores surpassing these limits. The degree of impact these defects cause on the fatigue life of their components is yet to be determined, but the TCD has the capability to attempt this kind of prediction as well in future studies [64].

Chapter 5: Vibration-Based Bending Procedure

5.1 Introduction

The experimental procedure for the vibration-based bending fatigue tests detailed in this work was recent and novel in its development. Therefore, this chapter presents a brief history and thorough walkthrough of the testing procedure.

5.2 History and Nature of the Vibration-Based Bending Fatigue Test

Traditionally, high-cycle fatigue tests have primarily been performed by applying a uniaxial, tensile stress. However, there are deficiencies to this testing method. First, axial loading is not representative of the stresses that would be experienced by turbomachinery components in vivo. Rather, failure in turbine blades is often caused by higher-mode bending stress induced by frequencies far higher than can be achieved by typical axial load frames [55]. This leads into another shortcoming of the axial test method: High-cycle tests can take many hours to complete. For example, a given uniaxial tension experiment may be run at 20 Hz [31]. At this frequency, a single 10^7-cycle fatigue test would take well over one hundred hours of continuous testing. This is a very long time to obtain a single point for an S-N curve, especially when continuous overnight testing is not always possible. Therefore, a more rapid, and more realistic, testing method was desired and developed by the Air Force Research Laboratory's Turbine Engine Fatigue Facility (TEFF) [55].

5.2.1 Previous Iterations of the Vibration-Based Bending Fatigue Test

The TEFF's concept of the vibration-based bending fatigue test was first developed using a single-use square plate. The square geometry was selected due to its favorable behavior when loaded in uniaxial bending [55]. The vibratory response of a fixed-free square plate produces a region of maximum stress at the free end, which nullifies the complications of stresses at the cantilevered end. The displacement and stress profiles of the square specimen are shown in Figure 8.

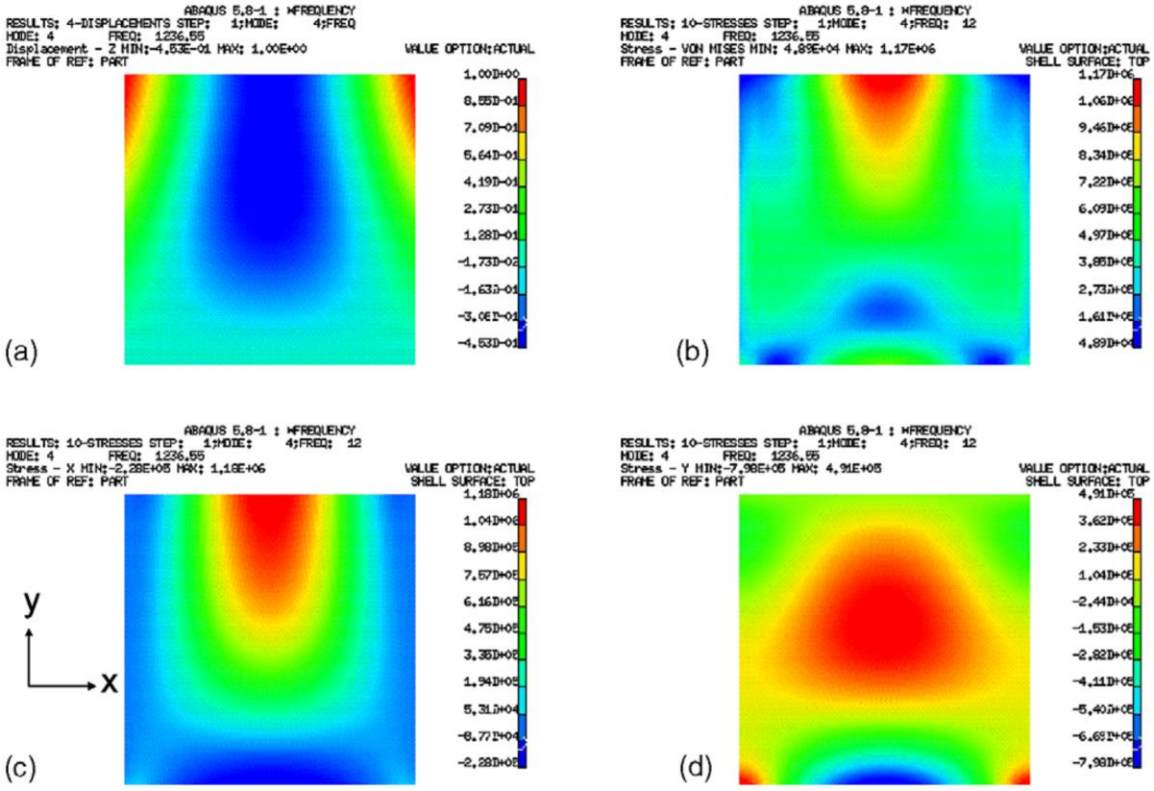

Figure 8: (a) Out-of-plane displacement, (b) von Mises stress, (c) x-direction stress, (d) y-direction stress for a square cantilever plate subject to chordwise bending [55]

Once the testing method had been developed, further improvement was desired. Specifically, the amount of material spent per test was much higher than traditional axial fatigue tests. The entire plate measured 114 x 165 x 3.1 mm, but failure was always

expected to occur at a much smaller region located at the center of the free end of the plate [55]. This prompted the creation and optimization of the hybrid insert plate. An iterative trial-and-error approach led to the design and testing of numerous rectangular inserts that each fit in a carrier plate similar to the original square test specimen [73]. Several versions of the plate-insert system are displayed in Figure 9.

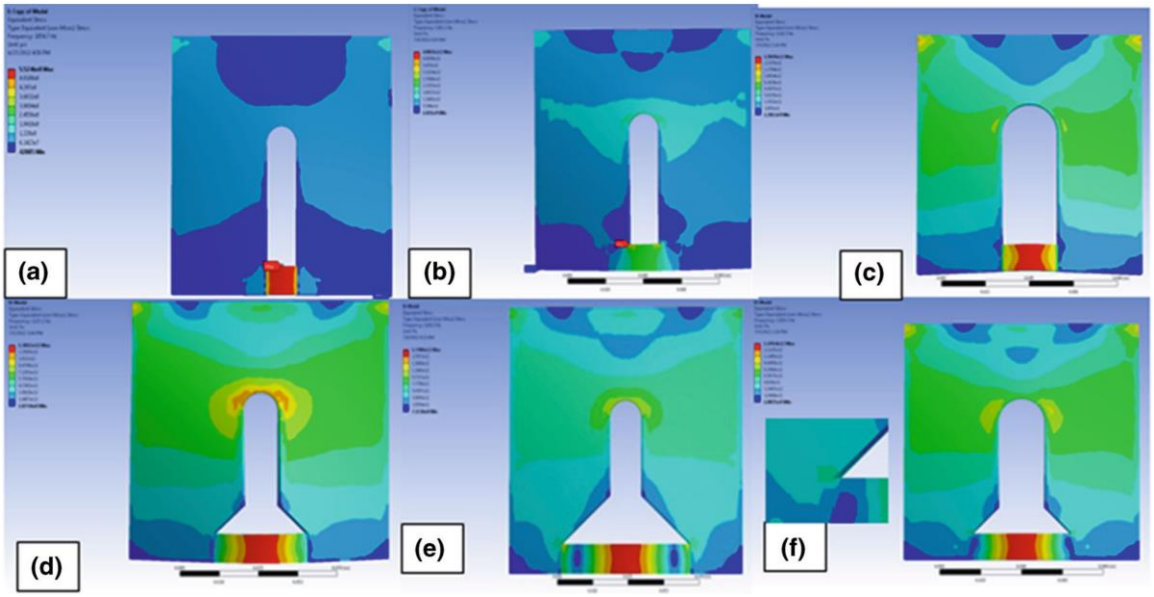

Figure 9: Iterations of the hybrid insert-plate [73]

At this point, the material waste for individual tests had been reduced by roughly 95% [73], but there were improvements left to be made. The carrier plate was still sustaining small amounts of damage that accumulated over the course of multiple tests. The specimen was also being damped more than desired by its interaction with the carrier plate [74]. This was rectified by further adjustment to both the plate and specimen geometry, which tested similarly to the original whole plate specimen with a 95% confidence interval [74]. Figure 10 below demonstrates the current iteration of the hybrid plate-insert and corresponding specimen used in the experiment at hand.

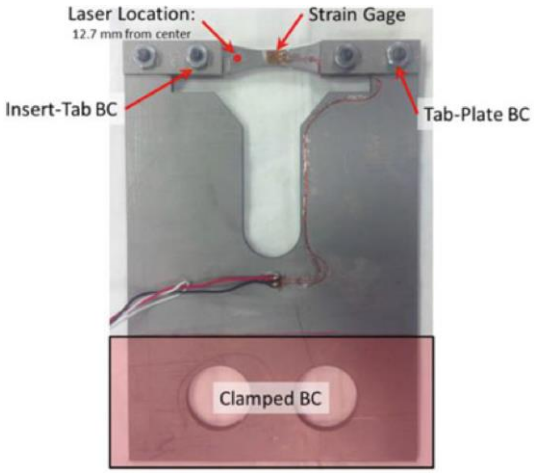

Figure 10: Optimized hybrid insert-plate utilized in this experiment [74]

5.2.2 Novelty of this Iteration of the Test

This experiment advances the relevancy of the vibration-based bending fatigue test by giving the specimens a relevant internal feature in the form of an as-built through channel. If additively manufactured materials are to become commonplace in industries such as aerospace with high integrity requirements, then the effects of additive defects must be thoroughly understood under realistic loading conditions. The goal of this study was to compare the fatigue performance of channeled test coupons to that of similar specimens built without the internal feature. A significant drop off in performance from solid to hollow specimens would bode poorly for the viability of AM materials in critical applications, since porosity and unpolished internal surfaces are essentially unavoidable when employing additive manufacturing technology. Bending fatigue of featured AM parts is yet unexplored, and a better understanding of this situation will either bring additive manufactured parts closer to utility in aerospace or bolster the validity of existing concerns.

5.3 Test Specimens

5.3.1 Specimen Geometry

The dogbone specimens built for this experiment were designed specifically for the testing process at hand, with the geometry displayed in Figure 11 below. Coupon outside dimensions were 3” long by 1/2” wide by 1/8” thick (76.2 x 12.7 x 3.18 mm). The gage section was the middle 1 1/2” (38.1 mm) of the specimen, rounded such that the center width was 1/4” (6.35 mm). Channeled specimens were built with a 0.060” (1.52 mm) diameter hole through the length of the part. This size was selected as a compromise between being a large enough feature to accurately build, but not so large as to detract from the durability of the specimen during handling. The two mounting holes were drilled through the broad sides of the grip section at a distance of 2 1/4” (57.2 mm) apart.

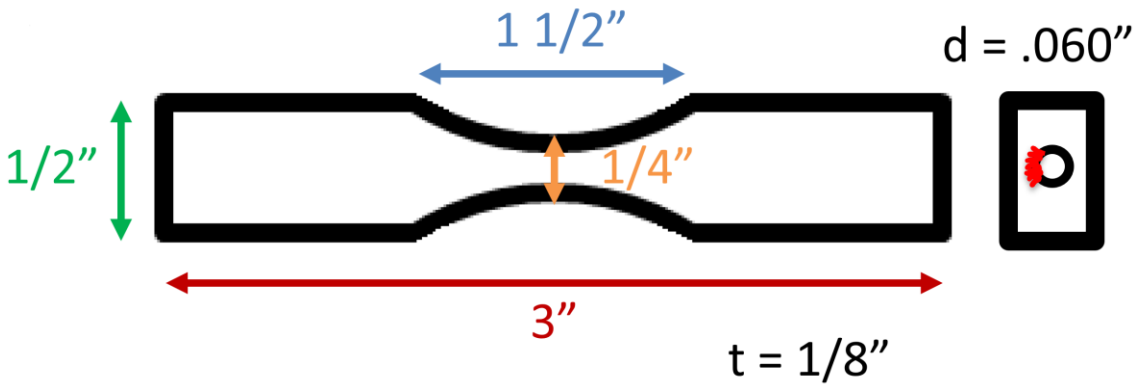

Figure 11: Specimen geometry

Specimens were granted a couple benefits from their geometrical design. Firstly, the curved section spanned the entire length of the gage section. Therefore, there were no extra corners along the gage section. This helped eliminate unnecessary stress concentration points. Further, there was a single plane of maximum bending stress, namely,

the cross-section at the very center of the length of the part. In this location, the cross-sectional area was minimized. Therefore, failure was logically most likely to originate in this plane, either at the corner of the specimen (where maximum bending stress on the surface met the sharp corner stress concentrator) or at the surface of the channel (where surface roughness incorporated many smaller, less-predictable stress concentrators). A simple finite element model was developed using SolidWorks to demonstrate the von Mises bending stress of the center cross section with theoretically no roughness on the channel surface. This analysis can be seen below in Figure 12.

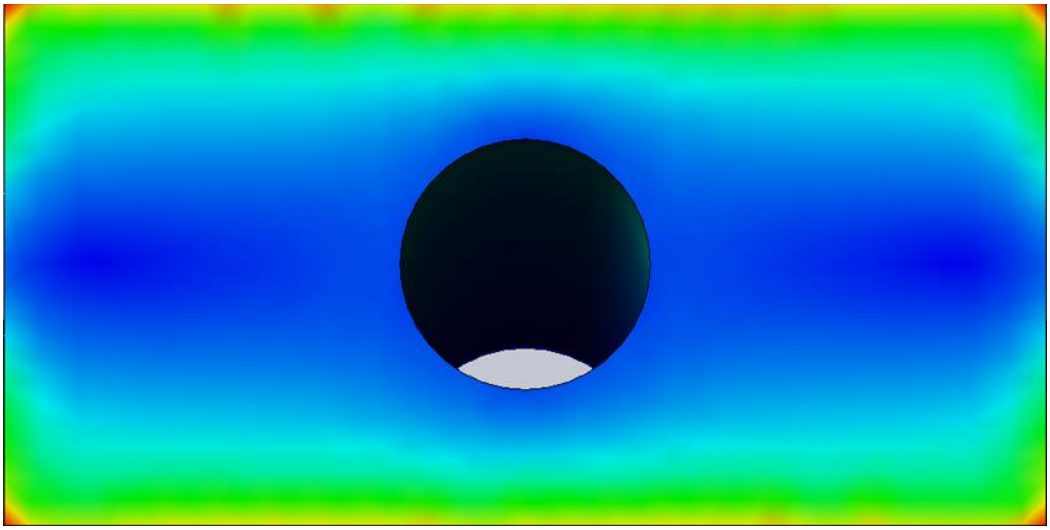

Figure 12: Bending specimen von Mises stress profile

The bending stress of a cross section is theoretically zero along the neutral axis and increases linearly moving closer to the top and bottom surfaces of the part. The symmetry of these specimens means the neutral axis is along the centroidal axis. Therefore, from the thickness of the specimens and the diameter of the hole, an approximate value of stress at the edge of the channel can be calculated to be 48% of the maximum applied stress. Due to the orientation of the hole with respect to the normal stress, the hole itself

does not create a stress concentration in the relevant plane. However, the roughness along the surface of the channel has the potential to cause in-plane stress concentrators because of its three-dimensional variations.

5.3.2 Vibrational Analysis

Five solid specimens were prepared and tested in an identical fashion to the fifteen channeled specimens. These solid coupons existed to serve as a control for the effect of the channel's roughness on specimen fatigue life. Besides the absence of the inner surface and its corresponding roughness, removal of the channel changed two key physical characteristics of the bending specimens: stiffness and mass.

The stiffness of a beam is a function of the elastic modulus, mass moment of inertia, and length of the member. In equation form:

$$k = f\left(\frac{EI}{L}\right)$$

For specimens of equal length and material properties, the stiffness varies solely as a linear function of the moment of inertia of the cross section. Taking the values at the center of the specimens, the solid specimens' mass moment of inertia can be calculated in the following manner:

$$I_{rectangle} = \frac{1}{12}bh^3$$

$$I_{solid} = \frac{1}{12} * (0.250\ in) * (0.125\ in)^3 = 4.0690 * 10^{-5}\ in^4$$

Since the round hole of the channeled specimens is located on the neutral axis, the moment of inertia of the circle can be subtracted from that of the solid rectangle to find the mass moment of inertia of the channeled specimens:

$$I_{circle} = \frac{\pi}{4} r^4$$

$$I_{channeled} = I_{rectangle} - I_{circle}$$

$$I_{channeled} = (4.0690 * 10^{-5}\ in^4) - \frac{\pi}{4} * (0.030\ in)^4 = 4.0054 * 10^{-5}\ in^4$$

Similarly, mass values can be calculated using the properties of the specimens at their center locations. Since the channeled and solid specimens are made from identical material, the density can be assumed constant. This yields the following mass density calculation for the solid specimens, a function of cross-sectional area and density:

$$m_{solid} = A_{solid} * \rho = bh\rho$$

$$m_{solid} = (0.250\ in) * (0.125\ in) * \rho = 0.03125\rho\ \frac{lbm}{in}$$

For the hollow specimens, the area of the circular hole is subtracted from the area of the solid bar:

$$m_{channeled} = A_{channeled} * \rho = A_{solid} - \pi r^2 \rho$$

$$m_{channeled} = \left(0.03125\rho\ \frac{lbm}{in}\right) - [\pi * (0.030\ in)^2 * \rho] = 0.02842\rho\ \frac{lbm}{in}$$

The natural frequency of a system can be calculated using the stiffness and the mass of the system:

$$\omega = \sqrt{\frac{k}{m}}$$

Compared to the channeled specimens, the solid control specimens have a higher stiffness (due to higher mass moment of inertia) and a greater mass.

5.3.3 Additive Build

The Inconel 718 specimens built for this experiment were manufactured at the University of Pittsburgh on an EOS M290 3D printer using the default parameter set. The bulk parameter set included a laser speed of 960 mm/s, laser power of 285 W, and a hatch spacing of 0.11 mm. Upskin laser parameters were 600 mm/s and 153 W, with a hatch spacing of 0.09 mm. The downskin parameters used were a laser speed of 2400 mm/s, a laser power of 145 W, and hatch spacing of 0.16 mm. The layer thickness for the build was set to be a constant 40 μm. Specimens were built in stacks of three channeled specimens and one control specimen. The build layout can be seen in Figure 13. A small thickness of surplus material was included between each specimen to allow room for the wire EDM. Seven objects were included in the build: specimen stacks A, B, C, D, and E; a sixth specimen stack designated “R” for “reject,” due to a dimensioning mishap during cutting; and a small coupon of interest in a separate study.

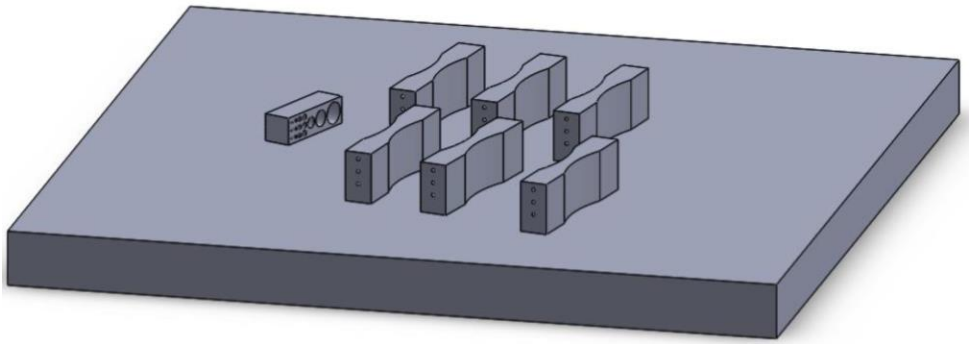

Figure 13: Build plate configuration

5.4 Specimen Preparation

5.4.1 Heat Treatment

In order to homogenize the microstructure of the test specimens, a heat treatment process was ordered. This treatment process was performed by Winston Heat Treating, Inc., and can be broken down into five steps. First, the specimens were solutionized at 1,750 °F (954 °C) to create a more uniform microstructural phase. Next, the specimens were aged at 1,325 °F (718 °C) for eight hours. The batch was then cooled to 1,150 °F (621°C), and then aged again for another eight hours. Finally, the specimens were quenched in nitrogen to freeze the homogenized microstructures into place.

5.4.2 Wire Electrical Discharge Machining

Specimens were separated and excess material was removed via wire electrical discharge machining (wire EDM). This process entails a thin wire serving as a tool electrode. Sparks are created by the electrode and used to melt away a slice of the object being cut. The system is “immersed in a dielectric medium” of deionized water which serves to clear away the removed material [75]. Wire EDM is a useful tool for advanced

manufacturing, but it is important to recognize that the cut surfaces of the parts sustain thermal residual stresses from the process [76].

5.4.3 Polishing

In order to counteract some of the unpredictable effects of surface roughness, the external surfaces of specimens were polished. This way, only the roughness within the channels remained and some variability between specimens could be eliminated. The curved surfaces of each specimen were first smoothed using a rotating sanding drum. Sweeps were made until no visible roughness remained. Next, the two broad surfaces were hand-sanded on 180 grit silicon carbide sandpaper table disks. Distilled water was periodically sprayed on the paper to help prevent particle accumulation. The coarse paper served to remove much of the roughness left by the wire EDM cuts, but it was not fine enough to leave a fully polished surface. Therefore, 600 grit sandpaper was used to create a near-reflective finish. For the most effective sanding, pressure was applied equally across the specimen as it is ground on the paper. Additionally, sweeps were made in the direction of the length of the specimen, along what would become the bending direction during the fatigue tests. This kept potential scratches in a less-dangerous orientation since any marks made by the sandpaper would be opposite the direction of the bending. Target average surface roughness was less than approximately 10 mircoinches (0.254 micrometers).

It was not necessary to thoroughly polish the grip sections of the test specimens. These sections were considered fixed boundary conditions and faced theoretically no stress as they did not displace relative to the shaker.

5.4.4 Mounting Holes

Once a specimen was fully polished, it was ready to be fitted with mounting holes. These holes were drilled through the broad side of the grip sections for the mounting bolts that held the specimen to the carrier plate. Care was taken not to scratch the samples' gage sections while drilling, and it was sometimes necessary to touch up the surfaces with 600 grit sandpaper.

5.4.5 Strain Gage Application

Before testing, each specimen was fitted with a strain gage to assist with the strain-velocity calibration. Model CEA-05/06-062UW-350 strain gages were used, rated to 350 Ω resistance. To encourage proper adhesion, a small amount of abrasion was given to the specimen where the gage was to be placed. This location was in the center of the gage section of the specimen, along the edge of the curved side. In order to apply the strain gage, the surface of the specimen needed to first be cleaned. A cotton swab was used to rub acetone on the specimen for dirt removal. A conditioner and a neutralizer were applied in sequence to further prep the surface for adhesion. The strain gage was then treated with a primer and glued to the center of the dogbone. The strain gage was placed with the tabs facing up. These tabs were the electrical transmittal locations where wires were soldered to complete the strain indicator circuit. The orientation of the strain gage on the test coupon is portrayed in Figure 14.

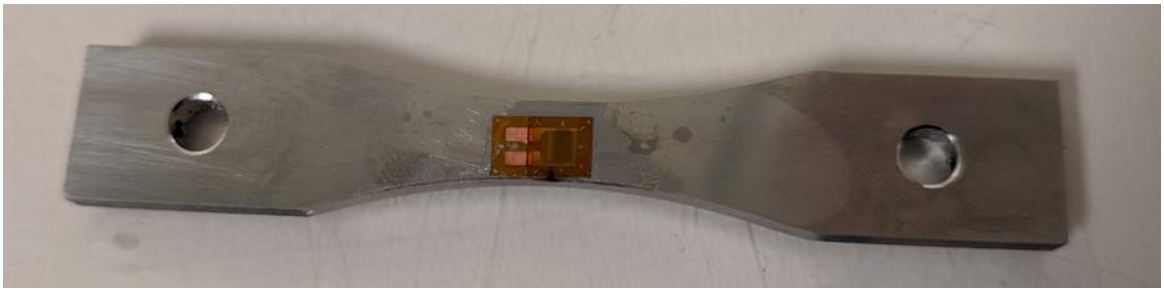

Figure 14: Specimen fitted with strain gage

Before soldering, the specimen needed to be loaded into the carrier plate. The dogbone was placed in between the two pairs of tabs with the strain gage facing downward and on the outside edge of the plate. This was the orientation most ideal for soldering. For each specimen loaded into the plate, a new pair of 11/32" nuts was used to tighten the tabs. The required 55 in-lbs (6.21 N-m) torque was near the yield strength of the fasteners, and they were easily and inexpensively replaced. After the specimen was bolted into the plate, two small pieces of coated electrical wire, about two or three inches long, were cut for connecting the strain gage to the plate's output wires. The coating on either end of these short wires needed to be stripped back about 1/8" (3.18 mm) to allow for proper solder adhesion. Using a temperature approximately 500-550 °F (260-288 °C), each wire was soldered to a strain gage tab and to an output wire on the carrier plate. Proper connections were confirmed by measuring across the carrier plate output wires and observing 350 Ω resistance. With the connections confirmed by ohmmeter, a polyurethane coat was applied over the strain gage to hold the arrangement in place.

5.5 Test Procedure

The shake table requires proper training for safe usage. Before powering on the shaker, the supply air and water lines must be on and open. The signal amplifier should be

on for approximately thirty minutes before testing in order be adequately warmed, so it is recommended to turn the amp on before the shake table. Turning on the entire block of amps helps expedite the warmup process.

Ensure the mounting blocks for the test plate are free of debris by wiping them before installing the plate. The plate is sandwiched between the two mounting blocks with the strain gage side of the specimen facing down. Using the gage-down orientation maintains consistency and helps prevent wire entanglement. A torque wrench is used to fasten the restraining nuts of the mounting blocks. Torque is gradually increased until the smaller, outside pair of fasteners are at 80 ft-lbs (110 N-m) and the inner nuts are at 120 ft-lbs (160 N-m). Next, the wire connections are taped down loosely, allowing room for vibration between the base and the mount of the shaker. The wires coming from the strain gage are then connected to the amp input tray, with the black negative of the gage pairing with the green negative of the amp and the two red positives matched. Figure 15 shows the carrier plate with a specimen mounted onto the shake table.

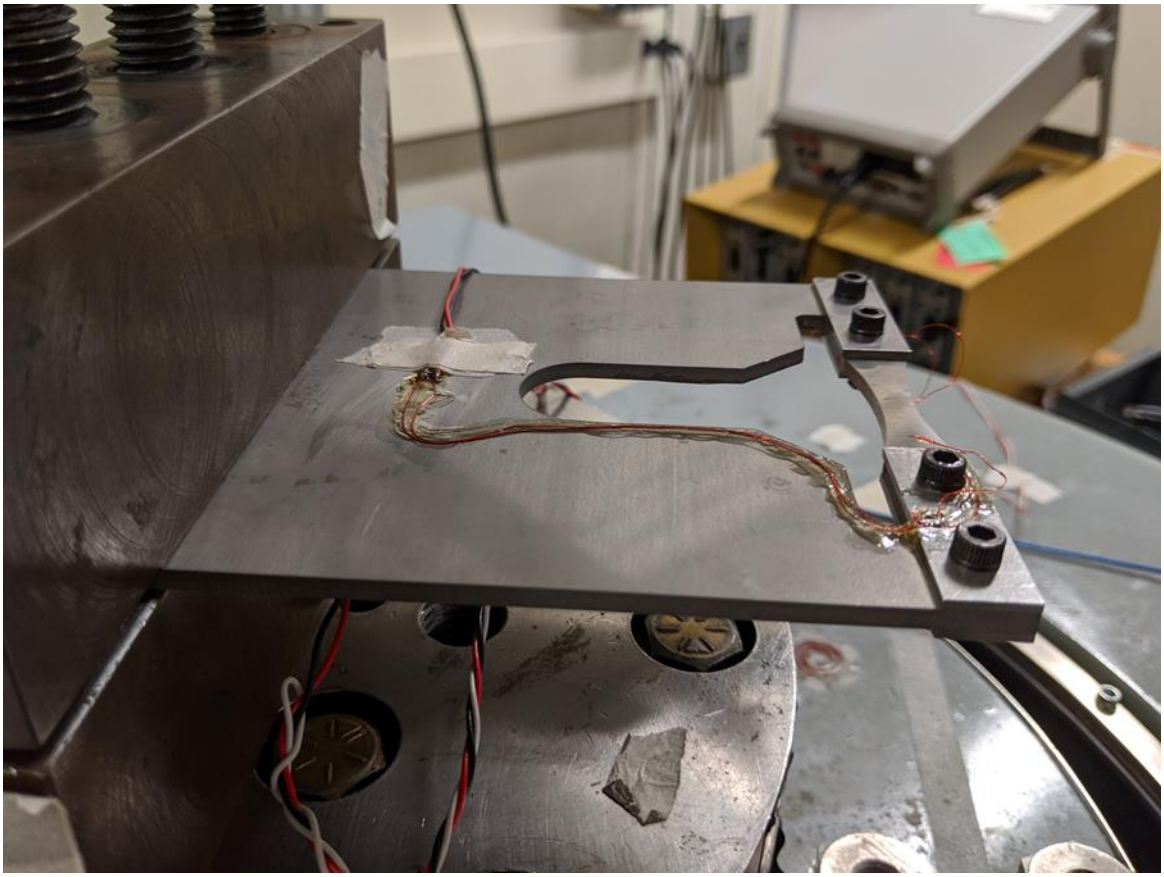

Figure 15: Specimen in carrier plate and mounted on shake table

The laser vibrometer must next be powered on and moved until the dot lies on the specimen approximately 1/4” from the grip of the plate. This location has been determined to be optimal for measuring the specimen’s response while also staying safely within the precision limits of the vibrometer [73]. A small piece of reflective tape is stuck to the test bar directly under the laser dot, increasing visibility. The laser velocity decoder is set to VD09 (1 m/s/V) and an autofocus is performed since all system parts are now in testing position.

To perform the strain gage calibration, the amplifier must first be connected to the multimeter via the 10 V port. The amp must then be switched to DC power. The excitation

voltage is turned on while the autobalance is reset, and then the excitation is turned back off. The amp balance is trimmed to zero before reactivating the excitation voltage and trimming the autobalance to zero. Next, a calibration factor must be calculated by dividing the excitation voltage (2 V) by the appropriate gage factor (2.170 for the strain gages used in this experiment). The calibration factor for these tests was therefore approximately 0.922 V. With the amplifier's Gain x100 and calibration B switch on, the gain is adjusted to read the value of the calibration factor. Finally, the calibration B and excitation are turned off, and the power is returned to AC. The strain gage output is switched from the multimeter back to the computer, and the laser vibrometer output is connected to the operator computer as well.

At this time, the shake table is ready to be powered on. First, the three fuse switches must be turned on sequentially. Then, on the shaker's tower, the "On" button is pressed. Once the "Ready" light appears, the "System Power" button is held for three seconds. Finally, the "Operate" button can be pressed, and the "Amp Gain" switch can be pushed all the way up. From this point, all control is done through the VibrationVIEW software.

Once the plated specimen is installed in the shaker and all electrical connections are made, the test is ready to commence. First, a broad sweep is conducted to determine the approximate resonant frequency of the system. This is necessary due to the slight variations in specimen geometry, fastener tightness, and other untraceable sources of changes in system stiffness. For the current specimens, the resonance frequency was consistently in the 1100-1120 Hz range, so the first sweep covered approximately 800-1500 Hz to ensure the entire desired mode shape was captured. To confirm the chordwise

bending mode has been identified, the laser vibrometer can be used to measure velocities at various points across the surface of the plate. Larger velocities correlate to greater displacements, and thus the running mode shape can be projected. This process is an important safety measure, since specific mode shapes' frequencies can vary per specimen and loading, and different modes can be indistinguishable from a single vibrometer reading. Once the desired mode has been fully established, the sweep frequency range is slowly narrowed around the chordwise bending mode, holding the acceleration constant at 0.1 g so the specimen does not sustain any premature fatigue damage. Once the natural frequency has been determined within a range of 10 Hz, the maximum velocity (mm/s), strain, and correlating frequency (Hz) are recorded. This is repeated as the acceleration is slowly increased by about 1 g per sweep, and the frequency range shifts downward by about 1 Hz per sweep. Each of these sweeps should be over a duration of three minutes to ensure that an ample amount of time is spent in the resonance peak to fully capture its shape. An example sweep from specimen A1, performed at an acceleration of 4 g, is shown below in Figure 16. Sweeps are conducted until either the maximum strain approaches the loading intended for the first step, or until the strain gage fails. The corresponding A1 strain-velocity calibration plot is shown in Figure 17.

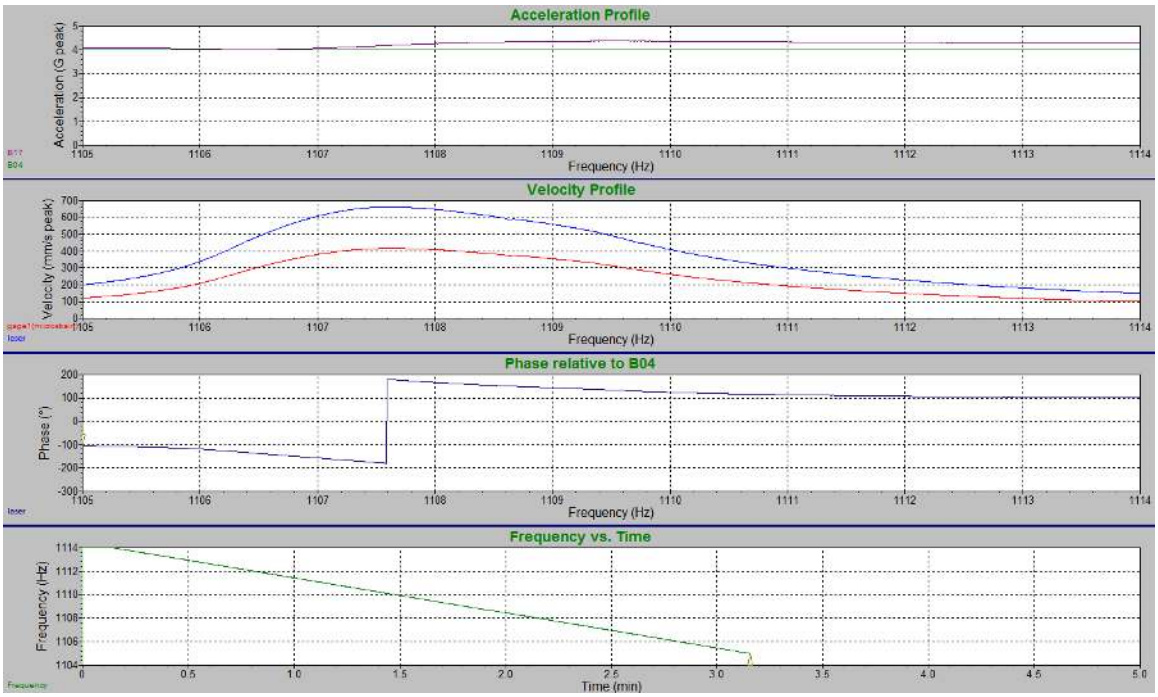

Figure 16: 4 g sweep on specimen A1, identifying a velocity of 662.8 mm/s, microstrain of 416.7, and resonance frequency of approximately 1108 Hz

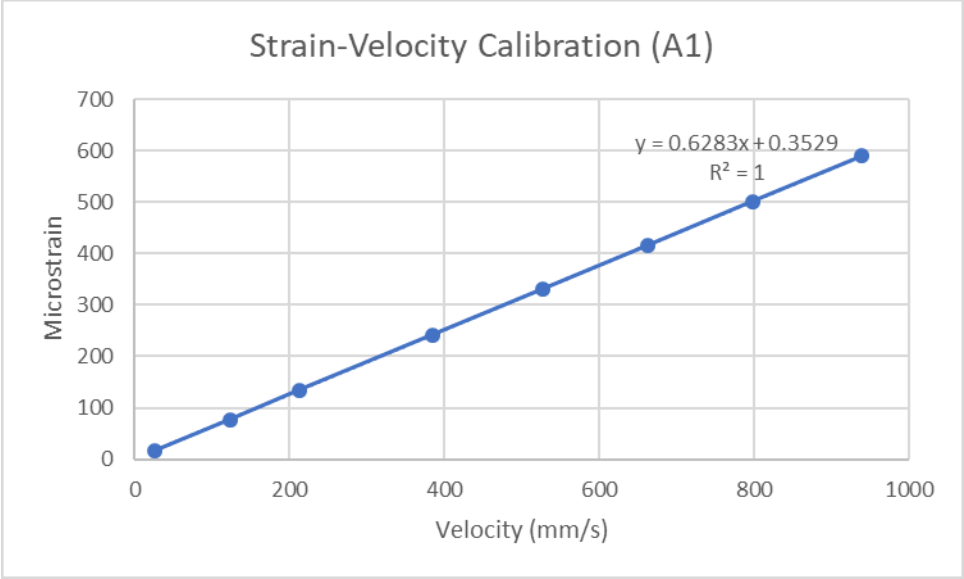

Figure 17: Strain-velocity relationship for specimen A1

The strain-velocity relationship is highly linear for a given specimen, and these values are used to calibrate the desired stress values. The target stresses are input by

converting to strain using the elastic modulus (30,100 ksi / 208 GPa for the additive Inconel specimens, as determined by the tensile test discussed in 6.2.1).

$$\mu\varepsilon = \frac{\sigma\ (ksi)}{E\ (ksi)} * 10^6$$

Then apply the experimentally obtained strain-velocity equation. Typical channeled specimens had a conversion of:

$$v\ \left(\frac{mm}{s}\right) = \mu\varepsilon * 1.6\ (\frac{mm}{s})$$

After establishing the strain-velocity relationship, extrapolations can be made to convert desired strains into inputted velocities. These velocities are entered into the test schedule in VibrationVIEW. If a particular stress is predicted to fail the part, several more steps than that should be programmed into the schedule to protect against premature test cessation. The final adjustments before beginning the test are to open the sweep window back up to a range of approximately 45 Hz and to increase the sweep duration to 15 minutes. This way, the full resonance peak is captured even as it shifts with the increasing acceleration.

After the initial sweep, a scheduled resonance table should be accessed. Here, the phase tracking must be activated in order to keep the frequency on the linear side of the resonance curve. If the nonlinear region is encroached upon, the vibrational response of the plate becomes unpredictable and unstable, and the velocity of the system tends to drop significantly below demand. It was determined experimentally that 185° was an

appropriate phase angle to maintain stability. Once this parameter has been set, the test is ready to run to completion.

Leading up to the first true stress step, lower stress values should be run at relatively low cycle counts to ease the system into the high-strain regime. Ideally, run steps of about 50,000 cycles that start at 800 mm/s and increase by 200 mm/s until the initial test velocity is reached; then begin running the desired number of cycles per step. The test concludes automatically when the shaker can no longer meet the current velocity demand due to the decreasing specimen stiffness as a crack propagates throughout the part. This often occurs suddenly and with little warning from the VibrationVIEW acceleration, velocity, phase angle, or frequency plots.

Once the test halts, check the specimen for any visible surface cracks. Crack visibility can be increased by shining a flashlight, or by using fluorescent penetrant inspection and a UV light. To ensure failure, even if a crack has been identified, it is best practice to run an additional sweep of the specimen. A noticeable decrease in resonance frequency is a strong indicator that significant crack growth has occurred. This change can be as little as 1-2 Hz or as much as 10+ Hz. For additional confidence, the test can be restarted, advancing through stress steps until resting on a stress two to three steps below the initial failure step. Failed specimens should either display significant velocity instability (variation in velocity is non-negligible compared to step size) or should trigger failure and system abort.

Once confident fatigue failure has occurred, the specimen can be unloaded from the shake table. Turn the amp gain on the shaker control tower all the way down and press the

ready button, then wait until the machine cools down (~15 minutes) before pressing the off button and flipping the power switches back to off position. It is then safe to turn off all equipment, as well as the water and air supply lines. Once the specimen has been removed from the carrier plate, it is ideal to remove the strain gage for accessibility to the entire outer surface of the specimen. This can be done by alternately soaking the specimen in an acetone bath and lightly scraping at the strain gage with a finger or razor. At this point, the test is concluded and the post-fracture analysis process can begin.

5.6 Difficulties and Potential Sources of Error

5.6.1 Phase Angle Control

When performing sweeps, it was shown that the frequency vs. velocity curve is asymmetric on either side of the resonance frequency. The maximum velocity response occurs at the natural frequency, but the rate of decreasing velocity is different on the higher- and lower-frequency sides of the curve. Additionally, the shape of this curve changes significantly with varying acceleration. The phase angle is a way to gage how close the system is to resonance at a given time. When at perfect resonance, the phase angle reading from the laser vibrometer is 180° (which is the same as -180°). The further from resonance, the closer the phase angle will be to 90° (or -90°). The sign is indicative of which side of the peak natural frequency the system is vibrating: if the angle is below resonance, the response is at a frequency higher than the resonant frequency, and if the phase angle is above resonance, the response is a lower-than-resonant frequency.

A steep frequency vs. velocity slope is an indication of volatility of the system. Within this regime, the VibrationVIEW control software can have difficulty keeping live

control of the velocity response. When this occurs, the system is able to decelerate much faster than it can accelerate (due to the running parameters being set to 0.2 dB/sec increasing rate and 0.5 dB/sec decreasing rate), and the velocity quickly plummets. In order to protect against this behavior, the system can be offset from resonance in the "safer" direction. In other words, a phase angle can be dictated to keep the system response on the side of resonance with the less-steep frequency vs. velocity slope.

During Test 1 (specimen E1), the phase angle was selected to be 175° (-185°). This decision was based on the shape of the frequency-velocity curves during the low-acceleration calibration sweeps. However, the velocity control during this test was fickle, frequently dropping well below the demand velocity. This was actively adjusted in the second half of the test by manually controlling the phase angle, and the data point is considered valid. For all subsequent tests, a phase angle of 185° (or -175°) was applied. This angle was found to be much more effective at stabilizing the velocity response for the majority of the test. The asymmetry of the curve seemed to flip at approximately 20 g acceleration, when the new phase angle became optimal. This explains why it was not predicted in the first test, since the first strain gage only survived through the 4 g sweep. The 20 g step correlated with approximately 40 ksi (276 MPa) stress, and no specimen failed below this point. Therefore, the 185° phase angle was deemed the preferred option, since it was the most stable choice during the critical stresses of every test.

5.6.2 Brief Velocity Overload

Occasionally, the specimen velocity would exceed the demand velocity by more than the normal variance of 20-30 mm/sec. Most often, these overloadings were the result

of the acceleration jump at the very beginning of a new step. This was most frequently seen in the lowest stress levels, so the ultimate and penultimate stress steps were rarely affected. These instances only occurred over a duration of 1-3 seconds, and the overshoot was usually only a small portion of the total applied strain.

During Test 15 (specimen E3), a software bug caused the scheduled Resonance Table to be deleted. Upon re-adding the step and restarting the test, a very large overloading occurred following the Resonance Table step. For a length of time less than 7.44 sec (8,244 cycles), velocity measurements exceeded the magnitude of first scheduled step (2,596 mm/sec). The maximum recorded velocity was 5,322 mm/sec. The cause of this was the control channel setting being left on “Default” instead of “On Ch2”. This test was allowed to continue to run since the overloading had already occurred and any damage that would result had already been done. Specimen E3, a 6,000,000-cycle test, exceeded its expected performance based on the final data trendline, so consequence of the brief excess loading appears to have been minimal. It should also be noted that this test failed due to fatigue at a stress lower than that which occurred during the overload.

5.6.3 Degradation of the Carrier Plate

During previous iterations of the carrier plate bending fatigue test, the plate was observed to eventually undergo failure [74]. During this experiment, a single additively manufactured IN-718 carrier plate was used for all tests. While no catastrophic failure of the plate was observed, it is possible that some change in material properties occurred throughout the duration of the testing period. Most likely would be a decrease in stiffness due to a slowly propagating crack, much like the method of failure of the tested specimens.

Theoretically, the change in stiffness from one test to the next should not affect specimen life, since the system's change in stiffness would be reflected in a change in the strain-velocity relationship in order to maintain appropriate levels of stress and strain. The more likely and more consequential plate degradation would be from the beginning of a single test to the end of the same test. This would occur after the determination of the strain-velocity relationship, and the drive velocities would already be determined and set. Decreasing the system stiffness decreases the natural frequency, which could shift the phase angle to the wrong side of the resonance peak. This could lead to a lack of velocity control or potentially a strain that is too low and does not sufficiently load the part to expectation, resulting in a misleadingly long fatigue life.

5.6.4 Variation in Hole Roughness

The nature of surface roughness is that it is difficult to predict and difficult to keep consistent. This is especially true of downward facing arches, which have been shown to vary even in overall shape due to the extreme degree of roughness [31]. This variation can affect total fatigue life in multiple ways. First, rough surfaces will have different crack initiation potential, based on roughness metrics such as Sa and Sv. Secondly, the level of circularity of the hole may affect the stresses that are experienced in the part [31]. Since detailed roughness measurements were not possible with the present specimens, a round-hole assumption was necessary when calculating stresses.

5.6.5 Variation in Surface Finish

Since specimen surfaces were hand-polished, there is a large potential for variation in surface finish quality. Specimens were polished in multiple batches. The first specimens

were measured to be sufficiently smooth with a profilometer, and the rest were sanded until they visually matched the confirmed smooth specimens. For reference, the profilometer read a gage section average roughness (Ra) of 2.7 μin (0.068 μm). Although attempts at consistency were made, it was impossible to eliminate all variation within the surfaces. This could lead to noticeable differences in time until crack initiation, particularly if most failures originate at the surfaces.

5.6.6 Error in Formation of Strain-Velocity Relationship

During the preliminary sweeps for development of the strain-velocity relationship, all strain and velocity values were accurate to the levels of the strain gage and laser vibrometer, respectively. When read from the graph, values were rounded automatically to four significant figures. This resulted in a lack of precision when the strain and velocity values rose to over 1,000 microstrain or mm/sec. Microsoft Excel was used to create a 1st order trendline, which was also provided to four significant figures. For this reason, the inversion of the equation (velocity-from-strain rather than strain-from-velocity) was also left in four significant figures, which again created opportunity for rounding error. Finally, demand velocities were entered as whole numbers. All of this potential error could accumulate into a shift of several mm/sec in the demand velocity. Unfortunately, there is not a workaround to this error, since the accuracy of measurements is always limited by the accuracy and precision of the instruments used.

5.6.7 Strain Gage Calibration Process

During strain gage calibration, there were several target calibration values that needed to be met. These included zeroing the amp balance voltage, as well as the shunt B-

calibration factor. These values were read and displayed by the system multimeter, and they were controlled by the system amplifier. Adjustments were performed using various screws, knobs, and dials, all of which were continuous controls. Therefore, it was impossible to calibrate to the exact target value. Further complicating the matter is the fact that these were electrical measurements, subject to minute perturbations and inconsistencies associated with instantaneous current flow. A value of 0.1 mV for a target 0 mV reading was still considered optimal, since the displayed value on the multimeter would vary more than that from second to second.

5.6.8 Demand Velocity Drift

Each stress step during the testing process was dictated by a corresponding velocity. Throughout the duration of a single step, the demand velocity could drift either up or down. This occurred in a seemingly patternless manner, but it tended to happen more frequently toward the beginning of a given step. The consequence of this drift was likely minimal, since the drift was far lower than the inherent velocity variation that occurred during every step. However, it is still best practice to reset the drift whenever it is noticed. This was done by opening the Edit Test menu and pressing OK. This reconfirmed the drive velocity and reset the driving value. This same process occurs at the beginning of each new step, meaning that velocity drift does not carry over from one step to the next.

5.6.9 Tests Over Multiple Days

Tests were optimally performed during a single run, but sometimes this was not feasible due to long step times and some level of unpredictability in specimen fatigue life.

In instances where delaying the conclusion of a test was unavoidable, steps could be taken to reduce the potential negative effects of a two-part test.

High power consuming equipment needed to be turned off, including the shake table and air compressor. The laser vibrometer was also powered down, so as to not waste the life of the laser. The multimeter, amplifiers, and operator computer with VibrationVIEW software could all remain on overnight, since these pieces of equipment consumed little power and could benefit from not needing a recalibration. The carrier plate, specimen, and the mounting system were not moved or adjusted in any way, if at all possible.

The laser vibrometer, since it was powered off, needed recalibrating. While not optimal, it must be assumed that the new calibration is equivalent to the original, since an uncalibrated laser vibrometer was too imprecise to be used effectively.

Determining that the test must be delayed needed to be done at least one step before the one that would be the day's last. In the Edit Test menu, the schedule could be adjusted mid-test for any step that had not yet begun. On the step that desired to be the day's final step, the number of cycles could be decreased by 100,000-500,000 cycles. Then, a Wait For Operator command was inserted following this step. This way, the test could be aborted after a known and precise number of cycles. Upon restarting the test, a new step was added. This step was at the same stress as the step that needed to be completed, and the number of cycles was equal to the amount of cycles cut from the previous day's step. Earlier stress steps were advanced by using the F11 button on the keyboard.

During the course of this experiment, three specimens required two-day testing periods. Each specimen (the 10,000,000-cycle tests D1 and ES, as well as the 6,000,000-cycle test E3) outperformed the series trendline, indicating that there were minimal negative effects from resting overnight. Each of these three tests also survived at least 1 million cycles on the next stress level before failure, a real-time duration of more than fifteen minutes.

One should be careful not to attribute cause and effect without sufficient evidence. For example, it is theoretically possible that the two-day testing process improved fatigue performance, causing the three specimens to overperform. However, it may be more likely that the naturally overperforming specimens tested at high cycle counts required two days to fatigue simply due to an insufficient time allotment for the tests. The sample size of two-day specimens is too small to make any substantial claims about the connection between fatigue life and the occurrence of a resting period.

5.6.10 Physical Shifting of the System

Throughout the course of a test, the carrier plate and specimen arrangement occasionally shifted slightly within the tolerances of the fasteners. This was a fairly common observance as the applied acceleration of the system slowly increased. When this slippage occurred, it was observed as a rapid linear shift of the frequency-velocity plot that did not greatly affect the stability of the test. If the shift occurred during the strain-velocity calibration sweeps, that particular sweep was run again to ensure that the data point matched the new state of the system. However, if the test had already begun, it was not practical to begin the entire sweep process over again. Therefore, slippage during the test

was simply considered allowable error. For this reason, it is best to run calibration sweeps as close to the first step's strain as possible without going over this threshold. This way, the system can shake out as many potential shifts as possible before fatigue testing begins.

Physical movement of the system can occur because of the gaps between various fasteners and the parts they hold together. These locations include the mounting screws holding the specimen in the carrier plate, the block holding the carrier plate onto the shake table, and the nuts and pins securing the mounting block on top of the carrier plate. All of these connections were made using consistent amounts of force or torque, but slippages were consistently observed regardless.

Chapter 6: Vibration-Based Bending Fatigue Results and Analysis

6.1 Introduction

Once all the vibration bending specimens were fatigued, two primary types of analysis were performed. First, quantitative methods were used to investigate the fatigue life of the channeled and solid specimens. This was done through the construction and analysis of an S-N plot. Second, the specimens' fracture planes and external surfaces were photographed and examined for patterns in the crack growth process. This qualitative study allowed for the determination of a consistent crack initiation point across all specimens.

6.2 Quantitative Analysis

The primary goal for the vibration bending experiment was to produce an S-N curve comparing the fatigue life of channeled specimens and their solid counterparts. The plots in this section serve to present this data and increase confidence in the results of the experiment by elimination of some of the potential sources of error discussed previously. In order to ensure the most accurate stress-strain relationship for the test specimens, the modulus of elasticity was first calculated by performing a tensile test on some excess material from the same build.

6.2.1 Modulus of Elasticity

In order to relate desired stress and the necessary strain, the modulus of elasticity is required. The three quantities are related by the equation:

$$\sigma = E\varepsilon$$

The modulus can be obtained by determining the slope of the elastic portion of a material's stress-strain curve. For non-additive Inconel 718, material databases list the Young's modulus as approximately 28,000 ksi (193 GPa) [22]. A piece of excess material from the build was pulled axially to determine the precise modulus of the AM Inconel used in this experiment. The coupon was pulled until failure, and the results are portrayed in Figure 18.

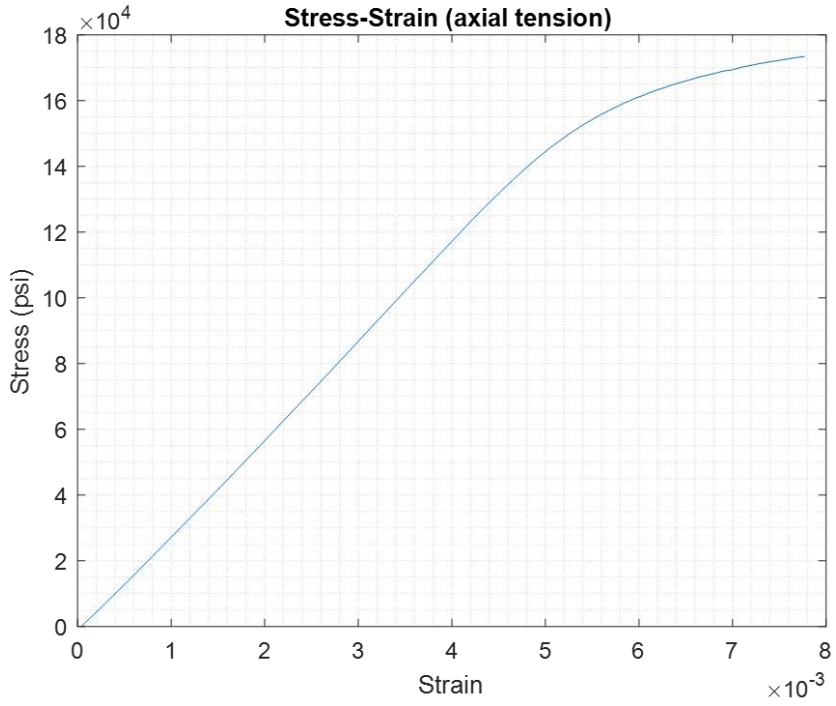

Figure 18: Stress-strain plot for elastic modulus calculation

From the collected data, 250 stress-strain measurements from the middle of the elastic regime were compared point-by-point, and the slopes were averaged in Matlab to

obtain a single mean elastic modulus value of 30,100 ksi (208 GPa). From the plot, a yield stress of approximately 140 ksi (965 MPa) can also be obtained. This is gathered by reading the stress at the beginning of the plastic (nonlinear) regime. The obtained values indicate that the additive 718 used is slightly stiffer and stronger than traditionally wrought material literature values [22].

6.2.2 S-N Data

Fifteen channeled and five solid specimens were tested at cycle counts ranging from 150,000 to 10,000,000 cycles. The resulting stress levels achieved are plotted in the S-N curve shown in Figure 19 below. Specimens and fatigue performance are correlated in the following Table 3.

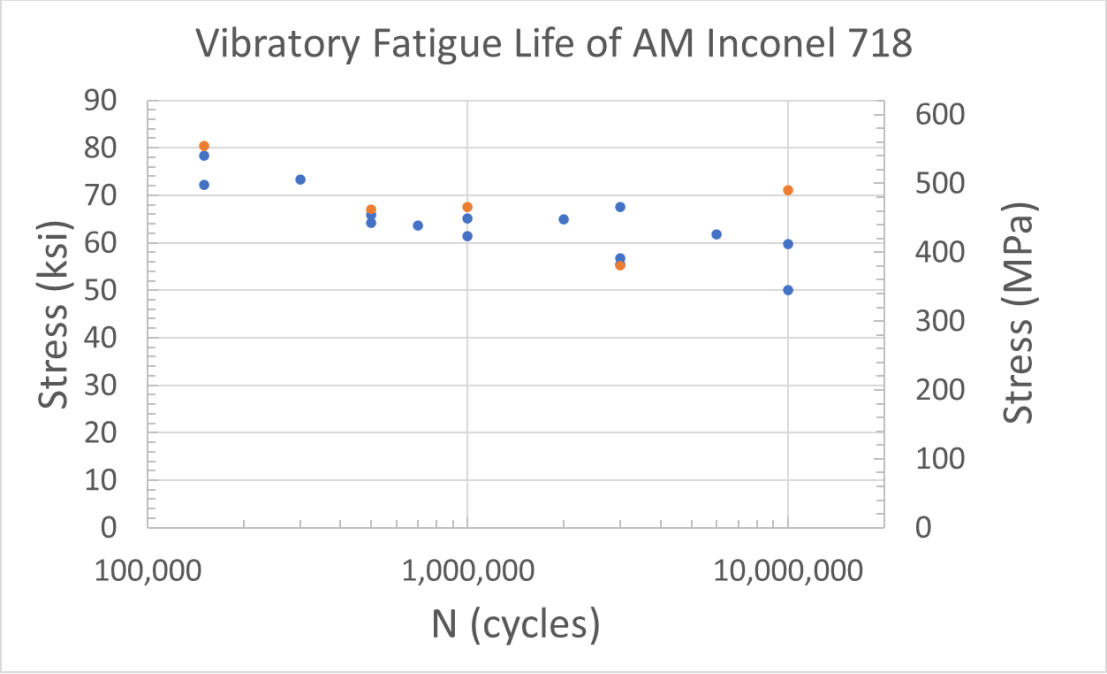

Figure 19: Bending fatigue life of channeled (blue) and solid (orange) AM alloy 718 specimens

Specimen	N (cycles)	S (ksi)	S (MPa)
A1	150,000	72.21	497.9
E1	150,000	78.43	540.8
D3	300,000	73.27	505.2
A2	500,000	64.14	442.3
B1	500,000	65.80	453.7
C3	700,000	63.62	438.6
B2	1,000,000	65.18	449.4
C1	1,000,000	61.33	422.8
B3	2,000,000	64.87	447.3
C2	3,000,000	67.49	465.3
D2	3,000,000	55.51	382.7
E2	3,000,000	56.73	391.2
E3	6,000,000	61.76	425.8
A3	10,000,000	50.09	345.3
D1	10,000,000	59.70	411.6
BS	150,000	80.43	554.6
CS	500,000	67.06	462.3
DS	1,000,000	67.54	465.7
AS	3,000,000	55.35	381.6
ES	10,000,000	71.01	489.6

Table 3: S-N data for all tested specimens

There is relatively little spread within the data, particularly among the lower-cycle tests. The solid control specimens are also well-integrated into the channeled specimens' range of stress values. The most variation occurs among the 10^7-cycle tests. Because of this spread, it is not entirely clear if the curve is trending toward a potential endurance strength or not. Dismissing the solid specimen gives the impression that the data is trending continually downward in a logarithmic fashion; however, if the lowest channeled specimen is considered the anomaly, then the curve suddenly could pass for flattening to a value of around 60 ksi (414 MPa), potentially indicating a fatigue limit at this stress. The literature value for annealed Inconel endurance strength is approximately 67 ksi (462 MPa) [22], so 60 ksi is a reasonable value for the same material made by additive manufacturing.

The AFRL has previously run vibration bending fatigue tests using rectangular plate specimens made of nickel alloy 718. The results of the previous test are shown below in Figure 20.

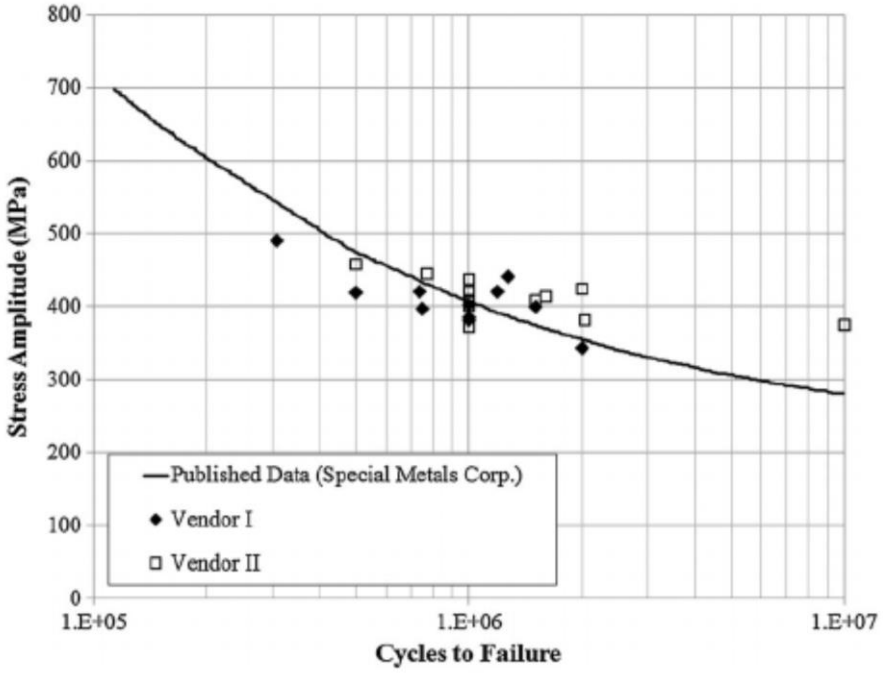

Figure 20: Previous iteration of the vibration fatigue test using solid plate specimens [77]

The results of the current fatigue test aligned quite closely with the previous iteration. Resultant stresses for specimens with lives ranging from 300,000 to 10,000,000 cycles were observed to closely follow approximately the same trendline [77]. This is evidence of the consistency throughout the generations of the vibration bending test procedure, supporting the accuracy of the specimen-insert model used in this experiment.

The channeled and solid specimens displayed essentially indistinguishable fatigue performance under equal stresses. The implication of this is that the roughness of the channel was not the limiting factor for the fatigue life of the channeled specimens. Rather,

a common feature, like the corner of the specimen, was likely the location of crack initiation. This can potentially be supported by fractography analysis.

6.2.3 Accounting for Potential Error

6.2.3.1 Degradation of the Carrier Plate

The same carrier plate was used for all tests performed in this experiment. If the structural integrity of the plate degraded over the course of the testing process, results of the fatigue tests could be compromised. Therefore, an analysis of specimen performance as a function of testing order was conducted. To perform this analysis, first a logarithmic trendline of the fifteen channeled specimens was created using Microsoft Excel. This trendline was plotted alongside the channeled specimens, whose dots were shaded according to their testing order: the darkest point was tested first, and the lightest point was tested last. The resulting S-N curve is shown in Figure 21.

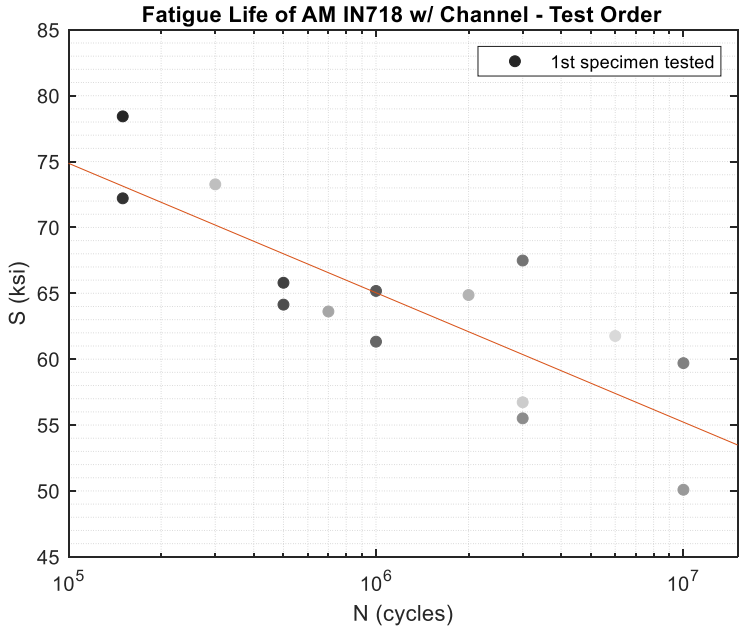

Figure 21: Fatigue performance sorted by test order

The equation of the trendline is:

$$S = -4.266 * \ln(N) + 123.98\ ksi$$

Studying the above plot reveals that the early and late tests are both distributed above and below the trendline of average group performance. This data is presented in an alternative way in Figure 22. For this graph, each specimen's fatigue performance was compared to its expected performance according to the trendline. A percent difference was calculated, and these values are plotted versus testing order.

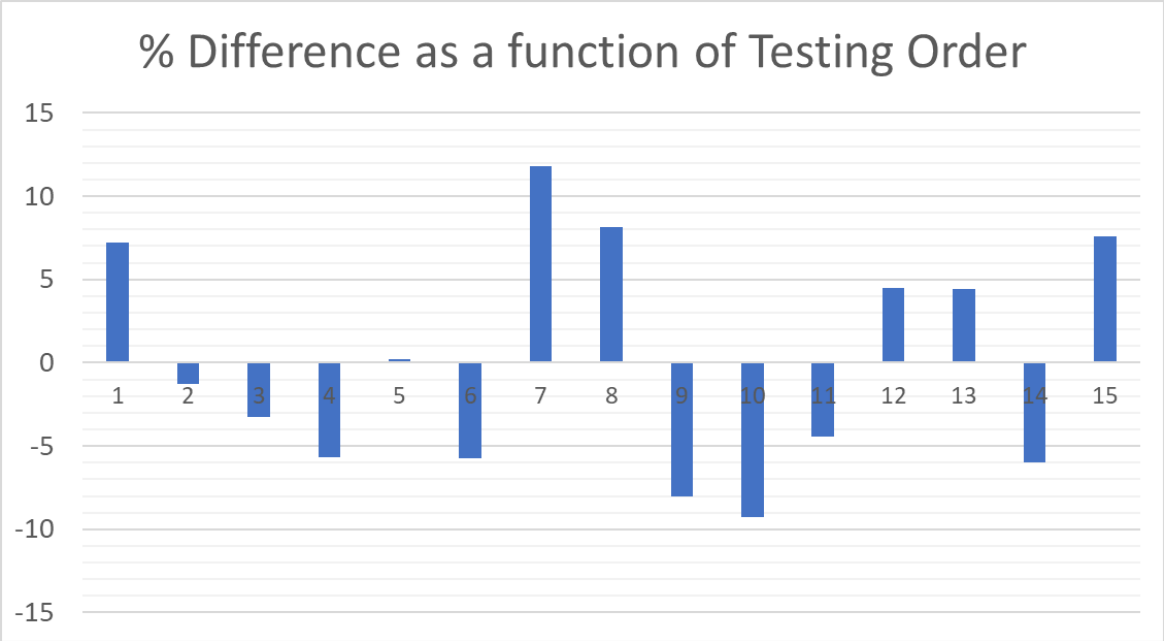

Figure 22: Bar graph of actual versus expected performance percent difference, as a function of test order

On this plot, a perfectly average test would have a percent difference of zero. The randomness of tests falling above or below the trendline indicates that there is no correlation between the testing order and fatigue performance. There is no apparent trend of increasing or decreasing performance as the tests were conducted. Therefore, the variable of testing order is deemed inconsequential.

6.2.3.2 Build Plate Location

Thermal history can vary by location on the build platform. These differences in build conditions can result in inconsistent microstructure, porosity density, and surface quality, each of which play a part in fatigue behavior. For this reason, the data is analyzed similarly as above, this time sorted by build stack. Figure 23 below shows the S-N curve with the same logarithmic trendline with colored markers indicating specimens built in the same stack.

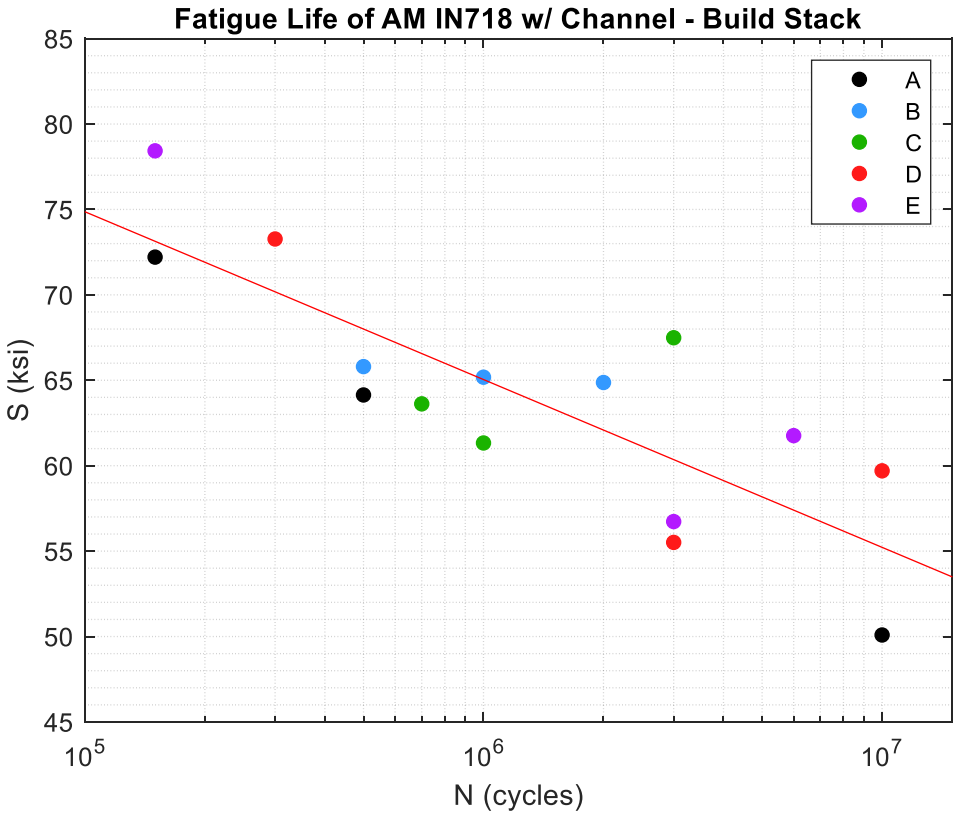

Figure 23: Fatigue performance sorted by build stack

It is observed that every build stack except group A had at least one specimen perform above and at least one specimen perform below the average performance. Returning to the percent difference method, Figure 24 is obtained.

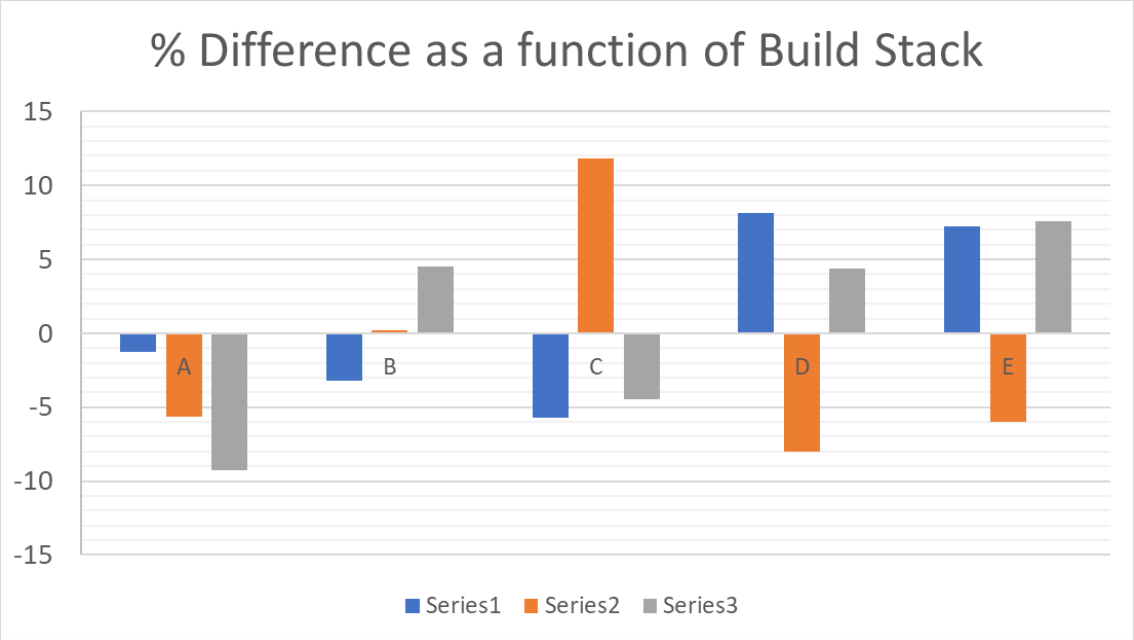

Figure 24: Bar graph of actual versus expected performance percent difference, as a function of build stack

There is no information correlating specimens to vertical position within an individual stack, nor stack location with respect to each other on the build plate. However, the erraticism and inconsistency within the percent difference data indicates that these are not likely major factors in fatigue performance within this group. Stack minimums vary by about 6%, maximums by 13%, and intermediates by13% difference. It is possible that some build location effect exists, but it is not distinguishable with the data available.

6.3 Fracture Analysis

While the quantitative S-N data expressed the fatigue performance of the test coupons, it did not provide insight into the origins of failure or the patterns of crack growth shape and magnitude among the specimens. In this section, photographs of fractured specimens taken with a light macroscope are presented and analyzed for consistency in crack origin and failure points.

6.3.1 External Surface

Immediately following the removal of the strain gage, specimens were visually searched for external cracks along the suspected fracture plane. For some specimens, fluorescent penetrant inspection was applied to aid in locating cracks. However, the majority had no noticeable external signs of failure, even upon examination with a low-magnification microscope. One sample that did have visible external cracking was E1; a length of the crack is shown in Figure 25, and the suspected crack origin at the corner of the specimen is shown in Figure 26.

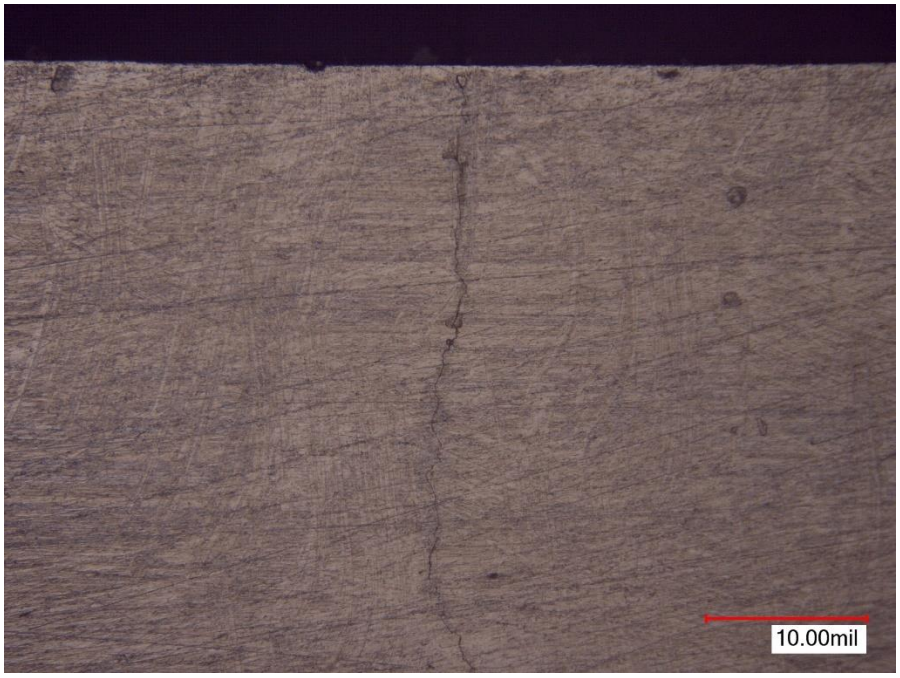

Figure 25: Specimen E1 external surface crack

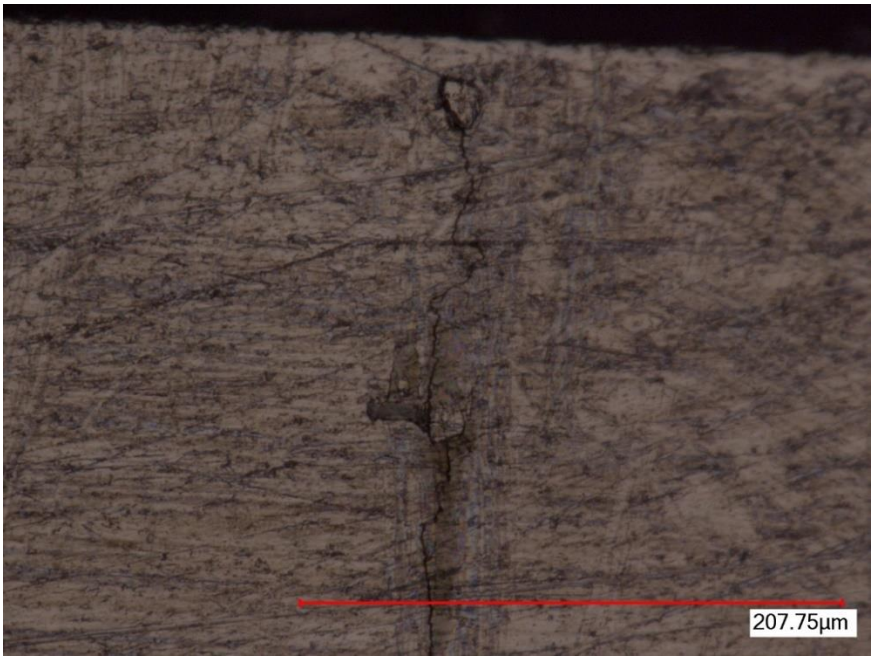

Figure 26: Specimen E1 external crack origin

The same specimen's crack was also present on the narrow side of the part. Figure 27 shows the crack spanning the thickness of many layers of the specimen.

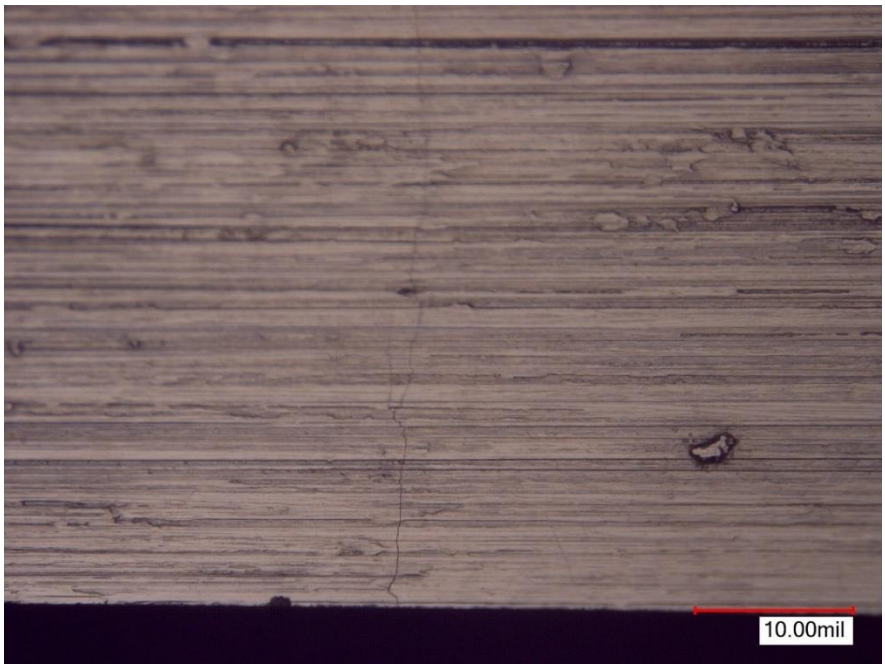

Figure 27: Specimen E1 external surface crack, curved face

On each of these two surfaces, it was possible to identify a location where the crack ended. This location on the flat surface is shown in Figure 28.

Figure 28: Specimen E1, external surface crack tip

Based off this observation, it was hypothesized that the detected crack originated at the corner of the specimen. However, a better perspective on this can be gained from observing the plane of crack growth in the middle of the specimen. In order to perform this analysis, the specimens needed to be pulled apart.

6.3.2 Fracture Surface

Throughout the fatigue test, crack growth was expected to occur at the plane of maximum bending stress, a cross section located directly in the center of the part. When a crack grows, the material is gradually separated, therefore decreasing the remaining cross-sectional area. It was postulated that by pulling a failed specimen axially, tensile failure

was extremely likely to occur on this same plane of crack growth due to its reduced area and thus increased stress.

Specimens were loaded into an MTS 100 kN load frame for axial pulling. Each grip section was clamped into one vice on the load frame, and tensile force was gradually increased until failure occurred. Fourteen of fifteen channeled specimens and all five solid controls had visible crack growth on the fracture plane. The only outlier, specimen B2, is shown in Figure 41 in Appendix 8.1: Fractography Images. It is unclear whether this specimen had only imperceptible crack propagation or if the specimen was torn along a plane other than its crack growth surface. A selection of all specimens' fractography images are shown and discussed below.

The channeled specimens can be grouped into five categories based on the degree of crack growth experienced before failure. First are the specimens with unknown crack propagation since they were intentionally overloaded following initial failure. This was done to ensure that at least some of the specimens would experience significant crack growth from bending loads; it was a precaution to see where a crack might originate and how it would grow in the event that the test alone did not cause visible damage to the specimens. This treatment was given to two specimens: C1 (1,000,000 cycles : 61.33 ksi / 422.8 MPa) and D1 (10,000,000 cycles : 59.70 ksi / 411.6 MPa). In both instances, the forced crack propagation drove the crack across approximately half the area of the part, including the entirety of one long edge of the part. This can be seen in Figure 29, where specimen D1 is pictured.

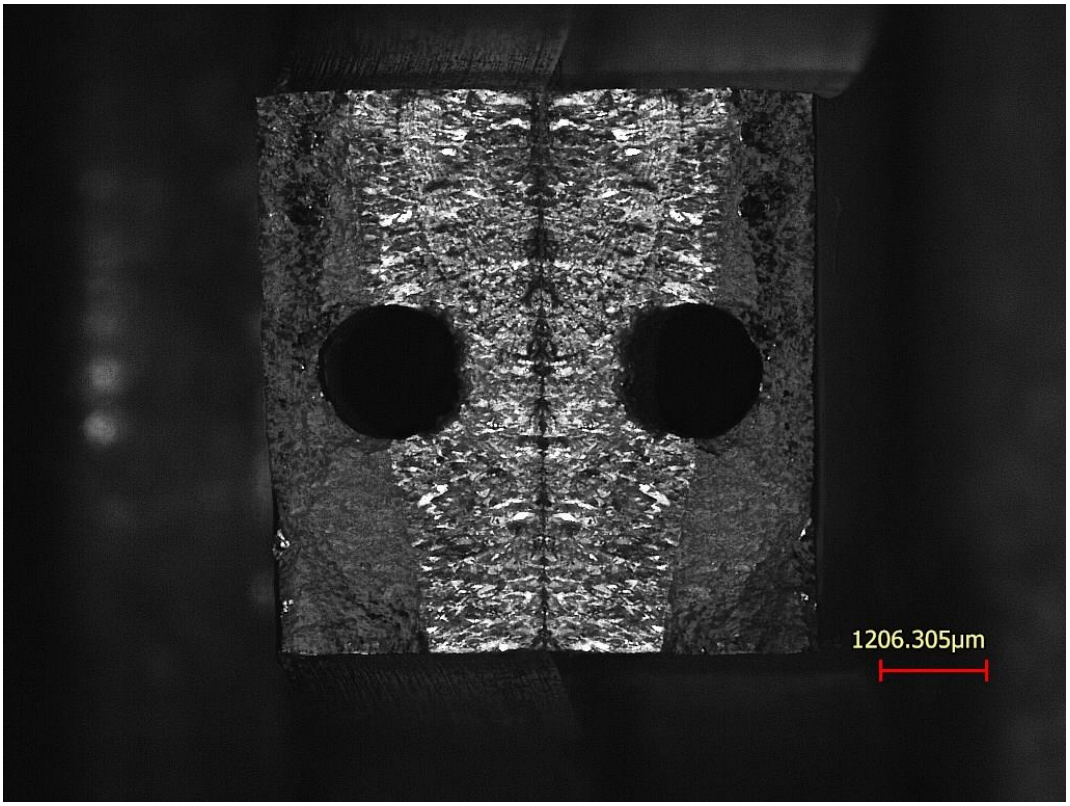

Figure 29: Specimen D1, subject to forced crack propagation

The second category of fracture surfaces are specimens that were not forcibly propagated but still experienced crack growth over a significant portion of their channel. This was true for four specimens: C3 (700,000 cycles : 63.62 ksi / 438.6 MPa), D2 (3,000,000 cycles : 55.51 ksi / 382.7 MPa), E1 (150,000 cycles : 78.43 ksi / 540.8 MPa), and E3 (6,000,000 cycles : 61.76 ksi / 425.8 MPa). In each of these instances, the perimeter of the channel is distinctly a part of the final crack profile. Specimen E3 is shown below in Figure 30 as an example of this category of specimen.

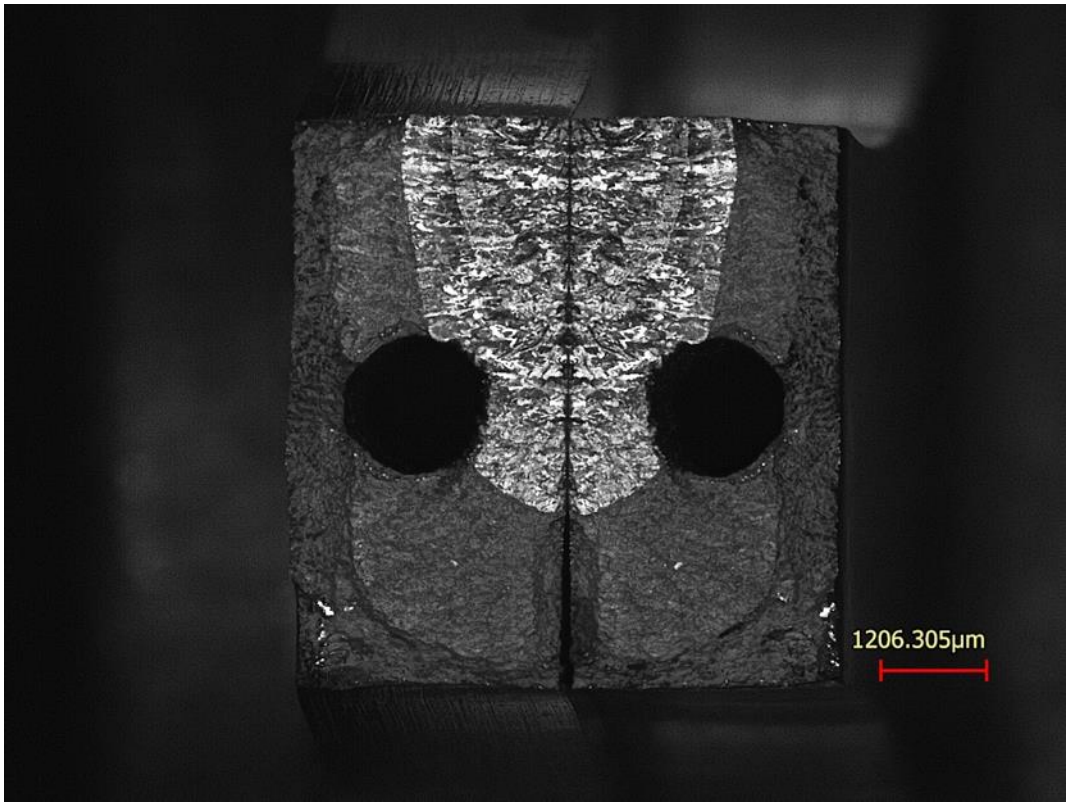

Figure 30: Specimen E3, with crack propagation over the channel

The third category of crack growth progress includes specimens where the crack tip was at or very near the channel when the test aborted. The most populated group, there are six channeled specimens that fit this description: A1 (150,000 cycles : 72.21 ksi / 497.9 MPa), A3 (10,000,000 cycles : 50.09 ksi / 345.3 MPa), B3 (2,000,000 cycles : 64.87 ksi / 447.3 MPa), C2 (3,000,000 cycles : 67.49 ksi / 465.3 MPa), D3 (300,000 cycles : 73.27 ksi / 505.2 MPa), and E2 (3,000,000 cycles : 56.73 ksi / 391.2 MPa). The distinction between this category and the last is that the crack growth profiles of these six specimens do not contain a portion of the channels' perimeters. An example of this can be seen in Figure 31, where specimen D3 is shown.

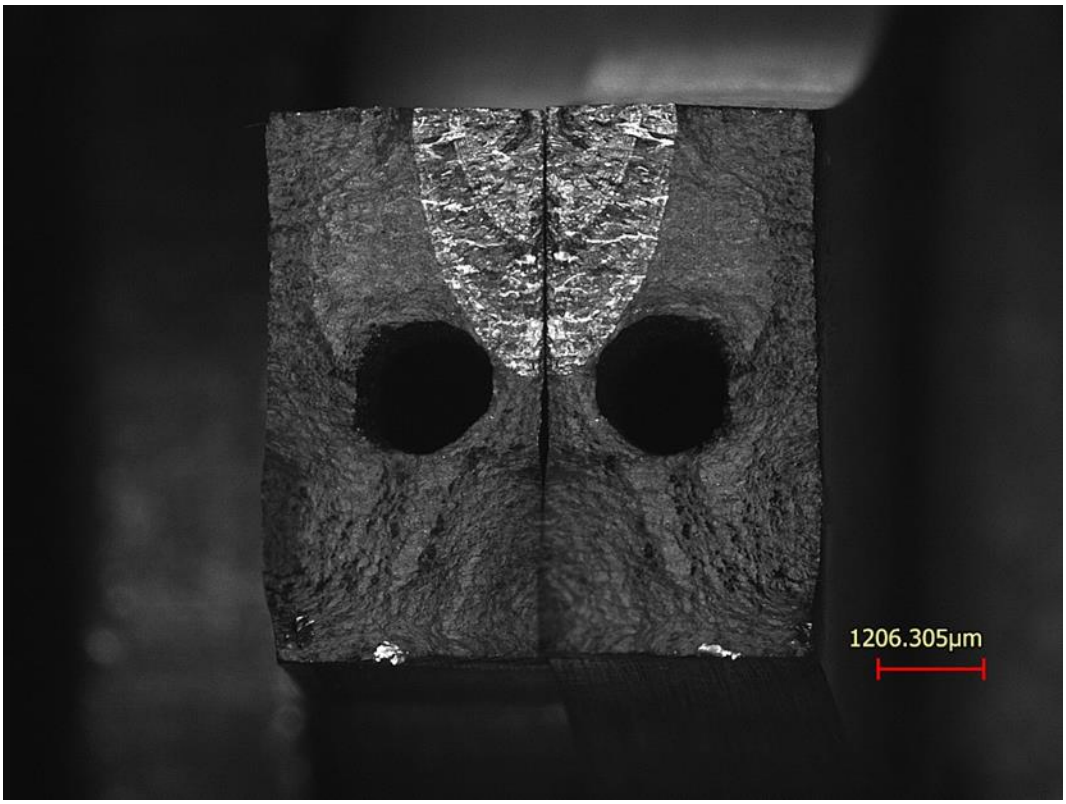

Figure 31: Specimen D3, with crack growth tangent to the channel

The fourth category of specimens are those that exhibited crack propagation in small degrees. These cracks were relatively far from the central channel when failure occurred. Two specimens fall into this category: A2 (500,000 cycles : 64.14 ksi / 442.3 MPa) and B1 (500,000 cycles : 65.80 ksi / 453.7 MPa). The crack growth profiles of these specimens cover far less than 25% of their respective fracture surfaces. Specimen A2 is shown below in Figure 32 as an example.

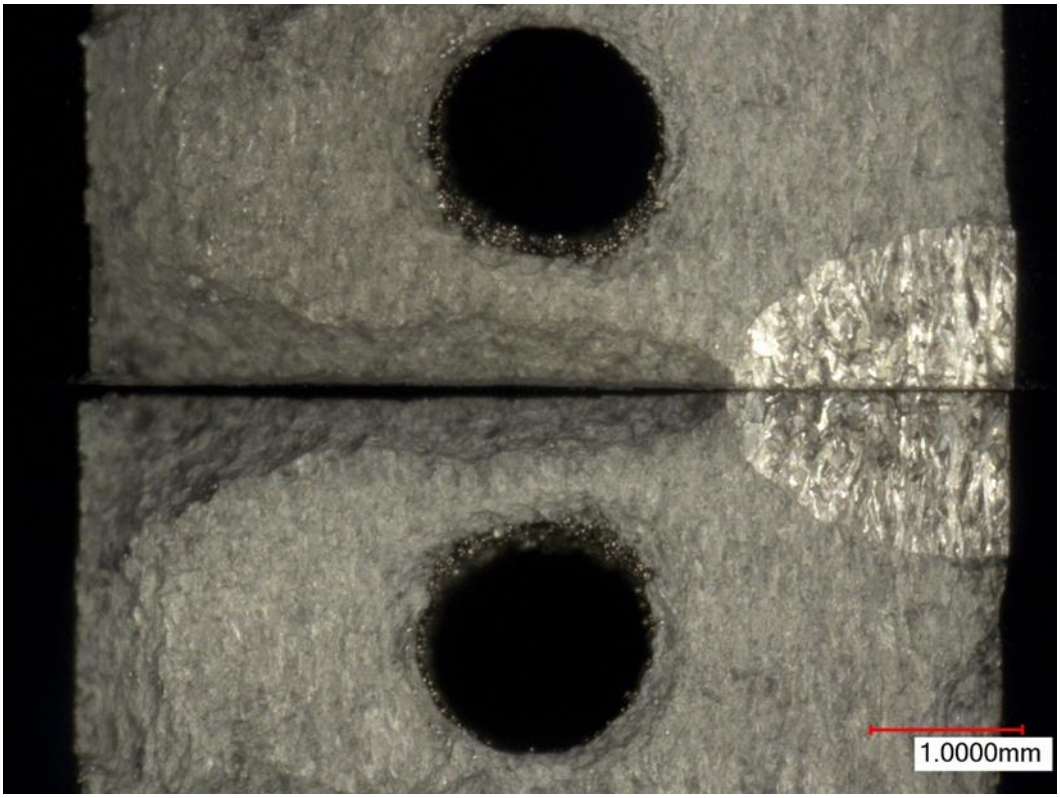

Figure 32: Specimen A2, with limited crack propagation

The final category is occupied by a single specimen, and it is identified by its unique lack of a visible crack growth profile. The tensile fracture surface of specimen B2 (1,000,000 cycles : 65.18 ksi / 449.4 MPa) is shown below in Figure 33. It is not entirely clear whether this specimen did not experience significant crack propagation during the fatigue test or if it did not separate on the crack growth plane when pulled axially. This could be further investigated by closely examining the external surface of the part and searching for signs of cracking at a location away from the tensile fracture surface.

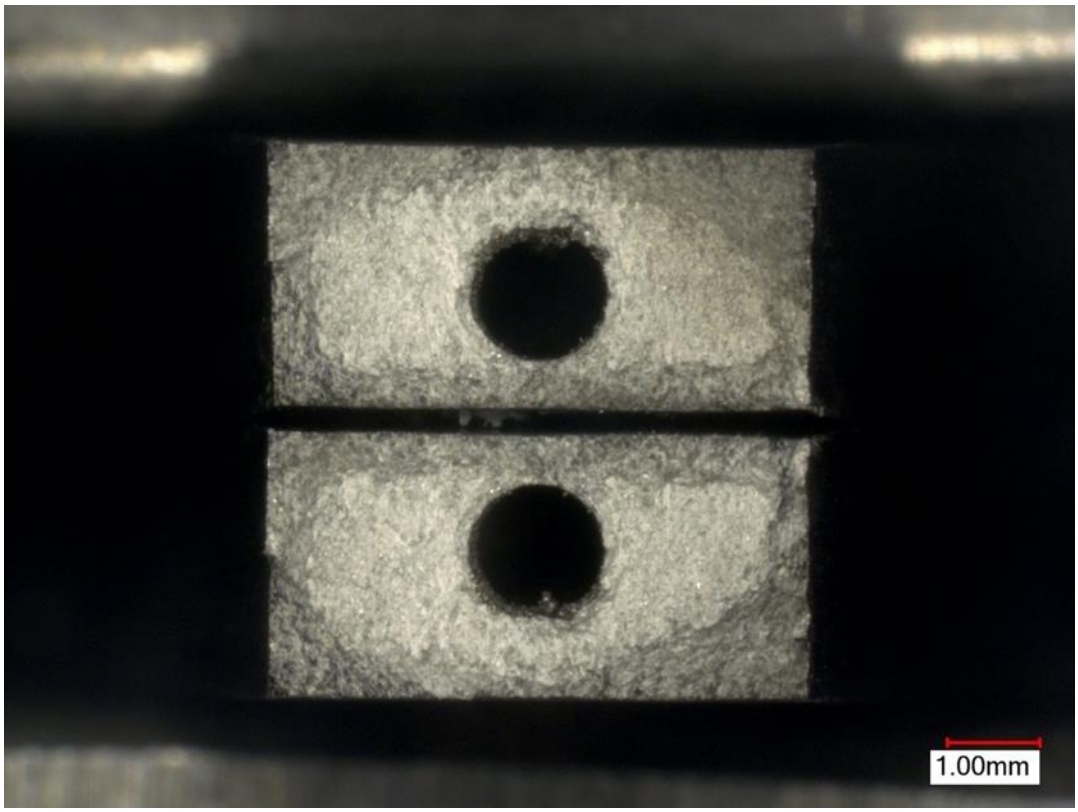

Figure 33: Specimen B2, with no visible crack propagation

The solid specimens were mostly consistent in their crack propagation. Four of the five samples exhibited fairly similar degrees of crack growth, with the total crack profile covering less than fifty percent of the total cross-sectional area. Specimens BS (150,000 cycles : 80.43 ksi / 554.6 MPa), CS (500,000 cycles : 67.06 ksi / 462.3 MPa), DS (1,000,000 cycles : 67.54 ksi / 465.7 MPa), and ES (10,000,000 cycles : 71.01 ksi / 489.6 MPa) all displayed visually comparable crack growth profile shapes of varying sizes. Specimen ES is pictured below in Figure 34 as an example of an average solid specimen crack surface from the experiment.

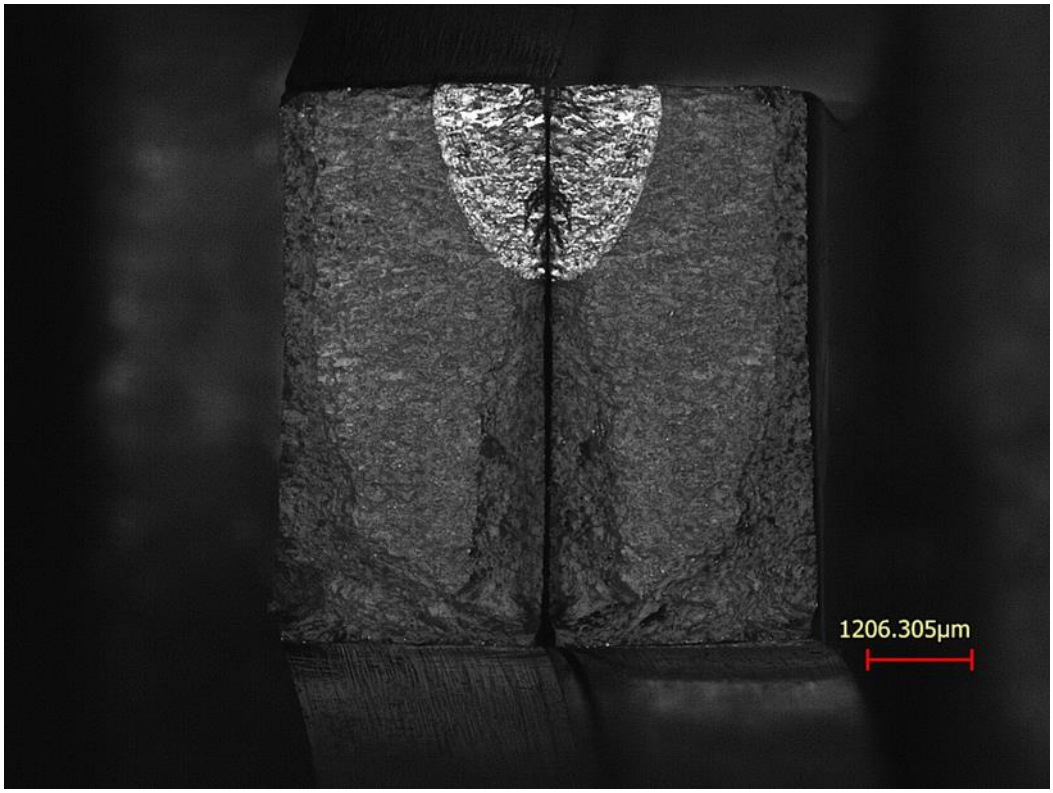

Figure 34: Specimen ES, displaying typical solid specimen crack growth behavior

Meanwhile, specimen AS (3,000,000 cycles : 55.35 ksi / 381.6 MPa) was distinct in its fracture. Upon failure, most specimens experienced a drop in resonance frequency of about 2-5 Hz. Specimen AS, on the other hand, dropped in natural frequency by approximately 24 Hz. AS was also the only specimen to display crack propagation over more than half of the fracture surface without any additional forced propagation. The AS specimen fracture surface can be seen in Figure 35, where the crack propagation profile is observed to occupy almost the entire fracture surface.

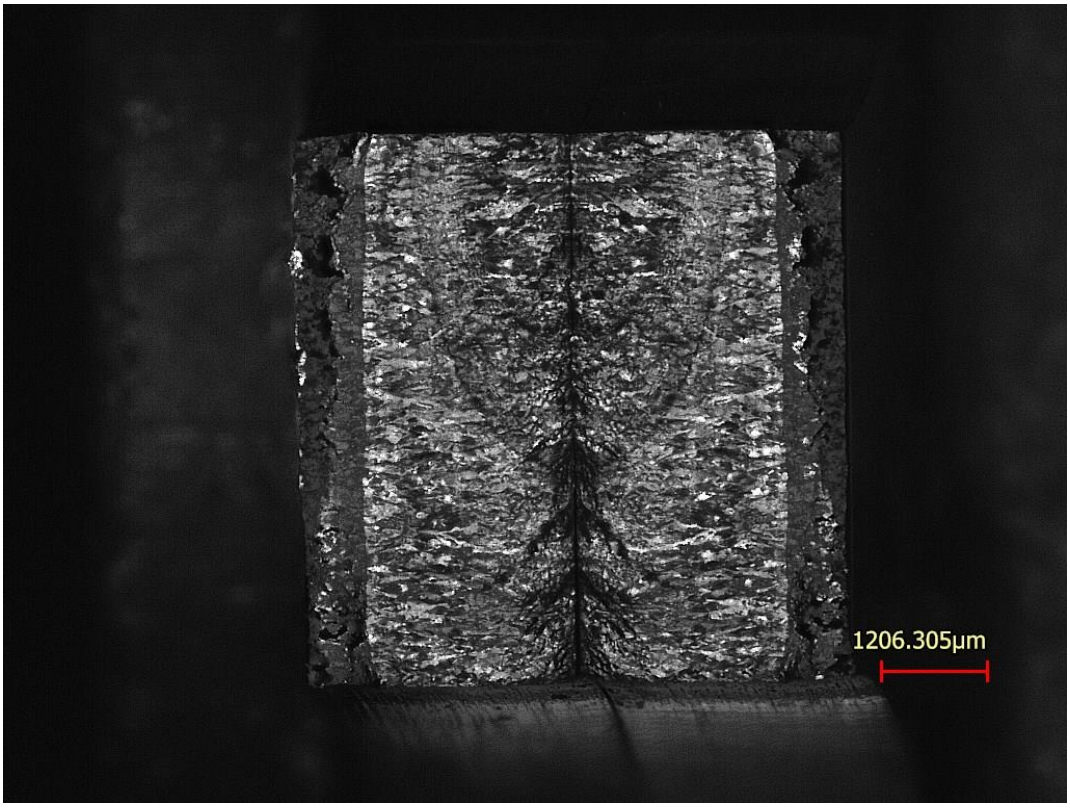

Figure 35: Specimen AS, with high degree of crack propagation

An effective method for determining the origin point of a crack on a fracture surface is by tracing the river marks to a single location. River marks are grooves that appear to radiate outward in the direction of crack growth. Examination of the fractography images from this experiment reveals that all specimens with visible crack propagation appear to have cracks initiating at the corner of the part. This heavily implies that the bending stress experienced at the surface of the specimens combined with the stress concentration of the sharp corner was greater than the stress experienced at the surfaces of the internal channels, even with the stress concentrations due to the as-built rough surfaces. This is further supported by the behavior of the solid control specimens. The S-N data of the solid specimens in Figure 19 aligns closely with the data from the channeled specimens. This

leads to the conclusion that the channeled specimens are behaving as though the channels are not present, since the applied loadings do account for the difference in cross-sectional area. Further, the channels do not visually appear to be significantly affecting the crack growth process either. This is based off the observations that, 1) The crack profiles on the channeled and solid specimens are of comparable shape and size, and 2) The channeled specimens did not fail when the crack reached any consistent point on or around the channel. Observation 1 suggests that the channel is not markedly contributing to the crack growth, since the form of the crack profile appears uncorrelated to the presence of a channel in a specimen. Observation 2 suggests that the channel is not likely to be triggering part failure, since the channeled specimens failed with crack profiles at a variety of orientations with respect to the channel. A correlation, on the other hand, might be indicated by the outer range of the crack profiles consistently spanning a particular part of the channel, such as the center or the near edge, but no such pattern exists insofar as the collected data indicates.

Examining the degrees of crack growth and sorting the categories in the manner described above, the following chart can be obtained from the S-N data. Figure 36 shows the fatigue performance of each specimen, with each bin representing a general degree of crack propagation. Specimens that underwent forced crack propagation are not included in this plot.

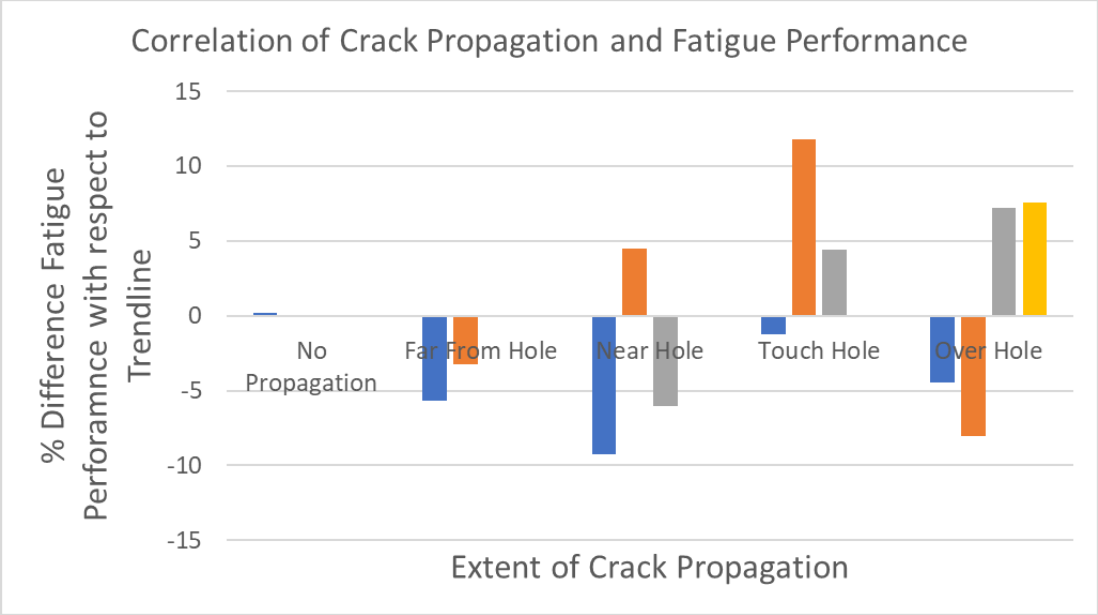

Figure 36: Relating the fatigue performance of channeled specimens to their relative degree of crack propagation

Specimens in the above chart are not sorted within the bins. The resulting plot does not present an explicit trend, but there do appear to be more high-performing specimens with high degrees of crack propagation than with little crack propagation. This could be due simply to the long-life specimens having more time for cracks to propagate, but it may also hint that these specimens had other qualities that allowed them to survive with smaller cross sections than their lower-performing counterparts. Such qualities could include lower channel roughness, or fewer internal defects like pores or inclusions. Specimens with relatively high life but little crack propagation may have been more resistant to crack initiation but still vulnerable to rapid crack growth.

6.4 Conclusions

Fifteen channeled and five solid specimens were fatigue tested under vibration-based bending loading, and they displayed very comparable fatigue life. Testing order and

build plate location were shown to be non-contributing variables to fatigue performance. Additionally, crack growth profiles indicated similar propagation and failure conditions between the channeled and control specimens. All these factors point to the conclusion that the presence of the channels had little impact on the test specimens' fatigue life. Instead, the overall geometry of the coupons appeared to be the limiting factor, since all visible cracks initiated at corners of specimens. Contributing to this also is the variable nature of bending stress across a cross section. Bending stress is theoretically zero at the neutral axis and increases linearly toward maximum tensile and maximum compressive stress on the top and bottom surfaces. What this means is that the surfaces of the channels were experiencing smaller stress magnitudes than the external surfaces of the of the specimens. Determining precisely how much lower the stress needs to be at a rough surface to achieve similar crack initiation behavior as a smooth surface will be critical in assessing if a potential geometry will be safe for fatigue application.

Some additive components with as-built internal features can be approximately as reliable as their traditionally manufactured counterparts in fatigue. Further, if features with as-built surface quality can meet reliability requirements, AM components become faster and more convenient to construct. However, the observed lack of crack initiation at the rough surfaces could change for specimens with different geometries, features, or loading distributions, and further experiments will be necessary to determine the sensitivity of each of these factors.

Chapter 7: Conclusions

As-built defects are one of the biggest inhibitors of additive manufacturing technology being used for critical applications, particularly within the aerospace industry. In order to advance the potential of AM components, their fatigue behavior needs to be understood more completely and more fundamentally. The experiments presented in this work served to fatigue and analyze additively manufactured parts, as well as to predict future failures by extending existing defect analysis models to AM applications.

Applying the theory of critical distances to microscale additive defects yielded numerous stress profiles and a table of threshold defect arrangements. Through the development and analysis of these stress maps, it was determined that the single-defect critical pore diameter is approximately 17 μm. Additionally, pairs of pores less than 17 μm diameter have minimal interactions when separated center-to-center by at least 60 μm. These could potentially make useful quality control guidelines for additively manufactured components; however, they are strict criteria, since as-built components frequently have many pores larger than 17 μm. This indicates that most AM parts are experiencing reduced fatigue performance due to internal porosity. These results are based on theoretical models and assume the reliable applicability of the theory of critical distances to the microscale, spherical pores, and coupled defects, all of which are extensions of the originally developed model. Results obtained in this experiment can be supported by thorough fatigue fracture analysis of porous specimens. Failures traceable to pores should occur at defects of more

severe magnitude than the limits provided here. Additionally, AM specimens with pores surpassing these guidelines should exhibit decreased fatigue performance compared to similar additive components with homogeneously nonthreatening porosities. The challenge lies in manufacturing AM parts with such reduced porosity.

The vibration-based bending fatigue experiments yielded an S-N curve and fractography images from fifteen channeled and five solid test specimens. Fatigue data obtained agrees well with the results of previous iterations of the test performed with the same material [77]. The limited spread between the performances of the channeled and solid (current and previous) specimens demonstrates the lack of contribution of the through channel to a specimen's stress state. It was shown through finite element modeling that the presence of the channel does not increase the bending stress, but the additional stress concentrations due to the channel's roughness were expected to have a larger impact than was ultimately shown. The fractography images consistently indicated that failures originated at the corners of the specimens, the same location of crack initiation shown by the solid specimens. This is a positive sign for AM component viability, since the addition of an internal feature did not detract from the fatigue life when the applied stress magnitude was normalized for the reduction in cross-sectional area. If the primary limiting factors are specimen geometry and load distribution, then this may not be much more restricting than for traditionally manufactured components. However, it is possible that the specimen design in this experiment, with the centralized hole and four sharp corners, was too lenient toward the internal feature when combined with the lower bending stresses experienced near the part's neutral axis. Further experimentation may be necessary to discover which

geometries, features, and loadings allow for safe, reliable, and consistent fatigue performance in additively manufactured components.

Defects are inherent to the additive process, so understanding the role these defects play in fatigue failure of AM components is critical. The results found in this study contribute to the collective understanding of pore-pore interactions and surface roughness of internal features, both of which are necessary for safe use of 3D printed parts in critical applications. If industry wants to take advantage of the many benefits of the additive manufacturing process, then these findings and more will be necessary for a responsible transition from traditional to AM components.

7.1 Recommendations for Future Work

The defect modeling work can be readily expanded upon by modeling different feature sets. These can include a surface notch and a pore, or two pores of different diameters. Additionally, the line, area, and volume methods of the theory of critical distances can still be explored. Moving into the multi-dimensional methods allows for analysis of features such as adjacent surface cracks and non-linear pore arrangements. Each of these applications of the TCD would benefit from direct fatigue test validation, but doing so would likely require heavy use of computed tomography, which can be time consuming and expensive.

The vibration-based bending fatigue experiment also has potential for future expansion, especially since the testing method is still early in its establishment. Specimens with features of increased complexity would be beneficial for finding tolerable and functionable designs. Channels could be built in greater quantity, in different orientations,

or with purposefully increased roughness and tested for bending fatigue life. The testing of specimens with increased internal complexity could benefit from using components of a physically larger size. Since the stepwise bending fatigue test has been previously validated for several iterations of specimen geometries, there is great potential for intricate internal features inside plate-shaped specimens. This would increase the cost of experimentation, but the value of the information to be gained has high potential.

Chapter 8: Appendices

Appendix 8.1: Fractography Images

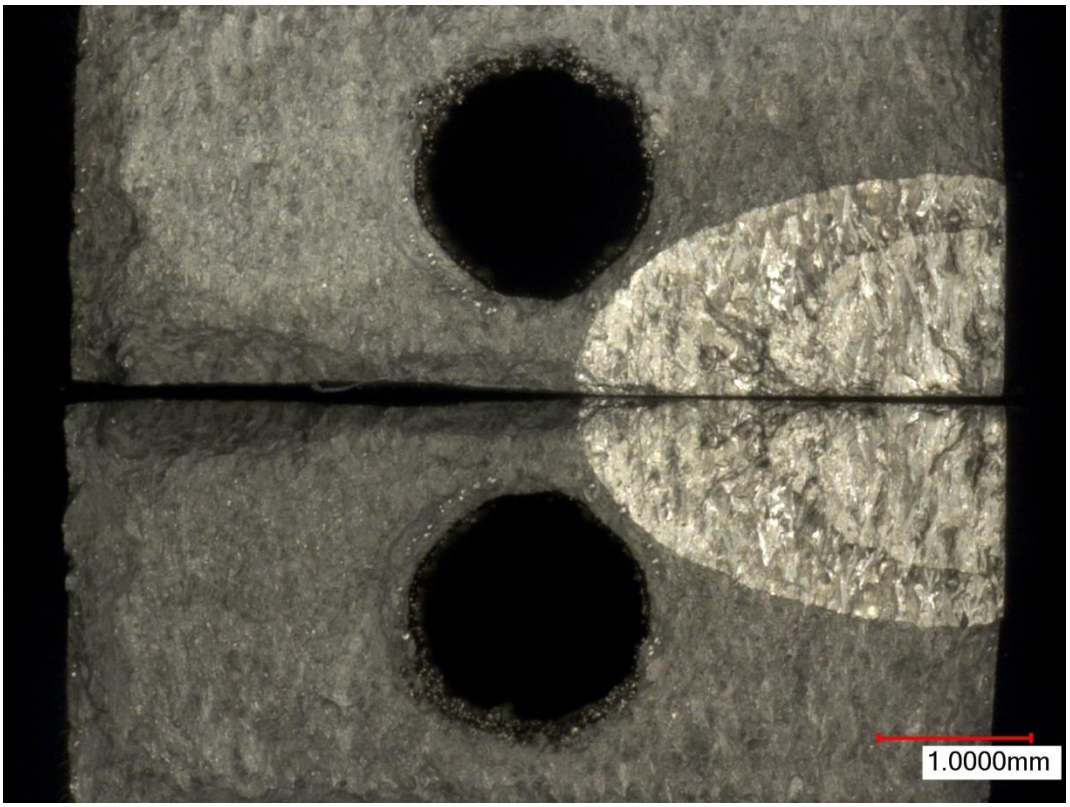

Figure 37: Specimen A1 fracture surface (150,000 cycles : 72.21 ksi / 497.9 MPa)

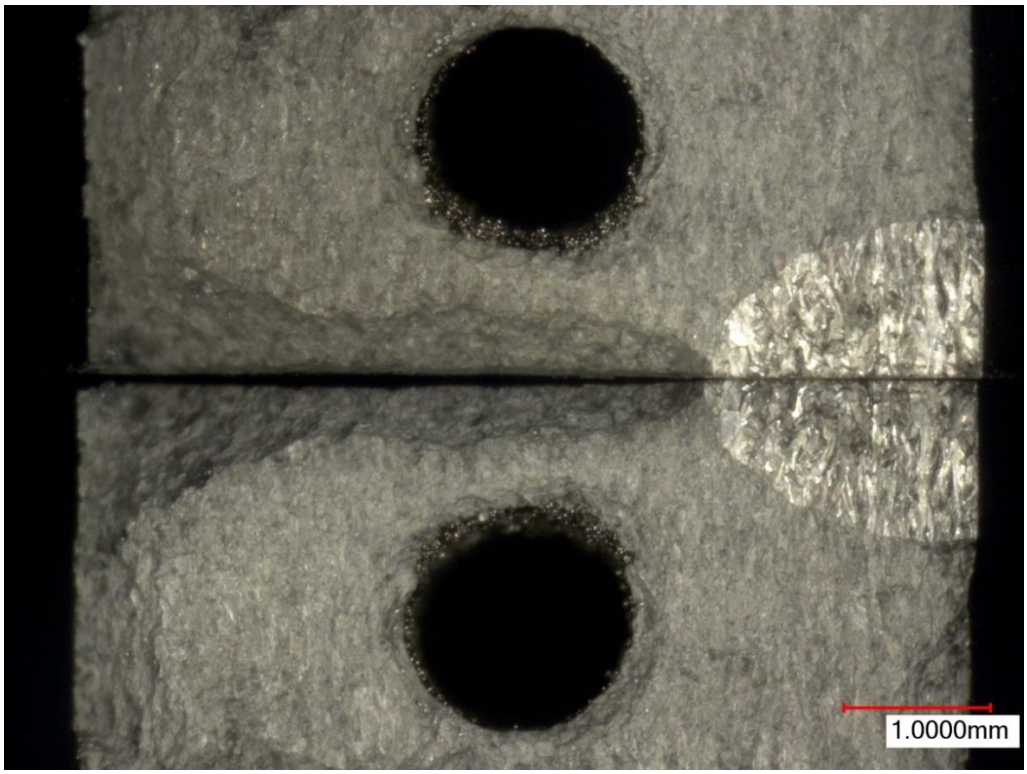

Figure 38: Specimen A2 fracture surface (500,000 cycles : 64.14 ksi / 442.3 MPa)

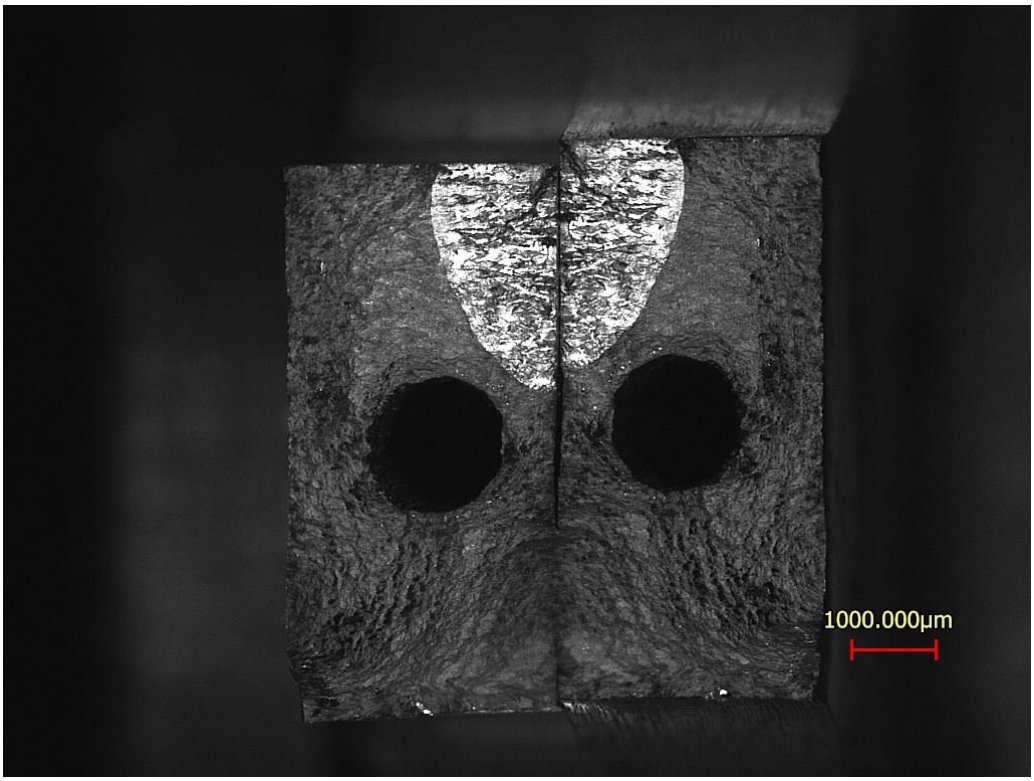

Figure 39: Specimen A3 fracture surface (10,000,000 cycles : 50.09 ksi / 345.3 MPa)

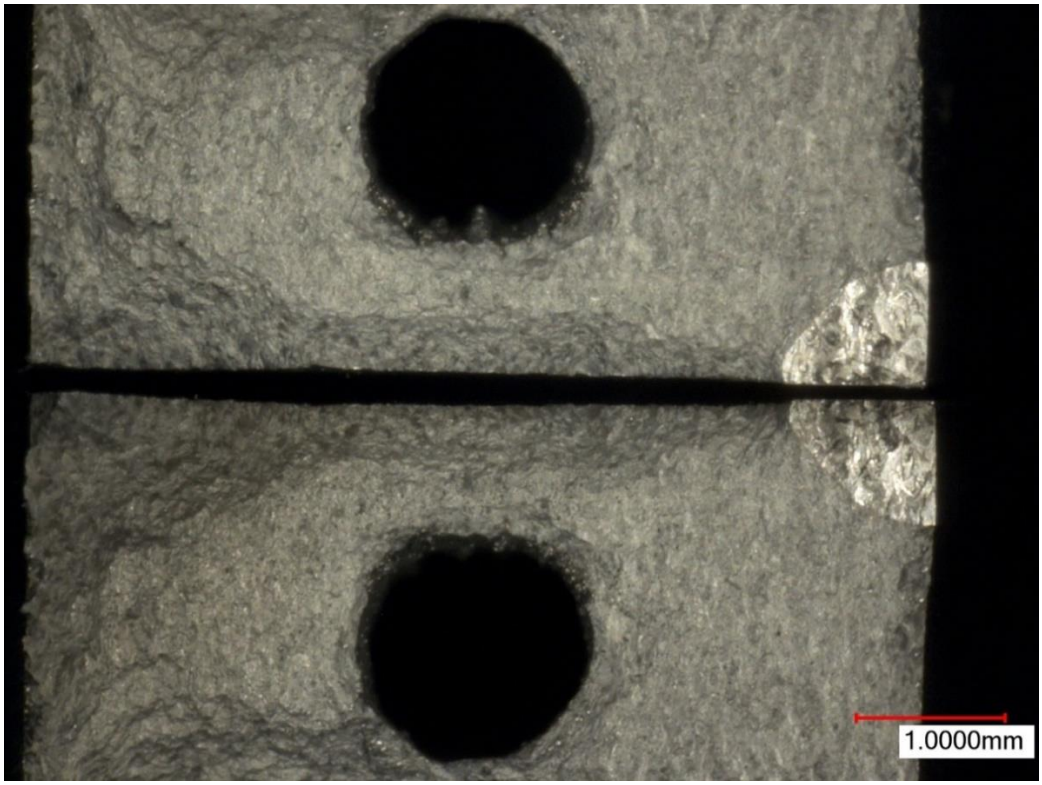

Figure 40: Specimen B1 fracture surface (500,000 cycles : 65.80 ksi / 453.7 MPa)

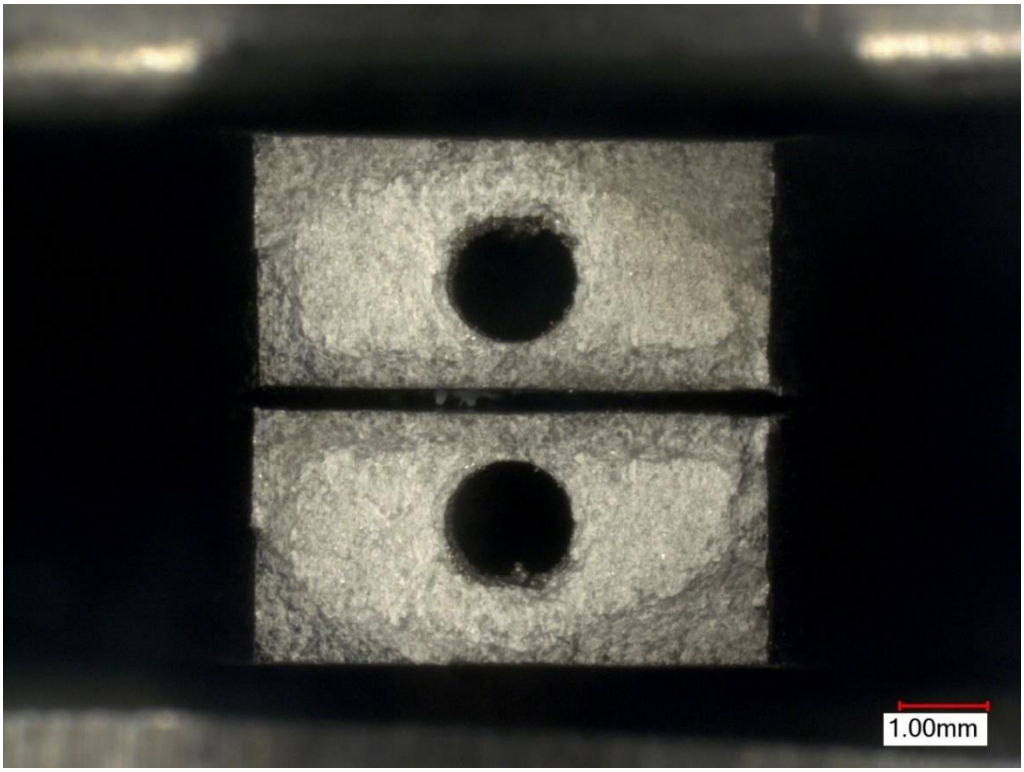

Figure 41: Specimen B2 fracture surface (1,000,000 cycles : 65.18 ksi / 449.4 MPa)

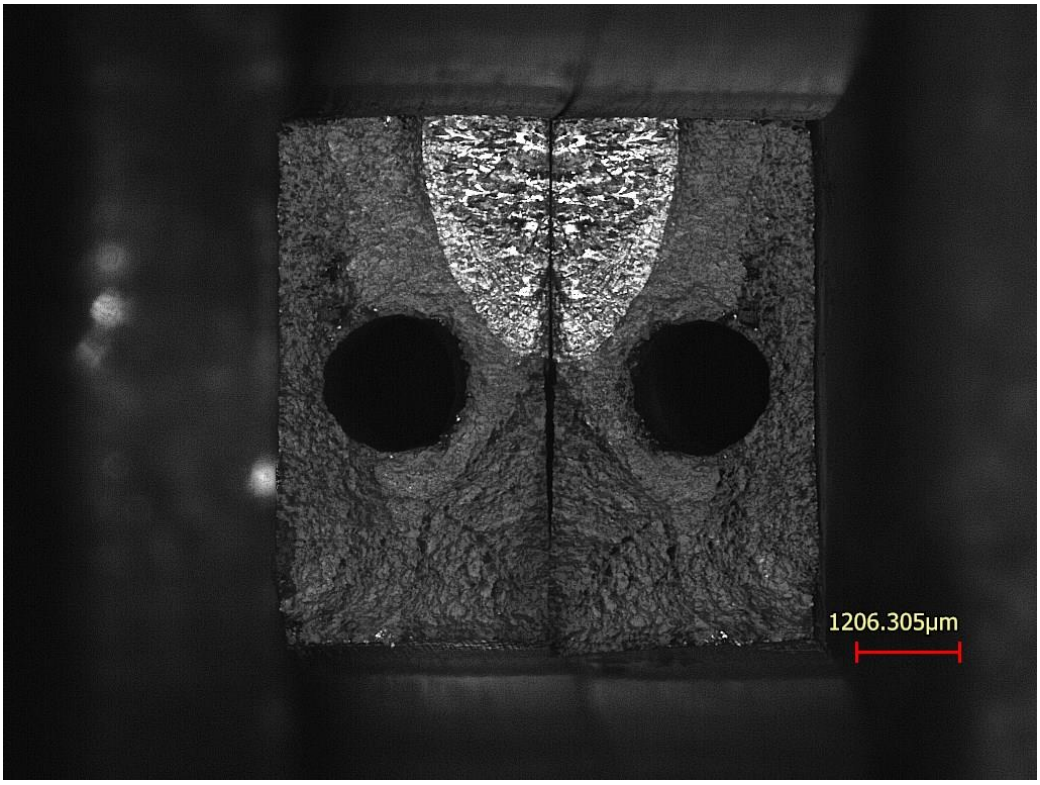

Figure 42: Specimen B3 fracture surface (2,000,000 cycles : 64.87 ksi / 447.3 MPa)

Figure 43: Specimen C1 fracture surface (1,000,000 cycles : 61.33 ksi / 422.8 MPa)

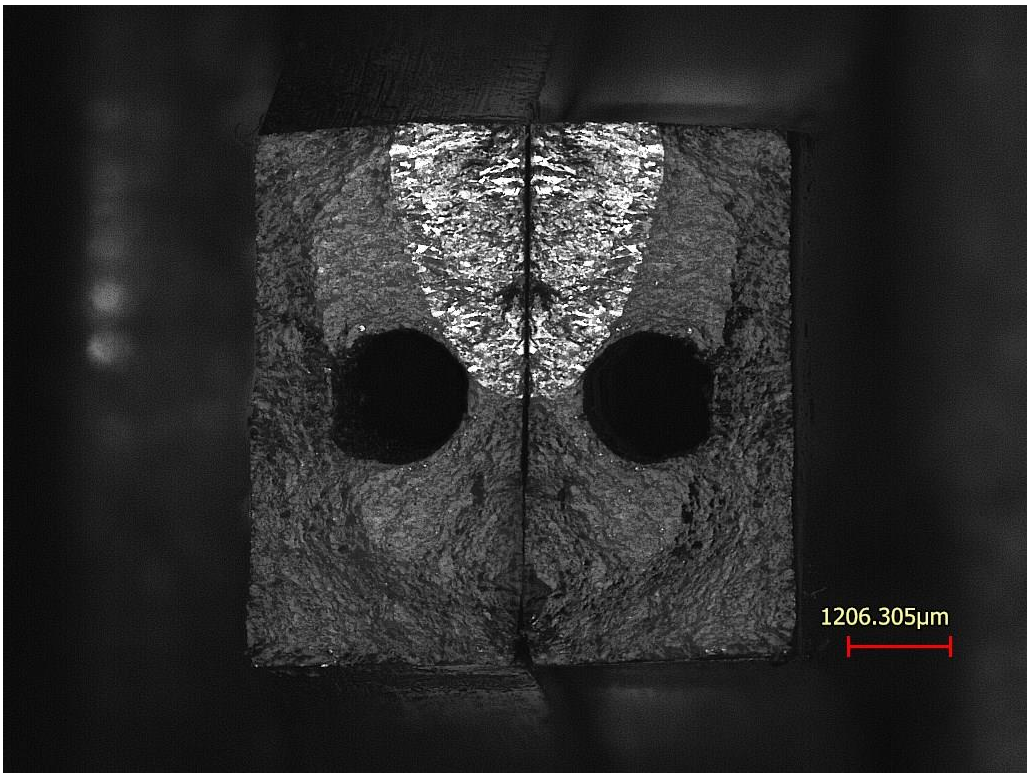

Figure 44: Specimen C2 fracture surface (3,000,000 cycles : 67.49 ksi / 465.3 MPa)

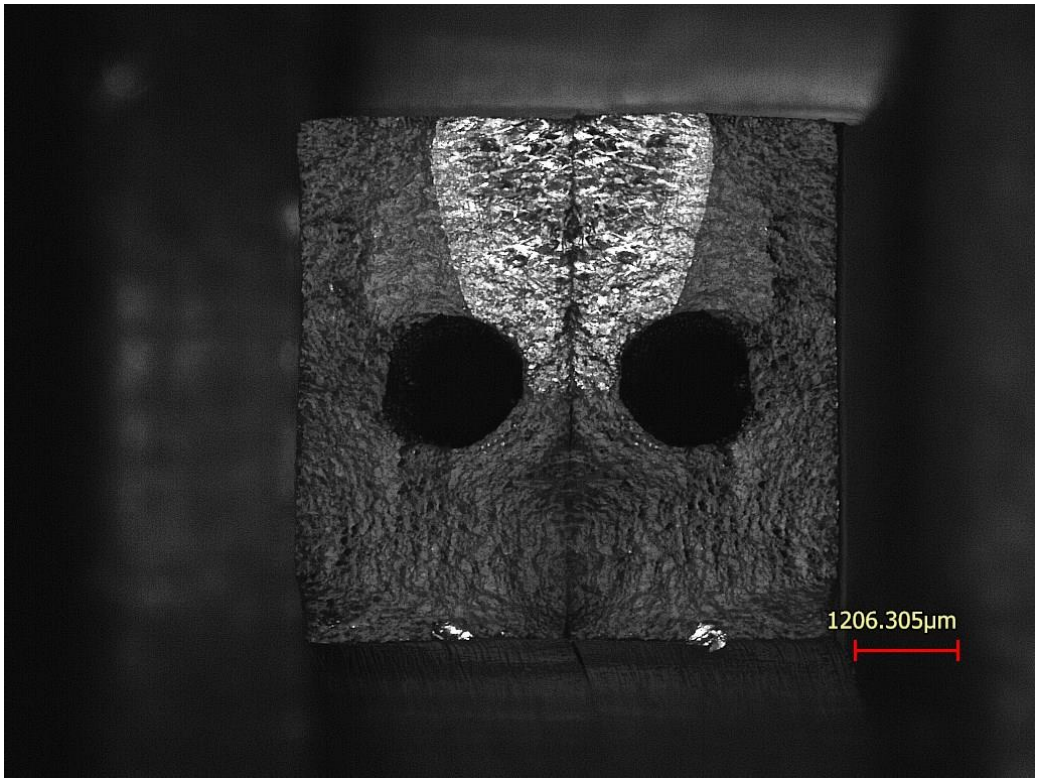

Figure 45: Specimen C3 fracture surface (700,000 cycles : 63.62 ksi / 438.6 MPa)

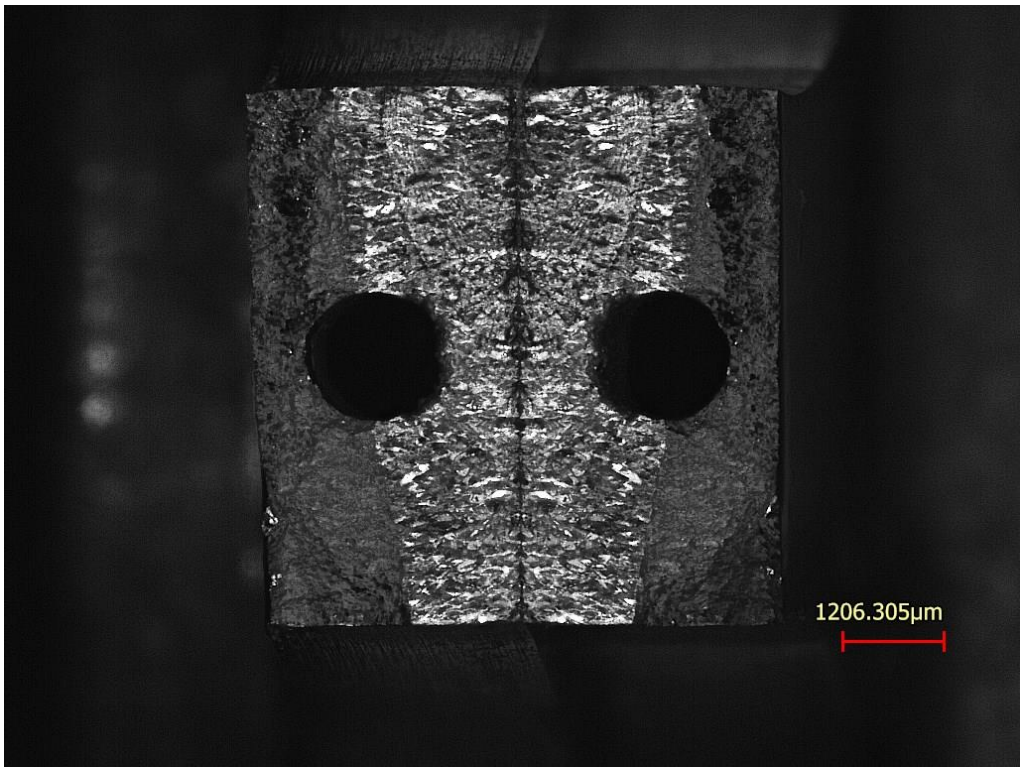

Figure 46: Specimen D1 fracture surface (10,000,000 cycles : 59.70 ksi / 411.6 MPa)

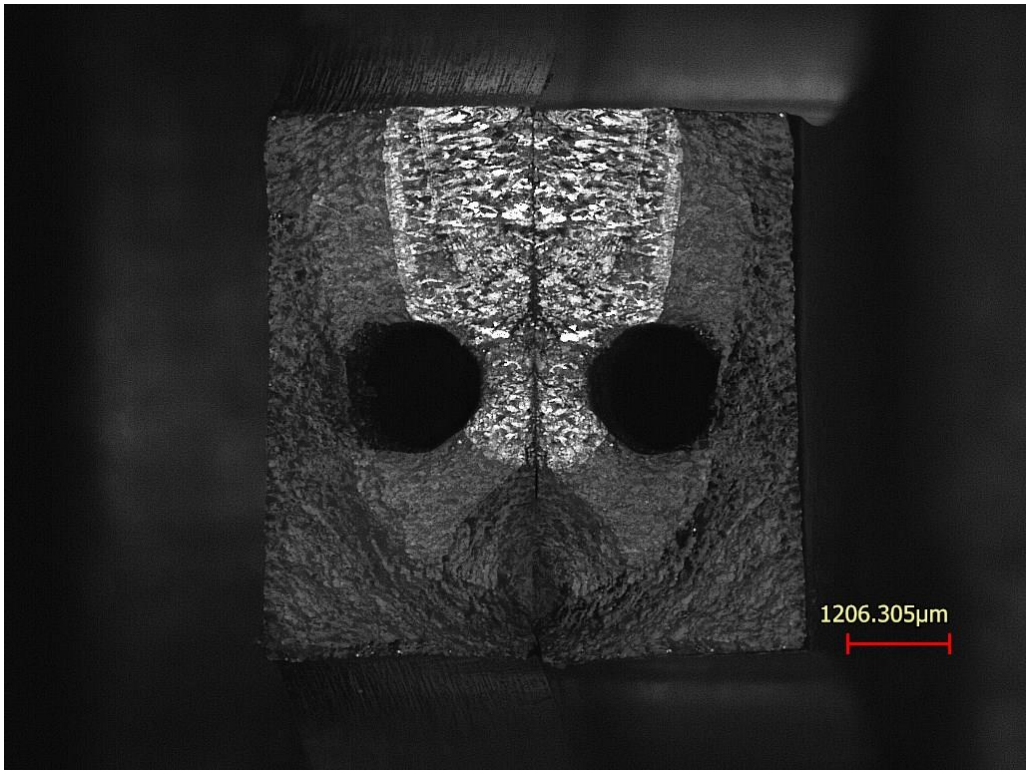

Figure 47: Specimen D2 fracture surface (3,000,000 cycles : 55.51 ksi / 382.7 MPa)

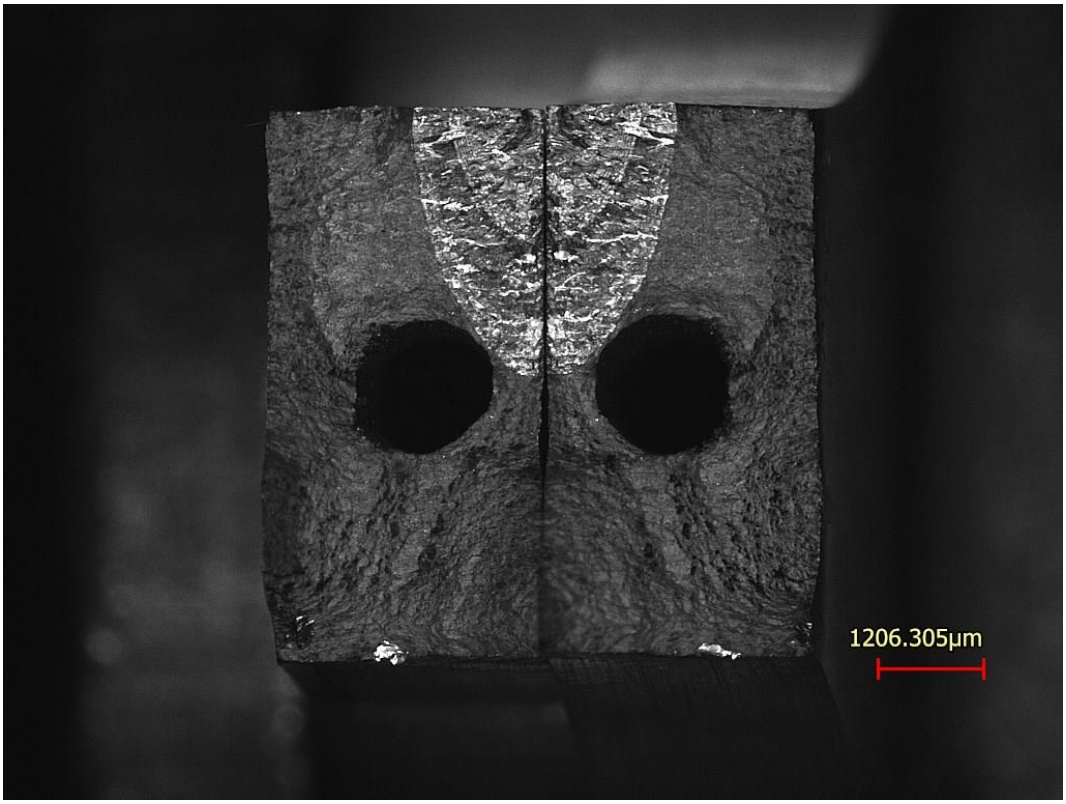

Figure 48: Specimen D3 fracture surface (300,000 cycles : 73.27 ksi / 505.2 MPa)

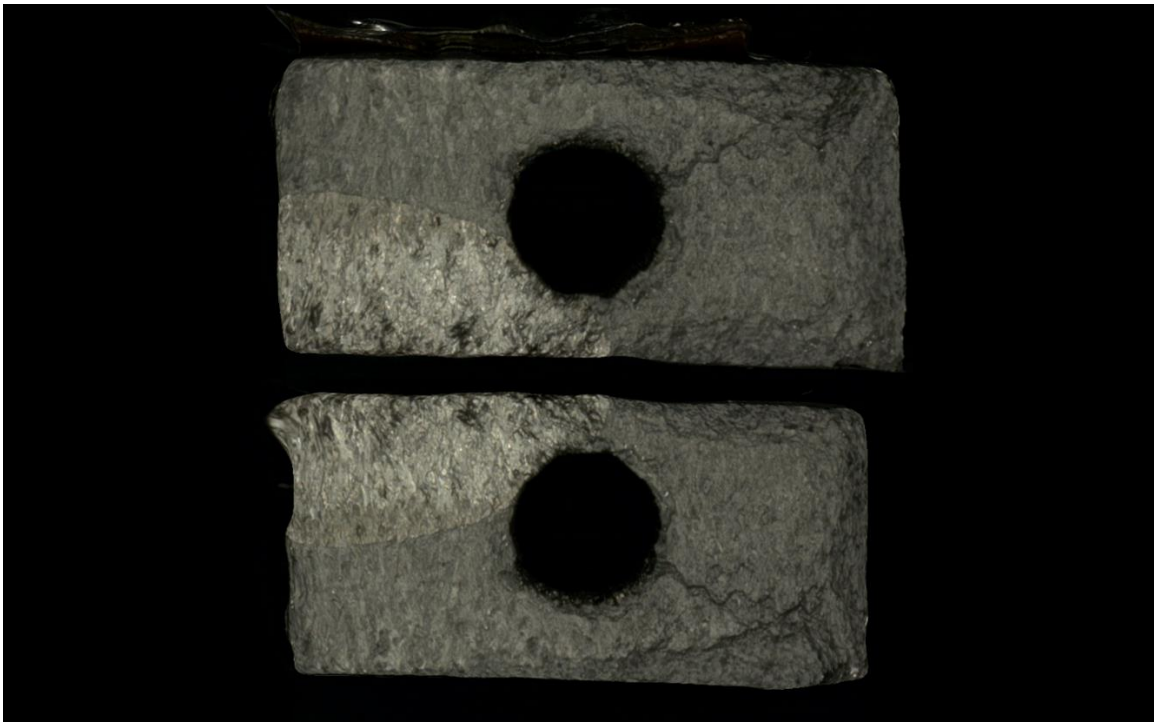

Figure 49: Specimen E1 fracture surface (150,000 cycles : 78.43 ksi / 540.8 MPa)

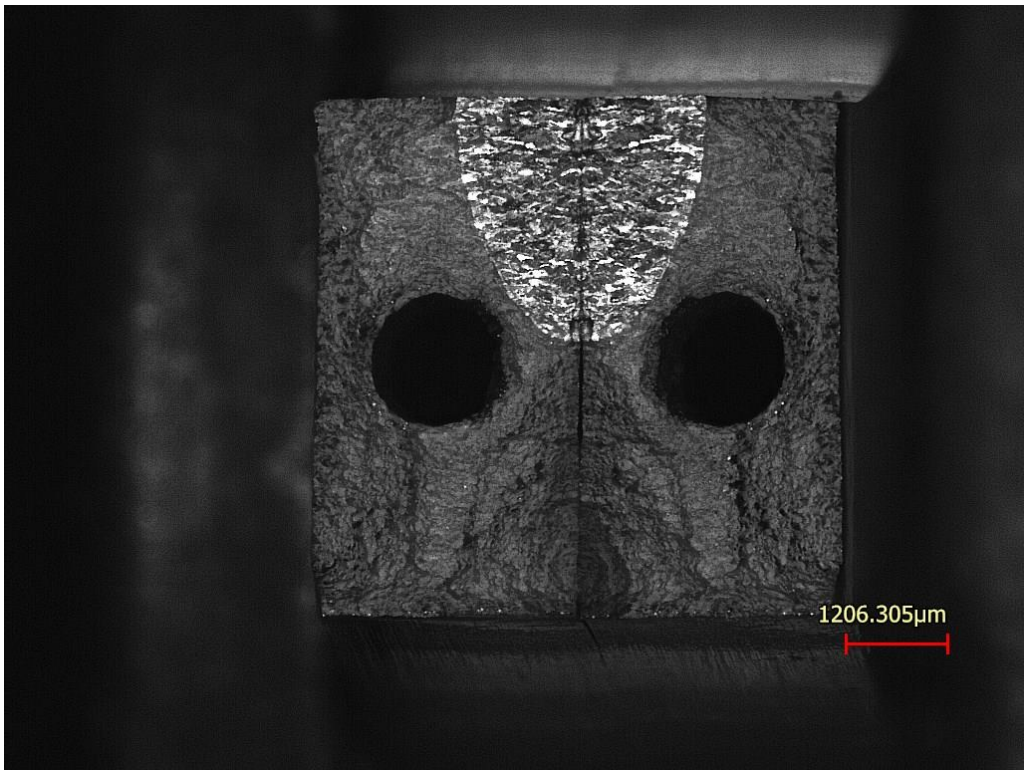

Figure 50: Specimen E2 fracture surface (3,000,000 cycles : 56.73 ksi / 391.2 MPa)

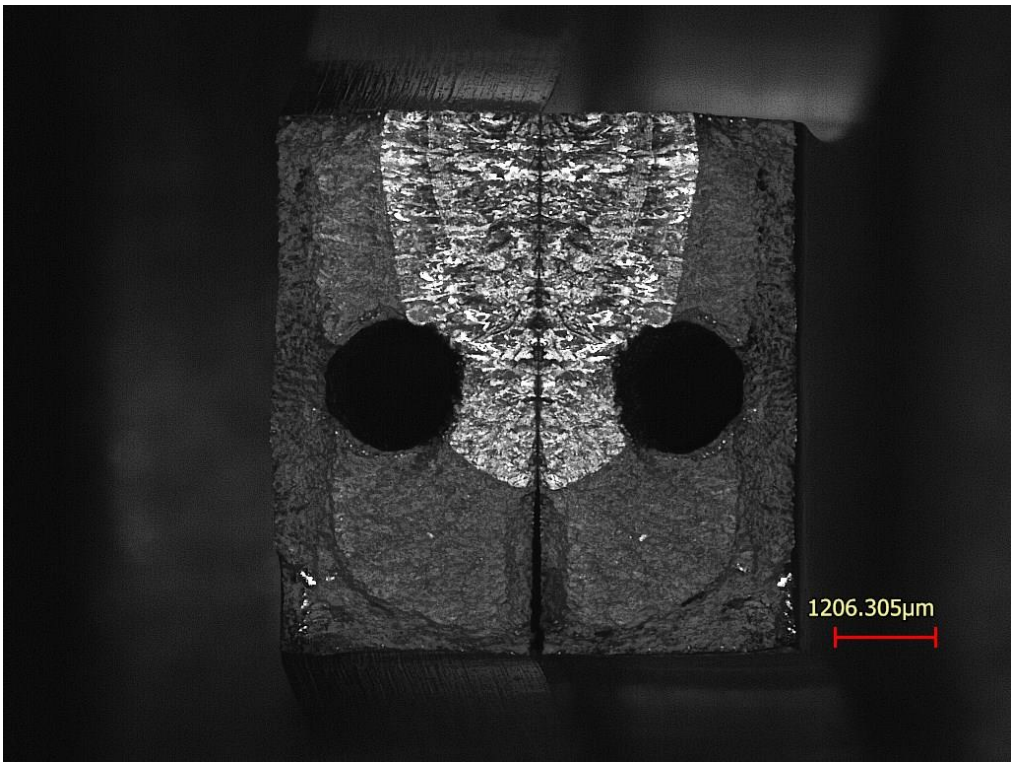

Figure 51: Specimen E3 fracture surface (6,000,000 cycles : 61.76 ksi / 425.8 MPa)

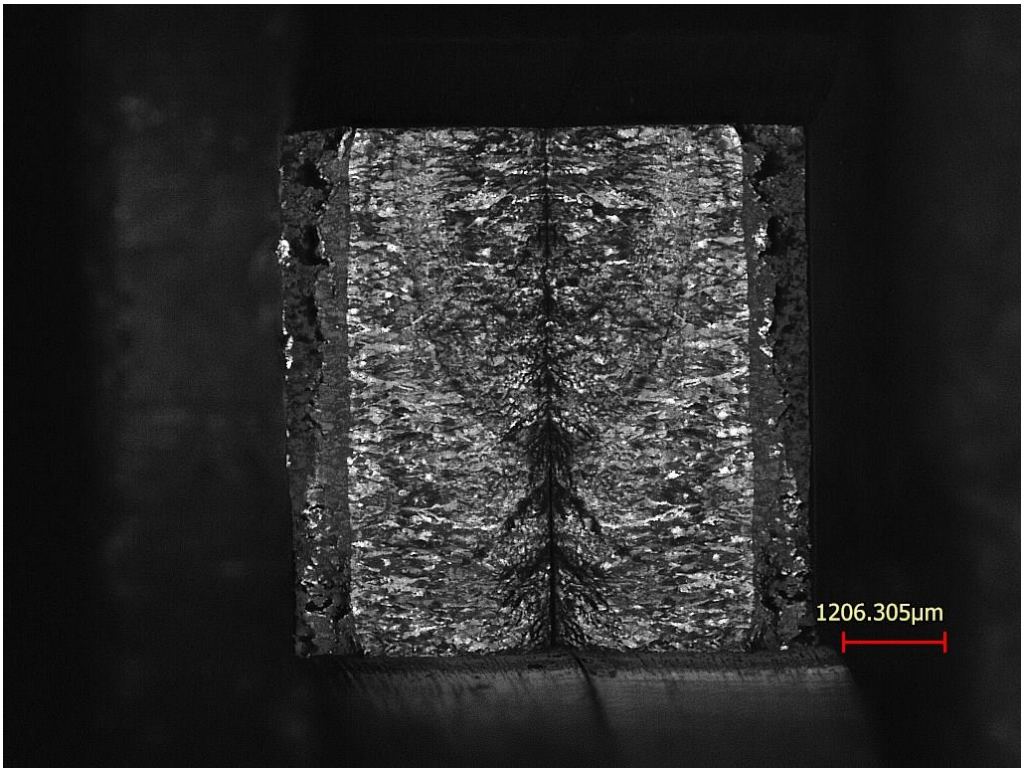

Figure 52: Specimen AS fracture surface (3,000,000 cycles : 55.35 ksi / 381.6 MPa)

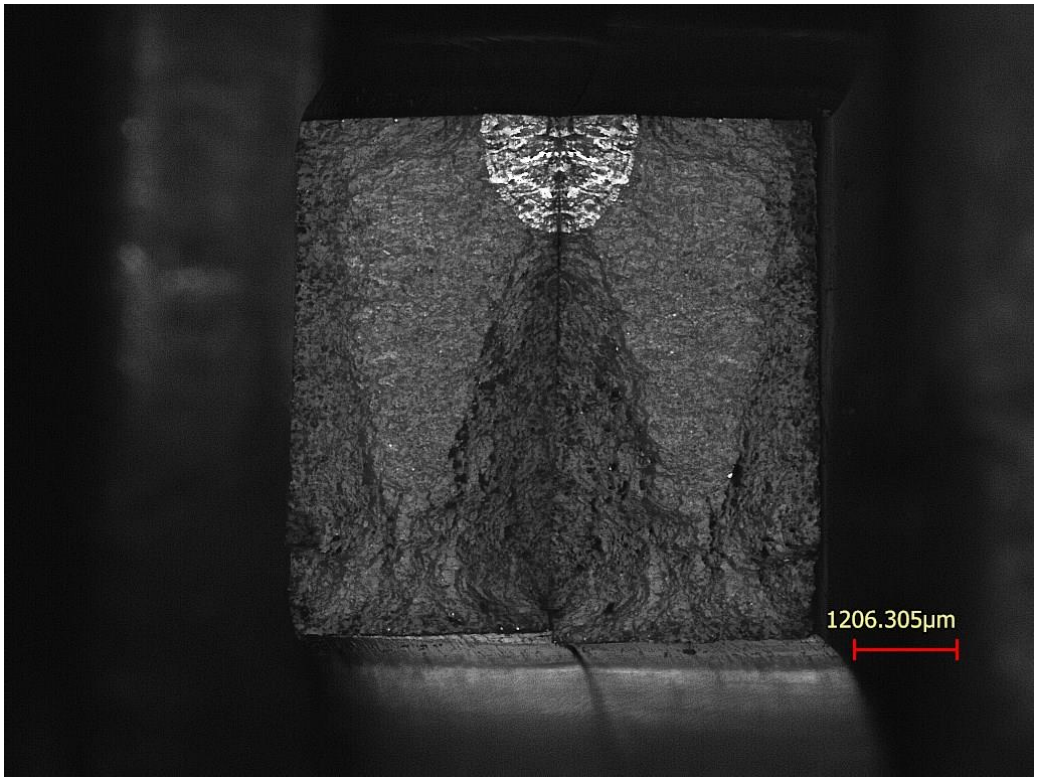

Figure 53: Specimen BS fracture surface (150,000 cycles : 80.43 ksi / 554.6 MPa)

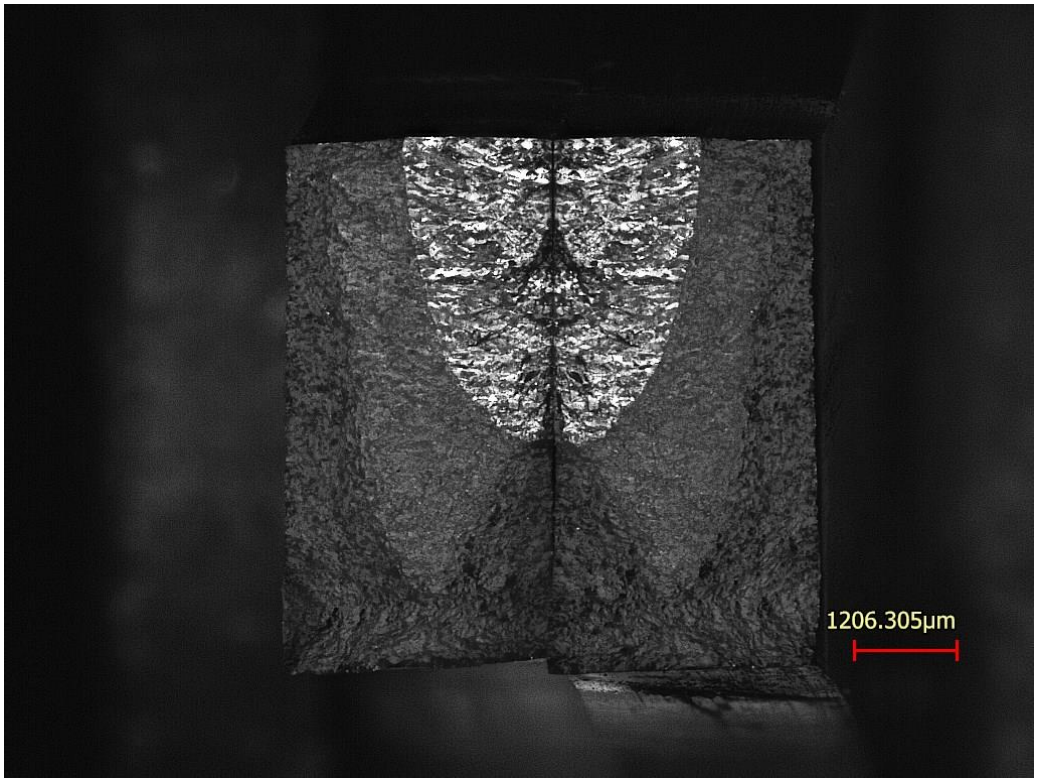

Figure 54: Specimen CS fracture surface (500,000 cycles : 67.06 ksi / 462.3 MPa)

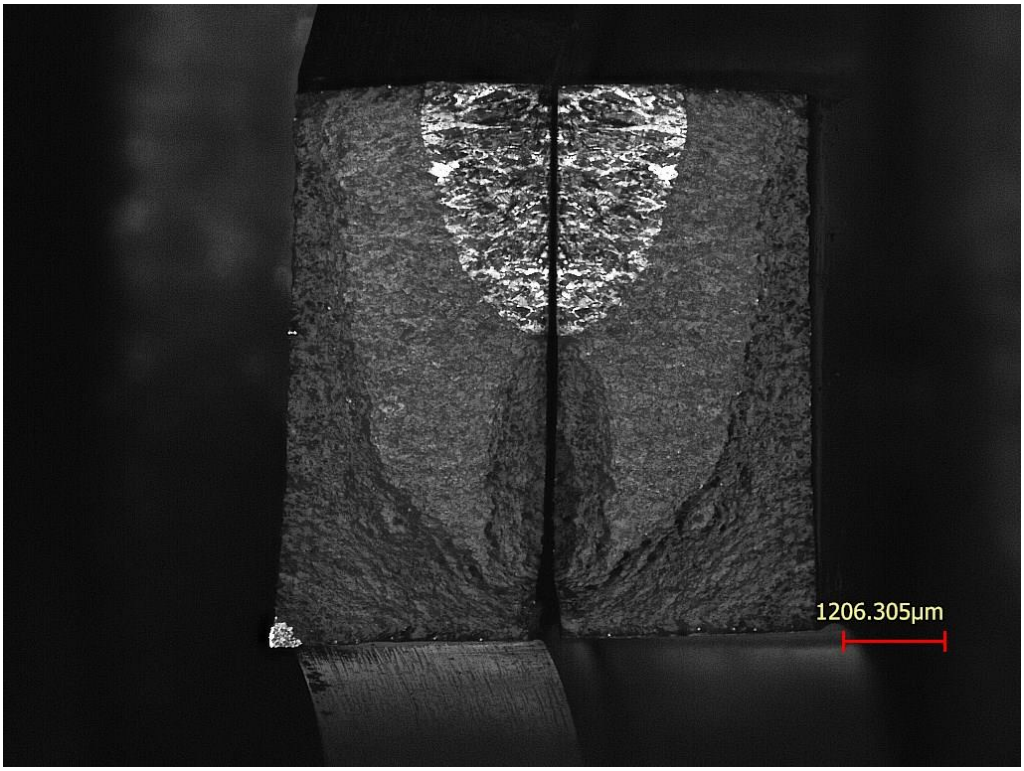

Figure 55: Specimen DS fracture surface (1,000,000 cycles : 67.54 ksi / 465.7 MPa)

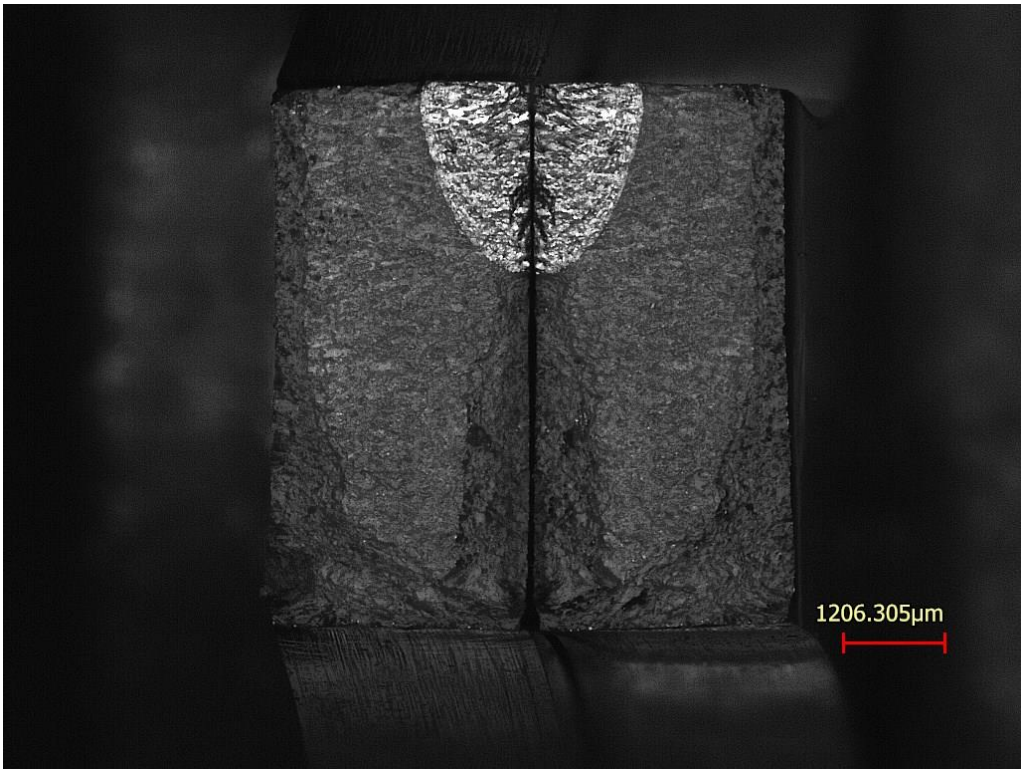

Figure 56: Specimen ES fracture surface (10,000,000 cycles : 71.01 ksi / 489.6 MPa)

Appendix 8.2: Vibration Bending Control Plots

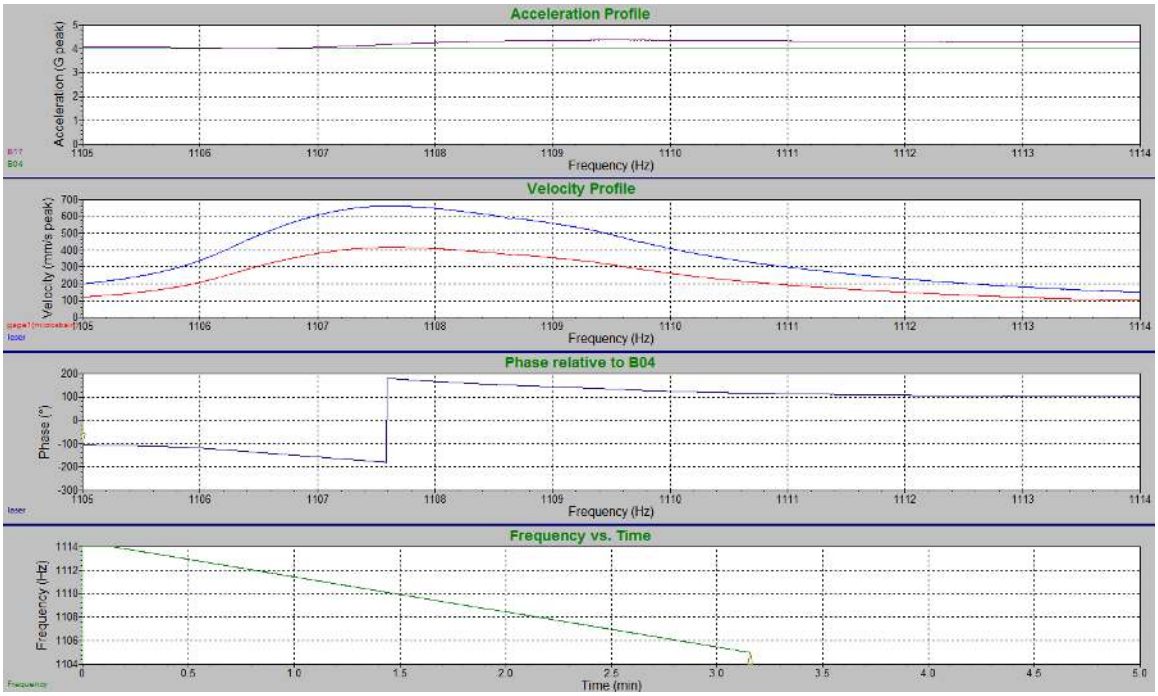

Figure 57: Specimen A1 4 g strain-velocity calibration sweep

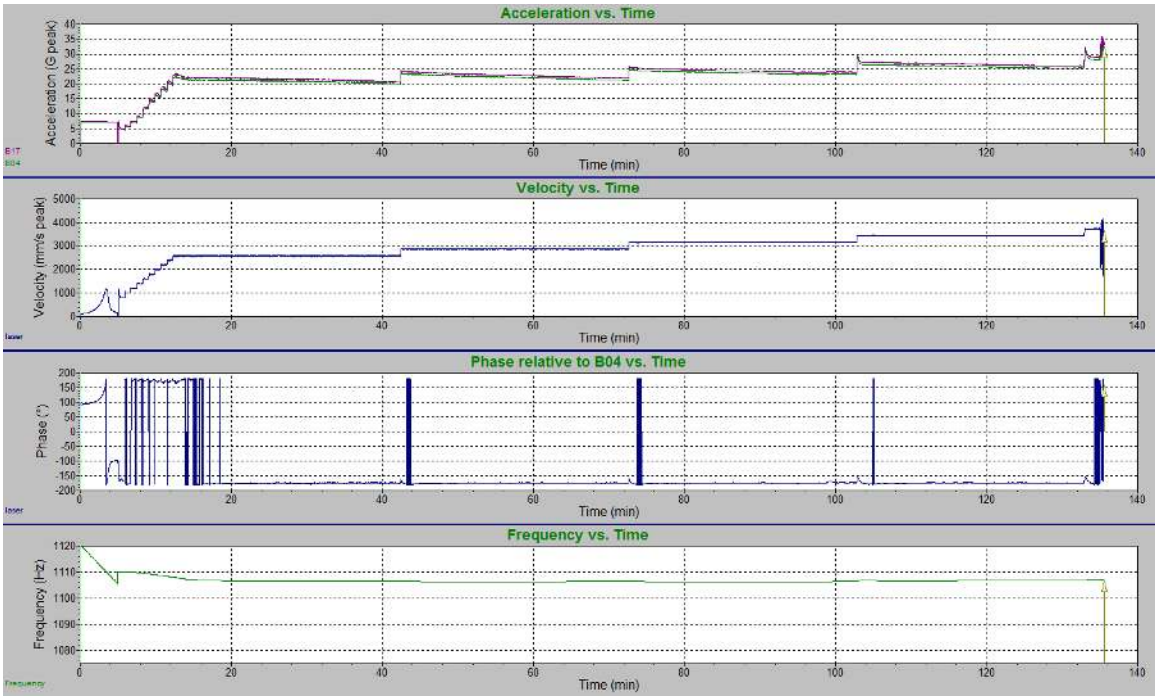

Figure 58: Specimen B3 fatigue test

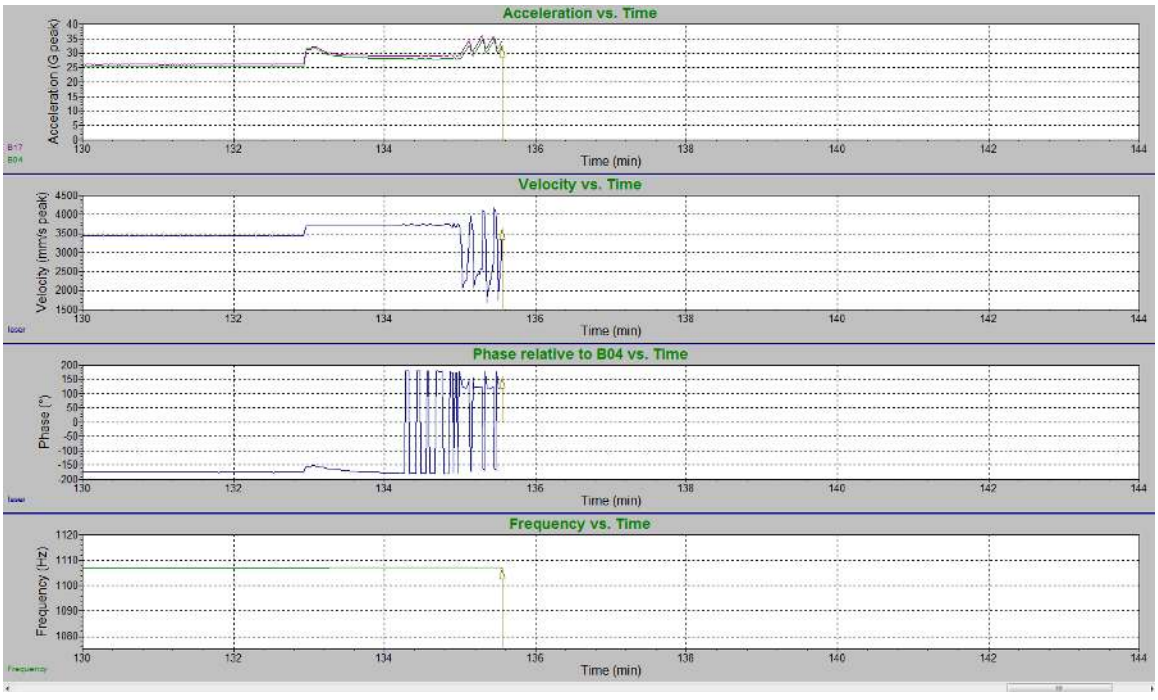

Figure 59: Specimen B3 fatigue failure

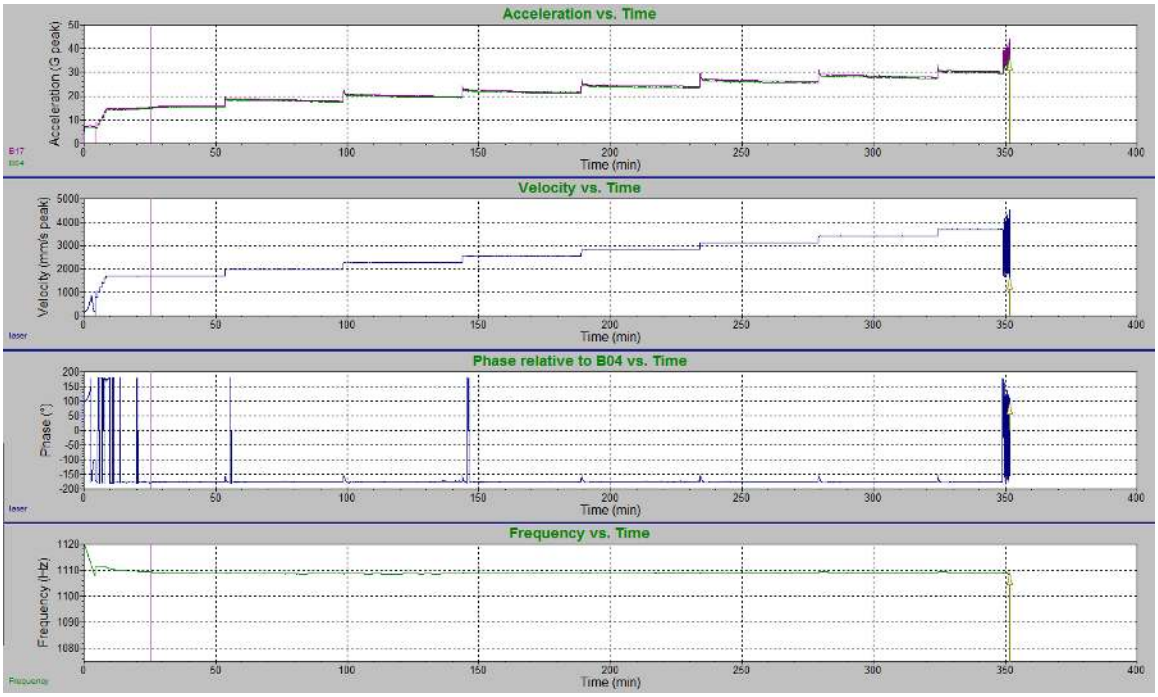

Figure 60: Specimen C2 fatigue test

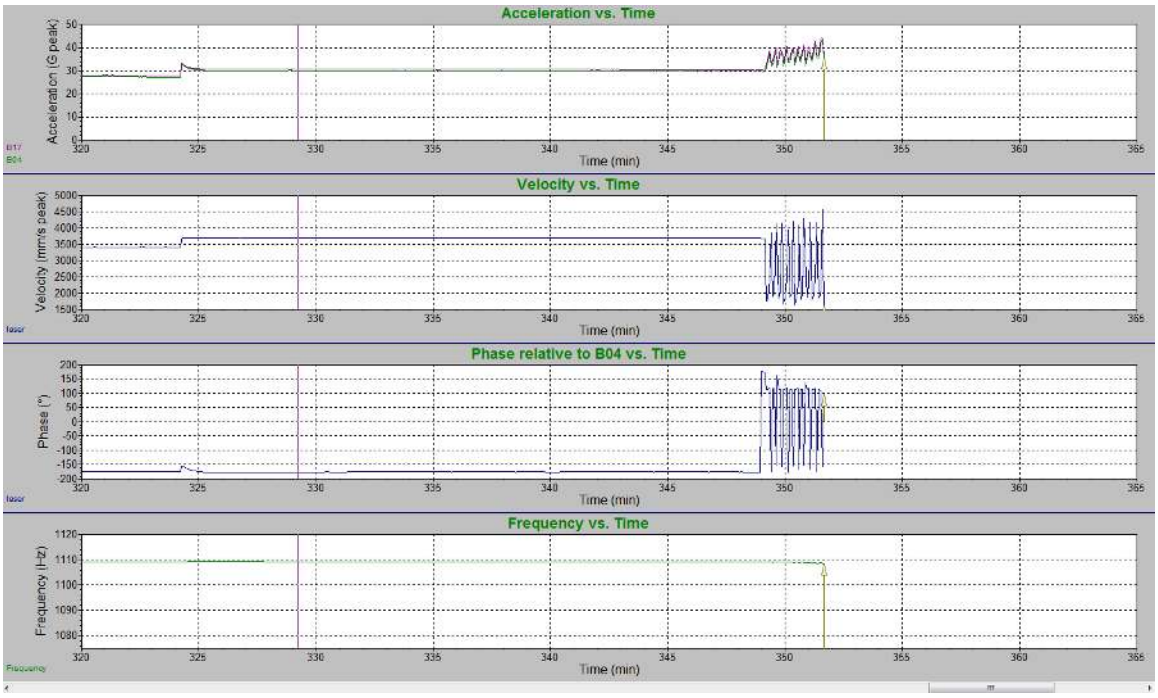

Figure 61: Specimen C2 fatigue failure

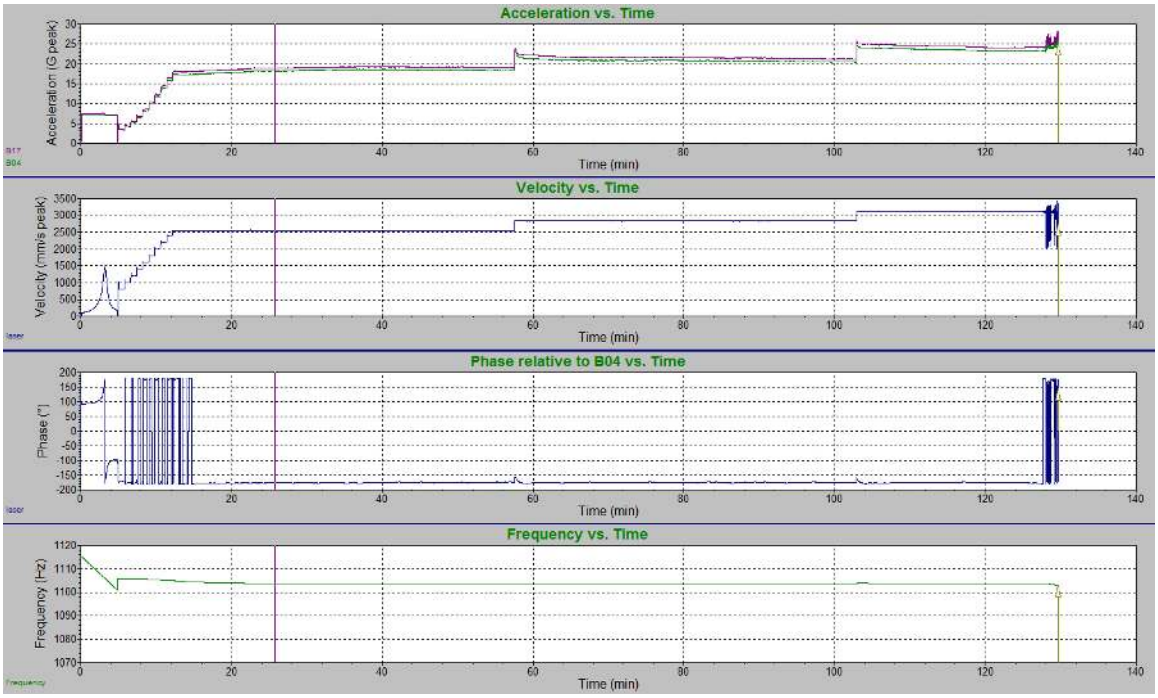

Figure 62: Specimen E2 fatigue test

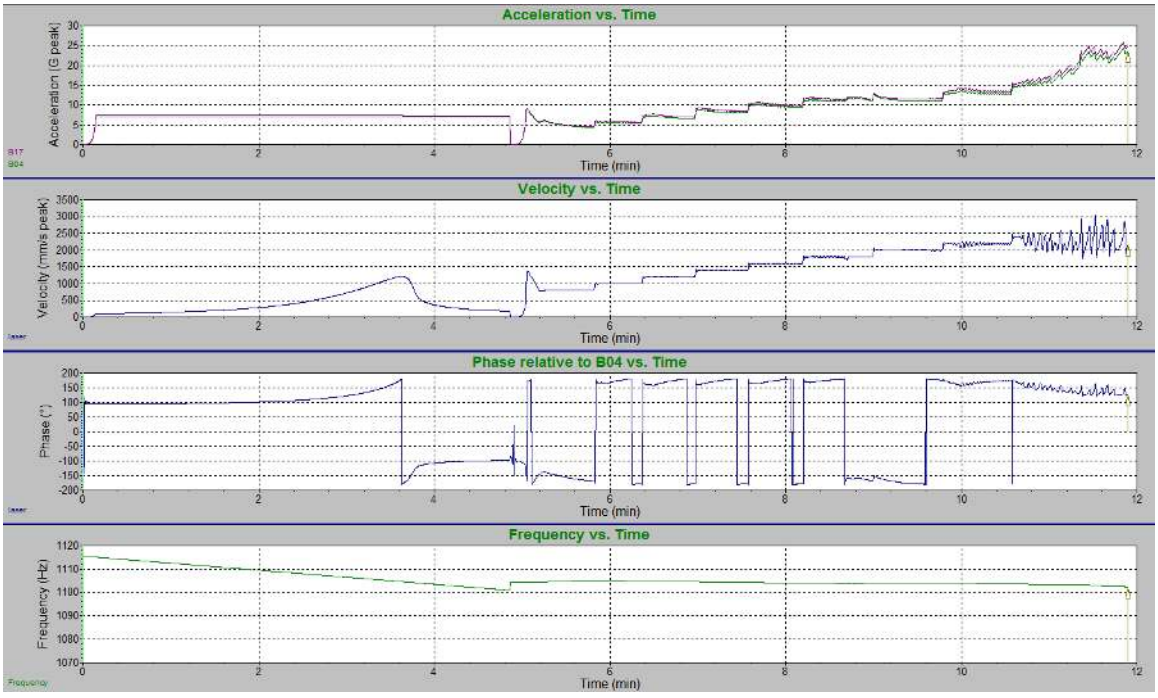

Figure 63: Specimen E2 failure check

Chapter 9: Bibliography

[1] J. Fielding, A. Davis, B. Bouffard, M. Kinsella, T. Delgado, J. Wilczynski, K. Marchese and I. Wing, "Department of Defense additive manufacturing roadmap," US Department of Defense, Washington, DC, 2016.

[2] N. T. Aboulkhair, N. M. Everitt, I. Ashcroft and C. Tuck, "Reducing porosity in AlSi10Mg parts processed by selective laser melting," *Additive Manufacturing,* Vols. 1-4, pp. 77-86, 2014.

[3] R. Cunningham, S. P. Narra, T. Ozturk, J. Beuth and A. D. Rollett, "Evaluating the Effect of Processing Parameters on Porosity in Electron Beam Melted Ti-6Al-4V via Synchrotron X-ray Microtomography," *The Journal of The Minerals, Metals & Materials Society,* vol. 68, pp. 765-771, 2016.

[4] J. C. Fox, S. P. Moylan and B. M. Lane, "Effect of process parameters on the surface roughness of overhanging structures in laser powder bed fusion additive manufacturing," in *CIRP Conference on Surface Integrity*, Charlotte, NC, 2016.

[5] G. Strano, L. Hao, R. M. Everson and K. Evans, "Surface roughness analysis, modelling and prediction in selective laser melting," *Journal of Materials Processing Technology,* vol. 213, no. 4, pp. 589-597, 2013.

[6] G. N. Levy, R. Schindel and J. P. Kruth, "Rapid Manufacturing and Rapid Tooling with Layer Manufacturing (LM) Technologies, State of the Art and Future Perspectives," *CIRP Annals,* vol. 52, no. 2, pp. 589-609, 2003.

[7] Wohlers, "Wohlers Report 2014: Additive Manufacturing," 2014.

[8] D. Thomas, "Costs, benefits, and adoption of additive manufacturing: a supply chain perspective," *International Journal of Advanced Manufacturing Technology,* vol. 85, no. 5-8, p. 1857–1876, 2016.

[9] Y. H. Chen, C. T. Ng and Y. Z. Wang, "Generation of an STL File from 3D Measurement Data with User-Controlled Data Reduction," *International Journal of Advanced Manufacturing Technology,* vol. 15, pp. 127-131, 1999.

[10] M. Yakout, A. Cadamuro, M. A. Elbestawi and S. C. Veldhuis, "The selection of process parameters in additive manufacturing for aerospace alloys," *International Journal of Advanced Manufacturing Technology,* vol. 92, p. 2081–2098, 2017.

[11] ASTM International, *ASTM F2792-12a, Standard Terminology for Additive Manufacturing Technologies, (Withdrawn 2015),* West Conshohocken, PA, 2012.

[12] Hybrid Manufacturing Technologies, "7 Families of Additive Manufacturing," 2018. [Online]. Available: http://www.hybridmanutech.com/resources.html. [Accessed 29 February 2020].

[13] T. Hafkamp, G. van Baars, B. de Jager and P. Etman, "A feasibility study on process monitoring and control in vat photopolymerization of ceramics," *Mechatronics,* vol. 56, pp. 220-241, 2018.

[14] I. Gibson, D. Rosen and B. Stucker, Additive Manufacturing Technologies: 3D Printing, Rapid Prototyping, and Direct Digital Manufacturing, New York: Springer, 2015.

[15] S. Meteyer, X. Xu, N. Perry and Y. F. Zhao, "Energy and Material Flow Analysis of Binder-jetting Additive Manufacturing Processes," *Procedia CIRP,* vol. 15, pp. 19-25, 2014.

[16] Y. L. Yap, C. Wang, S. L. Sing, V. Dikshit, W. Y. Yeong and J. Wei, "Material jetting additive manufacturing: An experimental study using designed metrological benchmarks," *Precision Engineering,* vol. 50, pp. 275-285, 2017.

[17] S. Park and D. W. Rosen, "Quantifying effects of material extrusion additive manufacturing process on mechanical properties of lattice structures using as-fabricated voxel modeling," *Additive Manufacturing,* vol. 12B, pp. 265-273, 2016.

[18] A. Saboori, D. Gallo, S. Biamino, P. Fino and M. Lombardi, "An Overview of Additive Manufacturing of Titanium Components by Directed Energy Deposition: Microstructure and Mechanical Properties," *Applied Sciences,* vol. 7, no. 9, p. 883, 2017.

[19] B. Ferrar, L. Mullen, E. Jones, R. Stamp and C. J. Sutcliffe, "Gas flow effects on selective laser melting (SLM) manufacturing performance," *Journal of Materials Processing Technology,* vol. 212, no. 2, pp. 355-364, 2012.

[20] Inco Alloys International, Inconel Alloy 718, 4th Edition, 1985.

[21] M. Rahman, W. K. H. Seah and T. T. Teo, "The Machinability of Inconel 718," *Journal of Materials Processing Technology,* vol. 63, pp. 199-204, 1997.

[22] Special Metals Corporation, "INCONEL alloy 718," 7 September 2007. [Online]. Available: https://www.specialmetals.com/assets/smc/documents/inconel_alloy_718.pdf. [Accessed 2 March 2020].

[23] United Performance Metals, "Nickel Alloy 718," [Online]. Available: https://www.upmet.com/sites/default/files/datasheets/718.pdf. [Accessed 2 March 2020].

[24] D. H. Smith, J. Bicknell, L. Jorgensen, B. M. Patterson, N. L. Cordes, I. Tsukrov and M. Knezevic, "Microstructure and mechanical behavior of direct metal laser sintered Inconel alloy 718," *Materials Characterization,* vol. 113, pp. 1-9, 2016.

[25] K. Kobayashi, K. Yamaguchi, M. Hayakawa and M. Kimura, "High-temperature fatigue properties of austenitic superalloys 718, A286 and 304L," *International Journal of Fatigue,* vol. 30, no. 10-11, pp. 1978-1984, 2008.

[26] Y. Ono, T. Yuri, H. Sumiyoshi, E. Takeuchi, S. Matsuoka and T. Ogata, "High-Cycle Fatigue Properties at Cryogenic Temperatures in INCONEL 718 Nickel-based Superalloy," *Materials Transactions,* vol. 45, no. 2, pp. 342-345, 2004.

[27] J. Gockel, L. Sheridan, B. Koerper and B. Whip, "The influence of additive manufacturing processing parameters on surface roughness and fatigue life," *International Journal of Fatigue,* vol. 124, pp. 380-388, 2019.

[28] W. Eidt, E. P. Tatman, J. McCarther, J. Kastner, S. Gunther and J. Gockel, "Surface roughness characterization in laser powder bed fusion additive manufacturing," in *Solid Freeform Fabrication Symposium*, Austin, TX, 2019.

[29] J. Delgado, J. Ciurana and C. A. Rodriguez, "Influence of process parameters on part quality and mechanical properties for DMLS and SLM with iron-based materials," *The International Journal of Advanced Manufacturing Technology,* vol. 60, pp. 601-610, 2012.

[30] F. Calignano, D. Manfredi, E. P. Ambrosio, L. Iuliano and P. Fino, "Influence of process parameters on surface roughness of aluminum parts produced by DMLS," *International Journal of Advanced Manufacturing Technology,* vol. 67, p. 2743–2751, 2013.

[31] E. P. D. Tatman, "The Characterization and Fatigue Life Impact from Surface Roughness on Structurally Relevant Features Produced Using Additive Manufacturing," Wright State University, 2019.

[32] H. Chen, D. Gu, J. Xiong and M. Xia, "Improving additive manufacturing processability of hard-to-process overhanging structure by selective laser melting," *Journal of Materials Processing Technology,* vol. 250, pp. 99-108, 2017.

[33] D. Greitemeier, C. Dalle Donne, F. Syassen, J. Eufinger and T. Melz, "Effect of surface roughness on fatigue performance of additive manufactured Ti–6Al–4V," *Materials Science and Technology,* vol. 32, no. 7, pp. 529-634, 2016.

[34] H. Masuo, Y. Tanaka, S. Morokoshi, H. Yagura, T. Uchida, Y. Yamamoto and Y. Murakami, "Influence of defects, surface roughness and HIP on the fatigue strength of Ti-6Al-4V manufactured by additive manufacturing," *International Journal of Fatigue,* vol. 117, pp. 163-179, 2018.

[35] ISO 25178-2, *Geometrical product specifications (GPS)- surface texture: areal- part 2: terms, definitions and surface texture,* 2012.

[36] B. Whip, L. Sheridan and J. Gockel, "The effect of primary processing parameters on surface roughness in laser powder bed additive manufacturing," *The International Journal of Advanced Manufacturing Technology,* vol. 103, pp. 4411-4422, 2019.

[37] ISO 13565-1, *Geometrical Product Specifications– Surface texture: Profile method; Surfaces having stratified functional properties– Part 1: Filterting and general measurement conditions,* 1996.

[38] D. Hoey and D. Taylor, "Quantitative analysis of the effect of porosity on the fatigue strength of bone cement," *Acta Biomaterialia,* vol. 5, no. 2, pp. 719-726, 2009.

[39] S. A. Yavari, J. van der Stok, Y. C. Chai, R. Wauthle, Z. T. Birgani, P. Habibovic, M. Mulier, J. Schrooten, H. Weinans and A. A. Zadpoor, "Bone regeneration performance of surface-treated porous titanium," *Biomaterials,* vol. 35, no. 24, pp. 6172-6181, 2014.

[40] J. A. Slotwinski, E. J. Garboczi and K. M. Hebenstreit, "Porosity Measurements and Analysis for Metal Additive Manufacturing Process Control," *Journal of Research of the National Institute of Standards and Technology,* vol. 119, pp. 494-528, 2014.

[41] B. Van Hooreweder, Y. Apers, K. Lietaert and J. P. Kruth, "Improving the fatigue performance of porous metallic biomaterials produced by Selective Laser Melting," *Acta Biomaterialia,* vol. 47, pp. 193-202, 2017.

[42] S. Tammas-Williams, P. J. Withers, I. Todd and P. B. Prangnell, "The Influence of Porosity on Fatigue Crack Initiation in Additively Manufactured Titanium Components," *Scientific Reports,* vol. 7, no. 7308, 2017.

[43] W. E. King, H. D. Barth, V. M. Castillo, G. F. Gallegos, J. W. Gibbs, D. E. Hahn, C. Kamath and A. M. Rubenchik, "Observation of keyhole-mode laser melting in laser powder-bed fusion additive manufacturing," *Journal of Materials Processing Technology,* vol. 214, no. 12, pp. 2915-2925, 2014.

[44] J. Zhang, F. Liou, W. Seufzer and K. Taminger, "A coupled finite element cellular automaton model to predict thermal history and grain morphology of Ti-6Al-4V during direct metal deposition (DMD)," *Additive Manufacturing,* vol. 11, pp. 32-39, 2016.

[45] Z. Wang, T. A. Palmer and A. Beese, "Effect of processing parameters on microstructure and tensile properties of austenitic stainless steel 304L made by directed energy deposition additive manufacturing," *Acta Materialia,* vol. 110, pp. 226-235, 2016.

[46] E. Fitzgerald and W. Everhart, "The Effect of Location on the Structure and Mechanical Properties of Selective Laser Melted 316L Stainless Steel," in *Solid Freeform Fabrication Symposium*, Austin, TX, 2016.

[47] Y. Ma, D. Cuiuri, N. Hoye, H. Li and Z. Pan, "The effect of location on the microstructure and mechanical properties of titanium aluminides produced by additive layer manufacturing

using in-situ alloying and gas tungsten arc welding," *Materials Science and Engineering: A,* vol. 631, pp. 230-240, 2015.

[48] N. Hrabe and T. Quinn, "Effects of processing on microstructure and mechanical properties of a titanium alloy (Ti–6Al–4V) fabricated using electron beam melting (EBM), part 1: Distance from build plate and part size," *Materials Science and Engineering: A,* vol. 573, pp. 264-270, 2013.

[49] L. Costa, R. Vilar, T. Reti and A. M. Deus, "Rapid tooling by laser powder deposition: Process simulation using finite element analysis," *Acta Materialia,* vol. 53, no. 14, pp. 3987-3999, 2005.

[50] J. Gockel, "Integrated Control of Solidification Microstructure and Melt Pool Dimensions in Additive Manufacturing of Ti-6Al-4V," Carnegie Mellon University, Pittsburgh, PA, 2014.

[51] M. H. Farshidianfar, A. Khajepour and A. P. Gerlich, "Effect of real-time cooling rate on microstructure in Laser Additive Manufacturing," *Journal of Materials Processing Technology,* vol. 231, pp. 468-478, 2016.

[52] F. Wang, S. Williams, P. Colegrove and A. A. Antonysamy, "Microstructure and Mechanical Properties of Wire and Arc Additive Manufactured Ti-6Al-4V," *Metallurgical and Materials Transactions A,* vol. 44, pp. 968-977, 2013.

[53] H. Bheda, W. Mondesir, R. Reese and S. Mantha, "Method and a system to optimize printing parameters in additive manufacturing process". United States Patent US10556382B2, 11 February 2020.

[54] R. G. Budynas and J. K. Nisbett, Shigley's Mechanical Engineering Design, 10th Edition, New York: McGraw Hill Education, 2015.

[55] T. J. George, J. Seidt, M. H. H. Shen, T. Nicholas and C. J. Cross, "Development of a novel vibration-based fatigue testing methodology," *International Journal of Fatigue,* vol. 26, pp. 477-486, 2004.

[56] J. Munguia and K. Dalgarno, "Fatigue behaviour of laser sintered Nylon 12 in rotating and reversed bending tests," *Materials Science and Technology,* vol. 31, no. 8, pp. 904-911, 2015.

[57] A. B. Spierings, T. L. Starr and K. Wegener, "Fatigue performance of additive manufactured metallic parts," *Rapid Prototyping Journal,* vol. 19, no. 2, pp. 88-94, 2013.

[58] B. Ellyson, M. Brochu and M. Brochu, "Characterization of bending vibration fatigue of SLM fabricated Ti-6Al-4V," *International Journal of Fatigue,* vol. 99, no. 1, pp. 25-34, 2017.

[59] P. A. Kelly, Solid Mechanics Part I, Auckland, NZ, 2015.

[60] L. Sheridan, O. E. Scott-Emuakpor, T. George and J. E. Gockel, "Relating porosity to fatigue failure in additively manufactured alloy 718," *Materials Science and Engineering: A,* vol. 727, pp. 170-176, 2018.

[61] S. Romano, A. Brückner-Foit, A. Brandão, J. Gumpinger, T. Ghidini and S. Beretta, "Fatigue properties of AlSi10Mg obtained by additive manufacturing: Defect-based modelling and prediction of fatigue strength," *Engineering Fracture Mechanics,* vol. 187, pp. 165-189, 2018.

[62] G. Meneghetti, D. Rigon and C. Gennari, "An analysis of defects influence on axial fatigue strength of maraging steel specimens produced by additive manufacturing," *International Journal of Fatigue,* vol. 118, pp. 54-64, 2019.

[63] K. Tanaka, "Engineering formulae for fatigue strength reduction due to crack-like notches," *International Journal of Fracture,* vol. 22, pp. 39-46, 1983.

[64] D. Taylor, The Theory of Critical Distances: A New Perspective in Fracture Mechanics, Oxford, UK: Elsevier, 2007.

[65] M. M. Shahri and R. Sandström, "Fatigue analysis of friction stir welded aluminium profile using critical distance," *International Journal of Fatigue,* vol. 32, no. 2, pp. 302-309, 2010.

[66] D. Taylor and G. Wang, "The validation of some methods of notch fatigue analysis," *Fatigue & Fracture of Engineering Materials & Structures,* vol. 23, pp. 387-394, 2000.

[67] D. Hoey and D. Taylor, "Fatigue in porous PMMA: The effect of stress concentrations," *International Journal of Fatigue,* vol. 30, pp. 989-995, 2008.

[68] D. Taylor, M. Merlo, R. Pegley and M. P. Cavatorta, "The effect of stress concentrations on the fracture strength of polymethylmethacrylate," *Materials Science & Engineering: A,* vol. 382, pp. 288-294, 2004.

[69] Z. Cheng, R. Liao, W. Lu and D. Wang, "Fatigue notch factors prediction of rough specimen by the theory of critical distance," *International Journal of Fatigue,* vol. 104, pp. 195-205, 2017.

[70] J. C. Sobotka, M. P. Enright and R. C. McClung, "Application of critical distances to fatigue at pores," *Fatigue & Fracture of Engineering Materials & Structures,* vol. 42, pp. 1646-1661, 2019.

[71] O. Vardar, I. Finnie, D. R. Biswas and R. M. Fulrath, "Effect of spherical pores on the strength of a polycrystalline ceramic," *International Journal of Fracture,* vol. 13, no. 2, pp. 215-223, 1977.

[72] J. N. Goodier, "Concentration of stress around spherical and cylindrical inclusions and flaws," *Transactions of the American Society of Mechanical Engineers,* vol. 55, no. 7, pp. 39-44, 1933.

[73] J. Bruns, A. Zearley, T. George, O. Scott-Emuakpor and C. Holycross, "Vibration-Based Bending Fatigue of a Hybrid Insert-Plate System," *Experimental Mechanics,* vol. 55, pp. 1067-1080, 2015.

[74] O. Scott-Emuakpor, T. George, C. Holycross and C. Cross, "Improved Hybrid Specimen for Vibration Bending Fatigue," in *The Society for Experimental Mechanics*, Indianapolis, IN, 2017.

[75] T. A. Speddint and Z. Q. Wang, "Study on modeling of wire EDM process," *Journal of Materials Processing Technology,* vol. 69, no. 1-3, pp. 18-28, 1997.

[76] J. P. Kruth and P. Bleys, "Measuring residual stress caused by Wire EDM of tool steel," *International Journal of Electrical Machining,* vol. 5, pp. 23-28, 2000.

[77] O. Scott-Emuakpor, J. Schwartz, T. George, C. Holycross, C. Cross and J. Slater, "Bending fatigue life characterisation of direct metal laser sintering nickel alloy 718," *Fatigue and Fracture of Engineering Materials and Structures,* vol. 38, no. 9, pp. 1105-1117, 2015.